

MICELLE AND SOFT-PARTICLE DYNAMICS

A Dissertation

Presented to the Faculty of the Graduate School

of Cornell University

In Partial Fulfillment of the Requirements for the Degree of

Doctor of Philosophy

by

Bryan Andrew Rolfe

February 2016

© 2016 Bryan Andrew Rolfe

MICELLE AND SOFT-PARTICLE DYNAMICS

Bryan Andrew Rolfe, Ph. D.

Cornell University 2016

Soft matter systems deal with particles or collections of particles that respond to applied forces with a non-linear response. Examples include polymers, colloids, vesicles, gels, emulsions, micelles and capsules. It is therefore unsurprising that these soft particles are ubiquitous: present in our everyday life, biologically important, and found in many industrial processes. To these systems, flow plays an essential role technologically (e.g. electrospinning, microfluidics, and directed self-assembly), biologically (e.g., blood flow), and industrially (e.g. polymer extruders and pumping of nuclear waste).

Utilizing non-equilibrium coarse-grained molecular dynamics (CGMD), we have explored time and length scales of self-assembled polymeric micelles and polymer grafted nanoparticles (PGNs) beyond the computational realm of atomistic MD. We first showed that concentrated polymeric micelle suspensions strongly organize into 2D patterns normal to the flow direction. The precise lattice formed was found to be dependent upon micelle concentration and the rate of the applied shear, in agreement with literature in the high shear regime. It was also shown, for the first time, that individual micelles exhibit rich dynamical behavior under flow, including tank-treading, trembling, tumbling, stretching and contraction, and rotation.

Current work has addressed the latter, the dynamical behavior in the dilute regime of polymeric micelles and PGNs – that is, individual soft particles subjected to shear flow. Understanding these dynamics is interesting fundamentally, but also in the aforementioned applications where soft particles are closely packed. This work has shown that the presence of these soft particles induces a strong disturbance to the otherwise linear shear field, and the shape and extent of this disturbance is a function of a characteristic relaxation time (corona length) and rate of applied shear. Finally, the shape fluctuations, flow-alignment, rotation, and tank-treading of these particles have also been characterized in detail and are compared to the more well-understood dynamics of vesicles and star polymers.

BIOGRAPHICAL SKETCH

Bryan Rolfe pursued his Bachelor of Science in Chemical Engineering at Arizona State University. During that time he worked in the Earth and Space Sciences department researching heavy metal isotope geochemistry as a paleoredox proxy as well as for a tool to track hazardous waste contamination in groundwater. Through this work he earned an opportunity to conduct research in Dortmund, Germany, where he investigated ionic-liquids as liquid-liquid extraction media. He was also awarded the prestigious Congressional Goldwater Scholarship, in part because of his undergraduate research. Upon completion of his B.S., Bryan moved to Ithaca, NY in preparation for his graduate work at Cornell University. In his first months there, he briefly worked in in Susan Daniel's lab studying hydrophobic surfaces as a tool for droplet manipulation. Eventually, Bryan settled into Yong Joo's group to study complex fluids from a computational standpoint. Along the way he earned a second trip to Germany – this time a collaboration with the chemical company BASF – as well as funding through the National Science Foundation Graduate Research Fellowship. Bryan has also made it a point to bring science to the masses through his outreach initiatives while at Cornell, and strongly believes that this desire will be a driving force throughout his career.

To my mom, dad, teachers, professors, and mentors that have supported and encouraged me throughout my academic career.

ACKNOWLEDGMENTS

I would like to thank my advisor, Yong Joo, for the inspiration behind this project, as well as for always finding new ways in which our research together could elucidate problems in the field of complex fluids. I would also like to thank him for his support and understanding of my sometimes-eccentric career ambitions. I also owe a great deal to my special committee, Roseanna Zia and Brian Kirby for their advisement and wealth of knowledge, whether through conversation or lecture. Finally, I'd like to thank Olivier Desjardins for stepping in as an impromptu committee member during my defense.

I would not have been successful in my endeavors if it were not for the help, discussions, and collaborations of my classmates. In particular, I'd like to acknowledge Sushmit Goyal, Sai Pooja Mahajan, and Jonathan Saathoff for their expertise and Mark Richards, Anthony Altieri, and Joe Mattson for their unique perspectives on often complex problems.

Perhaps most significantly, I'd like to thank Laura Wasylenki; without her mentorship during my undergraduate career, I would not have been as fortunate to study at an institution like Cornell University, nor would have I been as successful in securing funding along the way.

My project would not have been possible without funding through the NSF-IGERT fellowship program, the NSF Graduate Research Fellowship Program (Grant No. DGE-1144153), and the Applied Mathematics Program within the Department of Energy Office of Advanced Scientific Computing.

TABLE OF CONTENTS

| | |
|--|-----------|
| BIOGRAPHICAL SKETCH | v |
| DEDICATION | vi |
| ACKNOWLEDGMENTS..... | vii |
| LIST OF FIGURES..... | x |
| LIST OF TABLES | xiv |
| LIST OF ABBREVIATIONS | xv |
| LIST OF SYMBOLS..... | xvi |
| CHAPTER 1..... | 17 |
| 1 INTRODUCTION | 17 |
| 1.1 Introduction | 17 |
| 1.2 Shear-ordering of block copolymer nanocomposites..... | 17 |
| 1.3 Flow induced disturbances of soft particles in simple shear fields..... | 23 |
| 1.4 Dynamics of soft particles in shear flow | 28 |
| REFERENCES..... | 35 |
| CHAPTER 2..... | 38 |
| 2 SHEAR ORDERING OF MICELLE-NANOPARTICLE SYSTEMS UNDERGOING SHEAR..... | 38 |
| 2.1 Introduction | 38 |
| 2.2 Model Details | 40 |
| 2.2.1 Interaction Potentials..... | 40 |
| 2.2.2 Dissipative particle dynamics..... | 45 |
| 2.3 Simulation Details | 46 |
| 2.3.1 Method and validation..... | 46 |
| 2.3.2 Structural analysis..... | 48 |
| 2.4 Results and Discussion | 50 |
| 2.4.1 Micelle formation in neat polymer solutions..... | 50 |
| 2.4.2 Dynamics of Micelle/Nanoparticle Systems..... | 62 |
| 2.5 Conclusions..... | 69 |
| REFERENCES..... | 71 |
| CHAPTER 3..... | 75 |
| 3 . FLOW DISUTRBANCES AROUND SOFT PARTICLES | 75 |
| 3.1 Introduction | 75 |
| 3.2 Methods and Models..... | 77 |
| 3.2.1 Coarse Grained Model..... | 77 |
| 3.2.2 Simulation details | 78 |
| 3.3 Results and Discussion | 83 |
| 3.3.1 Colloid..... | 83 |
| 3.3.2 Polymer-grafted Nanoparticles | 86 |
| 3.3.3 Polymeric Micelles..... | 91 |

| | |
|---|------------|
| 3.4 Conclusions | 99 |
| REFERENCES | 100 |
| CHAPTER 4 | 103 |
| 4 . DYNAMICS OF SOFT PARTICLES IN SHEAR FLOW | 103 |
| 4.1 Introduction | 103 |
| 4.2 Methods and Models | 105 |
| 4.2.1 Coarse Grained Model..... | 105 |
| 4.2.2 Simulation details | 108 |
| 4.2.3 Methods of analysis..... | 110 |
| 4.3 Results and Discussion | 113 |
| 4.3.1 Relaxation Phenomena..... | 114 |
| 4.3.2 Shape Deformations | 119 |
| 4.3.3 Rotational Motion | 126 |
| 4.4 Conclusions | 129 |
| REFERENCES | 131 |

LIST OF FIGURES

| | |
|--|----|
| Figure 1-1 – Phase diagram for P104 in solution determined from static light scattering, small-angle neutron scattering (SANS), and H-NMR experiments [3]. | 19 |
| Figure 1-2 – The effect of nanoparticle load in ordered micelle solutions [10]. | 20 |
| Figure 1-3 – Cartoon of a face-centered cubic (FCC) binary crystal. For the micelle/nanoparticle shear-ordering systems, the smaller particles represent nanoparticles (~7nm) and the larger particles represent micelles (~25nm). | 21 |
| Figure 1-4 – Small-angle neutron scattering results for silica nanoparticles (left) and for the surrounding micelle matrix (right) at two different shear rates [13]. | 22 |
| Figure 1-5 – Stokes flow solutions for spheres and cylinders taken from [17]. From left to right: streamlines for the fixed-object (no rotation), the freely-rotating (torque-free) object, and finally for potential flow. | 24 |
| Figure 1-6 – Flow field surrounding elliptical cylinders held at fixed inclination angles [17]. | 25 |
| Figure 1-7 – Flow field induced by two star polymers of different functionality from multi-particle collision dynamics simulations [26] | 27 |
| Figure 1-8 – DNA in shear flow, taken from [30]. Left shows a cartoon of several different behaviors the polymer participates in depending on the Weissenberg number. The right figure shows snapshots at different times of the polymer a $Wi = 19$. Each column shows a different transitory behavior; from left to right: tumbling, mass propagation, and stretching/collapsing (trembling). | 29 |
| Figure 1-9 – (Left) Snapshots of a fluid vesicle in three different dynamic regimes. (Right) Inclination angle (top) and an asphericity parameter (bottom) for the three different regimes. The three regimes are, from top-to-bottom (left) and left to right (right): steady tank-treading, tumbling, and trembling [24]. | 30 |
| Figure 1-10 – Contour plot of energy dissipation surrounding a vesicle modeled using the advected-field (AF) method at four different viscosity ratios, $r = 2, 4, 6$ and 7.8 . Lighter colors indicate greater dissipation. Taken from [33]. | 32 |
| Figure 1-11 – Normalized rotational frequency about the vorticity axis for simulated star polymers as a function of functionality-corrected Weissenberg number. The data collapse onto one master curve. Taken from [25]. | 33 |
| Figure 2-1 – Example of a 2D density projection calculated by projecting the 3D micelle-core density into two dimensions. Notice that brighter colors indicate greater density in the flow direction – information which is not available in the core-only projection. | 49 |
| Figure 2-2 – Snapshots for a 30% neat polymer solution at three stages of micelle formation (solvent omitted for clarity). First is the random starting configuration. Second is the non-sheared ‘equilibrated’ morphology. Third is the shear-induced morphology at $\gamma = 0.002\tau^{-1}$. In each case, the snapshots were chosen after the system reached its stable state where the micelles were no longer changing in the duration of the simulations. | 51 |

Figure 2-3 – Sheared ($\gamma = 0.002 \tau^{-1}$) structures of BCP solutions formed as a function of concentration. 10% (a) and 20% (b) states show no discernible lattice configuration. (c) 30% shows an unstable oblique lattice while the 40% solution (d) shows a stable oblique lattice. 50% (e) and 60% (f) solutions show a stable truncated square tiling with cylindrical micelles at the tile centers. (g) 80% shows a stable square lattice and (h) 100% shows a stable hexagonal lattice.....53

Figure 2-4 – (Left) Gradient-vorticity plane structures of BCP solutions formed at lower shear rates (a) $0.001\tau^{-1}$, (b) $0.002\tau^{-1}$, and (c) $0.004\tau^{-1}$. The insets show time-averaged structure factors in the same plane as the density projections. (Right) Gradient-shear snapshots (with 3x3 duplicates for clarity) showing mostly spherical or slightly elliptical micelle morphologies.....55

Figure 2-5 – (Left) Gradient-vorticity plane structures of BCP solutions formed at higher shear rates (a) $0.006\tau^{-1}$, (b) $0.008\tau^{-1}$, and (c) $0.01\tau^{-1}$. (Right) Gradient-shear snapshots (with 3x3 duplicates for clarity) showing the sphere to elongated morphology transition that occurs at higher shear rates56

Figure 2-6 – Schematic of different hydrophilic block lengths used in the corona length study.57

Figure 2-7 – Sheared ($\gamma = 0.002 \tau^{-1}$) structures of BCP solutions formed as a function of hydrophilic-block length. (a) A6B3 – Unstable oblique lattice; snapshot here showing two-fold order. (b) A6B6 – Metastable square lattice, snapshot chosen to show square lattice, but other snapshots show a less or more ordered state. (c) A6B9 – Stable truncated square tiling with cylindrical micelle at the tile center. (d) A6B12 – Stable oblique lattice, indicated by the strong peaks in the time-averaged structure factors.58

Figure 2-8 – Selected streamlines for a sheared ($\gamma = 0.002 \tau^{-1}$) A6B12 micelle containing 1764 polymer particles. The streamlines show the rotational behaviour of the fluid surrounding the micelle. The inset figure demonstrates the tank-treading behaviour by tracking two micelle polymers in time.60

Figure 2-9 – Disturbance to a linear shear flow profile as a function of corona length for selected micelles. The micelle sizes from left to right are: 1548, 1968, 1980 and 1764 particles. Note that identical micelle sizes were not available across all four systems. Top row shows the flow streamlines superimposed over a contour plot of the magnitude of the deviation (for reference, the wall velocity would be $0.0287 \sigma/\tau$). Bottom row shows the disturbance vector field superimposed over the angular velocity.61

Figure 2-10 – Examples of nanoparticle stability relative to several different A6B3-type micelles. The light-to-dark paths indicate the position of the nanoparticle at various times. (Left) A stable nanoparticle within the sample timeframe near the stagnation point of a 1143 particle micelle. (Middle) A nanoparticle perturbed from an initially metastable stagnation/vortex region surrounding a 1737 particle micelle. (Right) An unstable nanoparticle moving between two micelle lanes. ...64

Figure 2-11 – The effect of nanoparticles on the structural organization of the A6B3 micelles. The nanoparticle-free system is included for reference. Note that 1.5

| | |
|--|----|
| vol% corresponds to five particles with diameters of 6.0σ , where as 3.6 vol% corresponds to the same number of particles but with diameters of 8.0σ | 66 |
| Figure 2-12 – Comparison of shear and post-shear structure in a neat A6B12 solution (left) and a A6B12 system with 5 (1.5%vol) diameter 6σ nanoparticles (right). Below are plotted bond-order parameters (Ψ) calculated from micelle centers of mass as a function of timestep. Under shear, the bond-order parameters are constant and equal. Following shear, there is sharp separation of the different Ψ 's, indicative of 3-D organization. y-axis scales are the same; x-axis scales are different by a factor of two. Notice the square lattice formed with the nanoparticles included instead of a rhombic lattice of the neat solution. Averaged bond-order parameters (Ψ) calculated from micelle centers of mass as a function of timestep. | 68 |
| Figure 3-1– Examples of the three different types of objects studied in this paper. | 81 |
| Figure 3-2 - Streamlines for velocity field and contour plots for velocity disturbance magnitude are shown for fixed and free colloids. The left pane shows the stokes solutions for a sphere under these conditions, and the right pane shows the CGMD results obtained. | 85 |
| Figure 3-3 – Time-averaged polymer probability density plots (top) and time-averaged velocity disturbance fields (bottom) for the two shear extremes for B7 PGNs. Note that the density data are calculated the entire omitted vorticity axis whereas velocity field data are calculated within a vorticity-direction slice $\sim 6\sigma$ wide, centered at the center of mass. Snapshots of the PGNs are shown overlaid the disturbance fields. | 87 |
| Figure 3-4 - Matrix showing the magnitude of the flow deviation as a function of both corona length and shear rate for the PGN. Contour plots represent the magnitude of the deviation from a linear field of the shear rate applied to the cell. Vector fields show the directionality of the deviation in the 2D cross-section. | 89 |
| Figure 3-5 - Intensity data from flow disturbance magnitudes for PGNs (left) and polymeric micelles (right) as a function of angle from the flow. Here, an angle of 0 corresponds to the direction of the flow, and an angle of +/- 180 degrees corresponds to the direction away from the flow. | 91 |
| Figure 3-6 – Time-averaged polymer probability density plots (top) and time-averaged velocity disturbance fields (bottom) for the two shear extremes for A6B7 micelles. Note that the density data are calculated the entire omitted vorticity axis whereas velocity field data are calculated within a vorticity-direction slice $\sim 6\sigma$ wide, centered at the center of mass. Snapshots of the micelles are shown overlaid the disturbance fields. | 92 |
| Figure 3-7 - Matrix showing the magnitude of the flow deviation as a function of both corona length and shear rate for a micelle. Contour plots represent the magnitude of the deviation from a linear field of the shear rate applied to the cell. Vector fields show the directionality of the deviation in the 2D cross-section. Overlaid numeric values correspond to the Wi number. | 94 |
| Figure 3-8 – Intensity data from flow disturbance magnitudes for PGNs (left) and polymeric micelles (right) as a function of angle from the flow. Here, an angle of | |

| | |
|---|-----|
| 0 corresponds to the direction of the flow, and an angle of +/- 180 degrees corresponds to the direction away from the flow. | 95 |
| Figure 3-9 - A comparison of the flow characteristics of a free colloid, a PGN (CB9) and a micelle (A6B9), left to right, subjected to simple shear ($\gamma = 0.008\tau-1$). The top row shows the streamlines of the flow, with flow disturbance magnitudes as the contour background. The bottom row shows the deviation velocity field with the background contour field representing the relative magnitudes of the vorticity..... | 97 |
| Figure 4-1– Examples of the three different types of objects studied in this paper. .. | 110 |
| Figure 4-2 – Time autocorrelation functions for the end-to-end (left) and end-to-center (right) vectors of the constituent polymers in the micelles. Shown are A6B1 (blue), A6B3 (black), A6B5 (red), A6B7 (magenta), and A6B9 (black, dashed). All results are taken from the zero-shear state. Inset shows the relaxation times extracted from the correlation functions with a power law fit as a function of total polymer length..... | 115 |
| Figure 4-3 – (Top) Snapshots for the two model systems, isolating grafted polymer relaxation behavior. (Bottom) Relaxation times τ_R for polymer grafted walls (PGWs) (left) at matched grafting density to polymer grafted nanoparticles (right) plotted against grafted polymer length. The relaxations for the PGNs are for the case in which translation and rotational motions on the rigid core are removed from the simulations. | 117 |
| Figure 4-4 – (Left) Mean-squared angular displacement for different tethered polymer lengths. (Right) Dimensionless rotational diffusion coefficients plotted against tethered polymer length, $DR, ideal = 2.65 \times 10^{-5}\tau-1$ | 119 |
| Figure 4-5 – Snapshots of A6B7 micelles demonstrating different dynamic regimes occurring at low and high shear rates. In both cases, the micelles are tank-treading. | 120 |
| Figure 4-6 – Normalized diagonal components of the gyration tensor for the shortest and longest tethered length for PGNs (left) and micelles (right) plotted against applied shear. All quantities are time-averaged and measured in the steady-state. | 121 |
| Figure 4-7 – Asphericity parameters for micelles (top) and PGNs (bottom) plotted against shear rate (left) and Wi (right). Wi values are computed by relaxation times characteristic to each particle: a relaxation of the polymer end-to-end vector for the micelles, and the isolated relaxation of the grafted polymers for the nanoparticles..... | 124 |
| Figure 4-8 – Flow alignment, or orientational resistance, for PGNs (top) and micelles (bottom). Note that the nature of this calculation is not well-suited for nearly-spherical particles, and statistically noisy data have been excluded. | 126 |
| Figure 4-9 – Normalized rotational frequencies for PGNs (top) and micelles (bottom) plotted against shear rate (left) and collapsed into master curves against Wi (right)..... | 128 |

LIST OF TABLES

| | |
|--|-----|
| Table 2-1 MD Reduced Units..... | 41 |
| Table 2-2 - Details of interaction parameters used in this paper..... | 43 |
| Table 2-3 – Interaction matrix; W = Water/Solvent, A = A-type copolymer, B = B-type copolymer, and C = colloid. | 44 |
| Table 2-4 – Simulation Parameters | 47 |
| Table 3-1 – MD Units..... | 77 |
| Table 3-2 – Details of interaction parameters used in this paper. | 78 |
| Table 3-3 – Interaction matrix; W = Water/Solvent, A = A-type copolymer, B = B-type copolymer, and C = colloid. | 78 |
| Table 3-4 – Simulation Parameters | 79 |
| Table 3-5 – Summary of important results..... | 96 |
| Table 4-1 – MD Unit definitions | 106 |
| Table 4-2 – Interaction parameters used in these simulations..... | 106 |
| Table 4-3 – Interaction matrix; W = Water/Solvent, A = A-type copolymer, B = B-type copolymer, and C = colloid. | 106 |
| Table 4-4 – Summary of simulation parameters | 108 |

LIST OF ABBREVIATIONS

| | |
|-------------|---------------------------------------|
| AF | Advected Field (methods) |
| BCC | Body-Centered Cubic |
| BCP | Block Copolymer |
| CGMD..... | Coarse-Grained Molecular Dynamics |
| COM/CM..... | Center of Mass |
| DPD | Dissipative Particle Dynamics |
| FCC | Face Centered Cubic |
| HCP | Hexagon Close Packing/Packed |
| LAOS | Large-Amplitude Oscillatory Shear |
| LJ | Finitely-Extensible Nonlinear Elastic |
| MD | Molecular Dynamics |
| NP | Nanoparticles |
| PB | Periodic Boundaries |
| PEO..... | Polyethylene Oxide |
| PGN | Polymer Grafted Nanoparticles |
| PGW | Polymer Grafted Wall |
| PPO..... | Polypropylene Oxide |
| SANS | Small-Angle Neutron Scattering |
| WCA | Weeks-Chandler-Anderson |

LIST OF SYMBOLS

| | |
|-----------------------------------|---------------------------------------|
| $\dot{\gamma}$ | Shear rate |
| σ | LJ diameter |
| ϵ | LJ interaction energy |
| m | LJ mass |
| τ | MD time |
| τ_R | Relaxation time |
| τ_{RR} | Rotational relaxation time |
| P^* | MD pressure |
| T^* | MD Temperature |
| k_B | Boltzmann Constant |
| ρ | Number density |
| $k_B T$ or kT | Unit of energy |
| ζ | DPD friction parameter |
| ξ_{ij} | DPD Gaussian random number |
| D^* | MD Diffusivity Coefficient |
| D_R | MD Rotational Diffusivity Coefficient |
| η^* | MD shear viscosity |
| η_0^* | MD zero-shear viscosity |
| k | Wave vector |
| ψ_l | Steinhardt bond-order parameter |
| η^* | MD shear viscosity |
| Pe | Peclet number |
| Wi | Weissenberg number |
| Re | Reynolds number |
| \vec{v} | Vorticity direction |
| a | Hard colloid diameter |
| R_{ee} | End-to-end vector |
| R_g | Radius of gyration |
| L | Contour length or box length |
| G | Gyration tensor |
| G_1, G_2, G_3 | Eigen values of the gyration tensor |
| m_g | Orientalional resistance parameter |
| χ | Inclination angle |
| ω_α or Ω | Rotational frequency about α |

CHAPTER 1

1 INTRODUCTION

1.1 Introduction

This introduction gives a brief overview of the topics investigated in the chapters that will follow. We include here important results from published literature, as well some of the shortcomings or gaps in these studies that we will address later. The overall organization of this chapter follows the organization of the main results chapters: shear-ordering of colloidal systems, flow disturbances around soft particles, and concluding with dynamics of these soft particles.

With few exceptions, all work presented here deals with flows that fall into the realm of simple shear. In other words: any flow where the unperturbed fluid has a velocity in a single direction and whose magnitude varies linearly in the perpendicular direction. Though this restriction may seem of little practical interest, its importance becomes clear when one considers that simple shear exists nearly always near interfaces in a general flow. Flow through blood vessels and the channels of microfluidic devices are a few ubiquitous examples. Another example that our group is particularly interested in is electrospinning, where shear flow is present at the fluid/air interface of the viscoelastic jet.

1.2 Shear-ordering of block copolymer nanocomposites

As the backbone of this work, block copolymers (BCPs) deserve special attention. BCPs are single-chained molecules that consist of two or more distinct

polymer groups. A diblock copolymer, for example, would consist of the union of an A and B-type homopolymer, sometimes requiring a non-repeating junction block. Similarly, a triblock copolymer could consist of a union of A, B, and A-type blocks, in that order, or A, B, and C-type blocks. The number-prefix is not derived from the number of block types, but rather the number of distinct block regions. In other words, both an A-B-C and A-B-A molecule would be considered triblock copolymers.

The utility of block copolymers arises from their ability to self-organize either in polymer melts, or in selective solvents. Many of the mass-produced block copolymers are derived from ethylene oxide (EO) and propylene oxide (PO) groups, the latter being less soluble in water. The difference in the solubility is a desirable property as it is the driving force for self-organization in equilibrium. The exact morphology formed during self-organization, or self-assembly, is a strong function of solvent, temperature, polymer chemistry, and concentration of the polymer in solution [1], [2]. A phase diagram for P104 ($\text{EO}_{18}\text{PO}_{58}\text{EO}_{18}$) in solution is shown in Figure 1-1 for illustration. For this BAB-type triblock copolymer, the A-type polymer minimizes its contact with the solvent, forming the core of, for instance, a spherical micelle. Interestingly, self-assembly is only observed below a certain temperature (about 80C for P104). Above this temperature, entropic effects dominate, and polymers do not self-assemble. Another important feature is that the morphology depends primarily on concentration. As one increases the concentration, the P104 polymers transition into worm-like micelles (with a hexagonal packing), and at high concentrations, into lamella (layers with 1-dimensional order). Some regions contain two phases, and are labeled as such (2Φ).

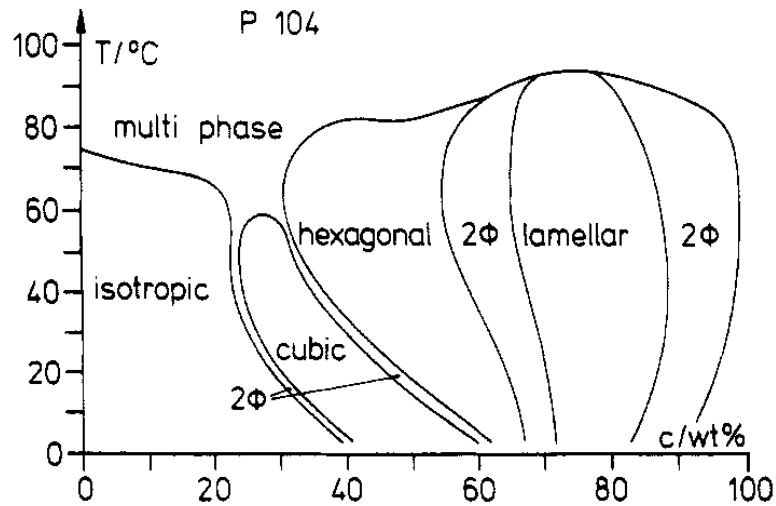


Figure 1-1 – Phase diagram for P104 in solution determined from static light scattering, small-angle neutron scattering (SANS), and H-NMR experiments [3].

The cubic phase seen in Figure 1-1 for spherical micelles is not unlike that of concentrated hard-sphere solution. At this level of coarseness, both systems minimize their free-energy by organizing into close-packed configurations. Typically though, these systems quickly become diffusion limited, and only ever attain local order. In other words, a scattering experiment – SANS was used to generate the phase diagram in Figure 1-1 – will show only radial order, with scattering intensities being independent of scattering angle. It was later discovered that under applied shear, colloidal systems sometimes exhibit long-range order with close packed planes of a crystal lattice aligned parallel to the flow [4]. Scattering experiments of the resulting morphology reveal six-fold directional order (such as an HCP lattice) as shown in Figure 1-4, in contrast the pure-radial symmetry seen prior. The alignment and sliding of these lattice layers corresponds, in a rheological sense, to a shear-thinning regime. Possible formulations for sliding mechanisms have been proposed by Loose and

Ackerson [5]. Morphologically and at low concentrations, spherical micelles behave in much the same way as hard spheres, exhibiting long-range order under the right shear conditions [6]–[9]. It was later found that these well-ordered micelle systems could also be used to template nanoparticles [10]–[12]. Nanoparticles may be templated by either including them within the hydrophobic region of the micelles (i.e. making the nanoparticles hydrophobic), or by simply placing them into the external matrix. In the latter approach, the result is a binary crystal, much like the one illustrated in Figure 1-3. An accurate way to determine the microstructure is through in-situ small-angle neutron scattering experiments with a specially designed couette cell [13] – a resulting scattering pattern is shown in Figure 1-4. The scattering patterns are consistent with HCP alignment with the flow direction, as proposed by Loose and Ackerson, but cannot reveal *how* the layers slip by one another.

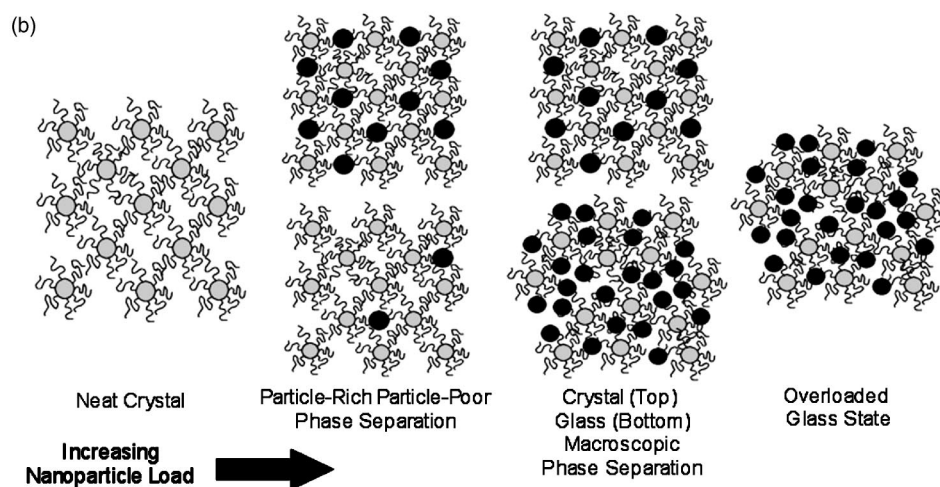


Figure 1-2 – The effect of nanoparticle load in ordered micelle solutions [10].

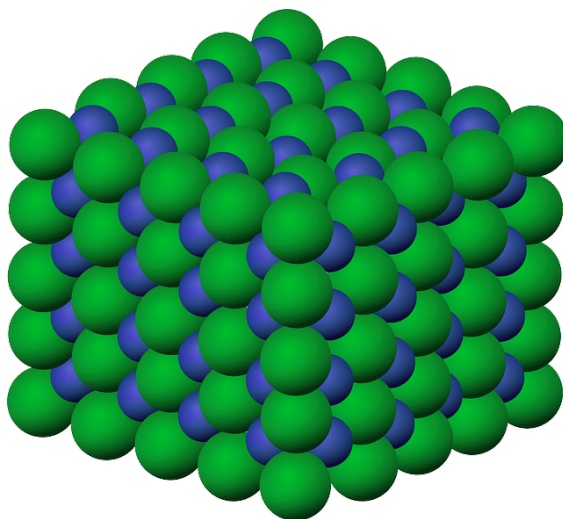


Figure 1-3 – Cartoon of a face-centered cubic (FCC) binary crystal. For the micelle/nanoparticle shear-ordering systems, the smaller particles represent nanoparticles (~7nm) and the larger particles represent micelles (~25nm).

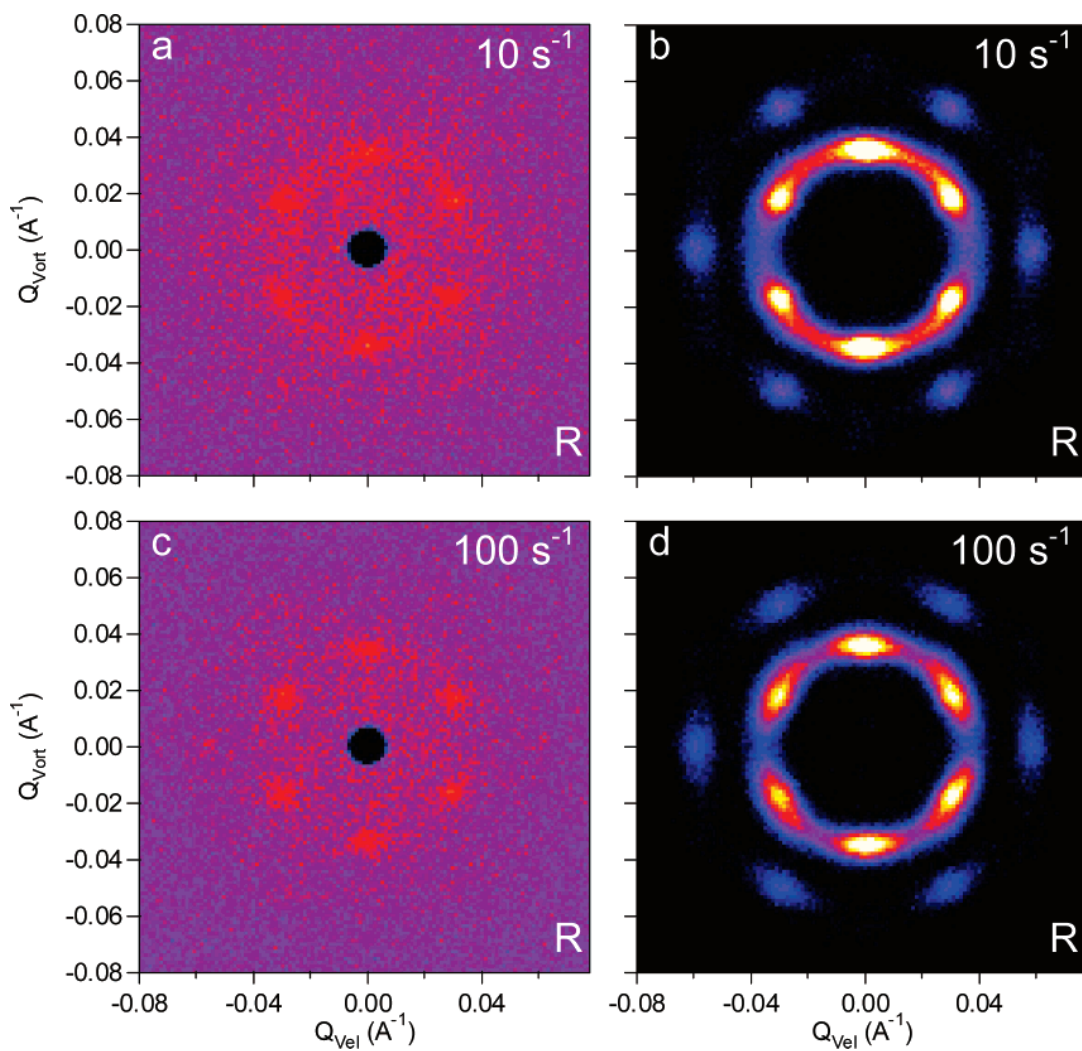


Figure 1-4 – Small-angle neutron scattering results for silica nanoparticles (left) and for the surrounding micelle matrix (right) at two different shear rates [13].

Though the experimental studies that have been performed have proved that type and strength of the shear field, as well as the size of the nanoparticles are important factors governing nanoparticle templating, they have difficulty elucidating the microscopic mechanisms controlling the degree of order. As a result, full controllability of these nanocomposites remains elusive. Computational methods, especially coarse-grained molecular dynamics, provide a means to explore these

otherwise inaccessible time and length scales, given that the methods are first validated against experimental results.

Unique to the work that is presented here, is that we explore micelle ordering in the non-equilibrium regime. The number of publications covering equilibrium states of similar systems is far greater, and, in fact, there are no known publications prior to this work on the shear-ordering of micelle nanoparticle composite systems.

1.3 Flow induced disturbances of soft particles in simple shear fields

An object placed in a flow field will necessarily affect a change, or a disturbance, to the flow, which in turn may influence positioning and behavior of surrounding objects – in this case, micelles and nanoparticles. Under certain conditions, the resulting steady-state flow can be known analytically. Stokes flow around an ideal sphere is one of the simplest examples (Figure 1-5). In contrast, deformable and non-spherical objects present a considerable challenge. Axisymmetric ellipsoids have been extensively studied [14]–[16], with the seminal paper on the subject first published by Jeffery in 1922 [14]. His work demonstrated that ellipsoidal particles, at low shear rates, undergo periodic rotation and precession, forming closed paths (relative to the flow) that were later coined Jeffery orbits. Most importantly, the flow around isolated rigid ellipsoids is therefore time-transient, as the orientation of the ellipsoid is time-transient.

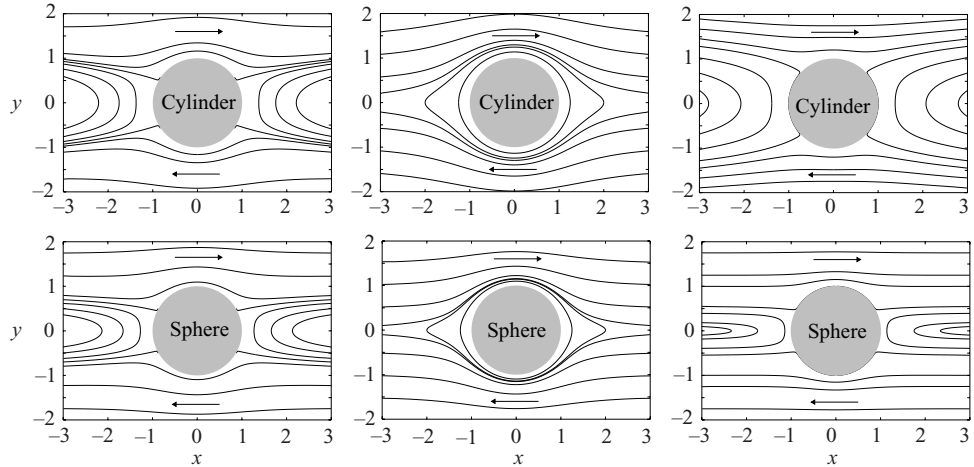


Figure 1-5 – Stokes flow solutions for spheres and cylinders taken from [17]. From left to right: streamlines for the fixed-object (no rotation), the freely-rotating (torque-free) object, and finally for potential flow.

Deformable ellipsoids can behave very differently from rigid ellipsoids. In certain shear regimes, deformable ellipsoids undergo tank-treading behavior, which is a direct result of their non-rigid nature [18]. This behavior can be described as the constituent components of the deformable object rotating about the center of mass, while the overall shape of the object may be stretched and inclined to the flow. As a result, there is a steady-state solution to the surrounding flow, though it may or may not be known analytically. Computing numerical solutions to the Stokes equations for ellipsoids held at a fixed inclination angles is the simplest way to approximate the flow for a tank-treading ellipsoid (Figure 1-6). On the theoretical front, Keller and Skalak were able to develop a model derived from equilibrium and energy considerations for ellipsoidal vesicles that captures the transition from steady-state to transitory behavior [19]. However, the complexities resulting from vesicle non-

ellipsoidal deformation has forced the most significant recent progress to be in numerical models, such as efforts by the Misbah group [20], [21]. Thus, it is unsurprising that the flow around other soft particles, including micelles, is even less understood.

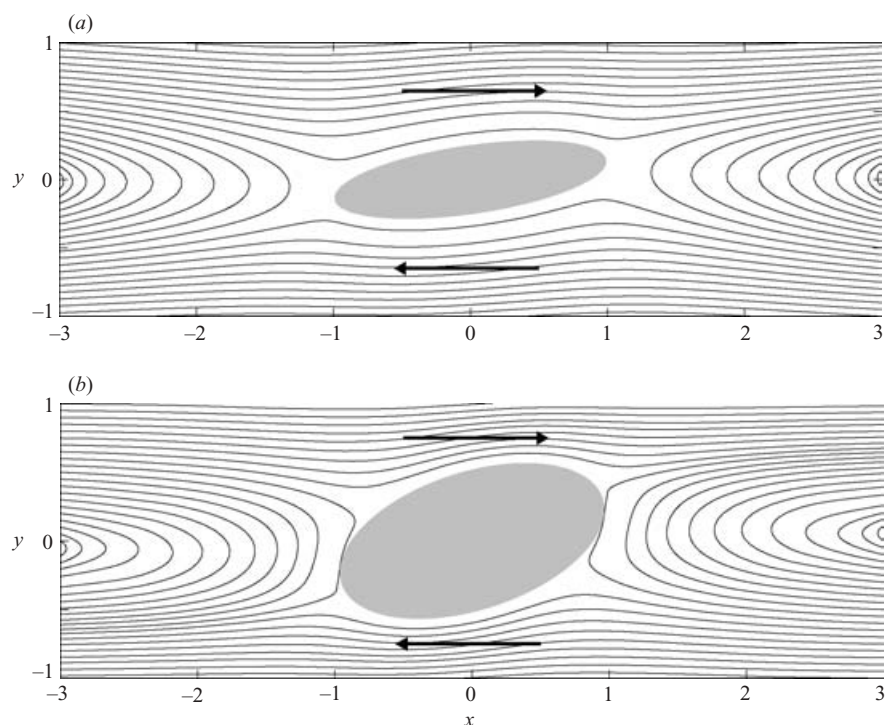


Figure 1-6 – Flow field surrounding elliptical cylinders held at fixed inclination angles [17].

Another hurdle in the path to understanding the flow effects of micelles in shear flow is their small size. Whereas vesicles have been extensively studied in part for their biological importance, they are also of such scale that they can be inspected visually and in situ with creative development of an experimental apparatus. There are many examples in the literature experimentally addressing flow and dynamics of

vesicles, and references [22]–[24] are a few good examples. In contrast, at the scale of polymeric micelles, there are only a handful of publications that have attempted to model or simulate flow effects or dynamics. The bulk of these studies have been aimed at star polymers.

Star polymers serve as good tools for comparison as they are similar to micelles in their size, deformability, and chemical composition. Most of the available knowledge of these systems has come from Gompper's group in Germany. Their simulations have suggested that star polymers in shear flows induce a rotational velocity disturbance and exhibit dynamics similar to other soft bodies in shear. These phenomena are further characterized by the grafting density, and to a lesser extent, the size, of the star polymers [25]–[28]. An example of the flow around two star polymers of different grafting densities is shown in Figure 1-7. Note the rotational flow around the stars, the straddling in-plane stagnation points and finally the corresponding counter-rotating vortices on either side. This flow is only qualitatively similar to the numerical solutions for ellipsoids held at fixed inclination angles. A similar method has been employed to study branched polymers, with the simplest branch polymer being a star polymer [29].

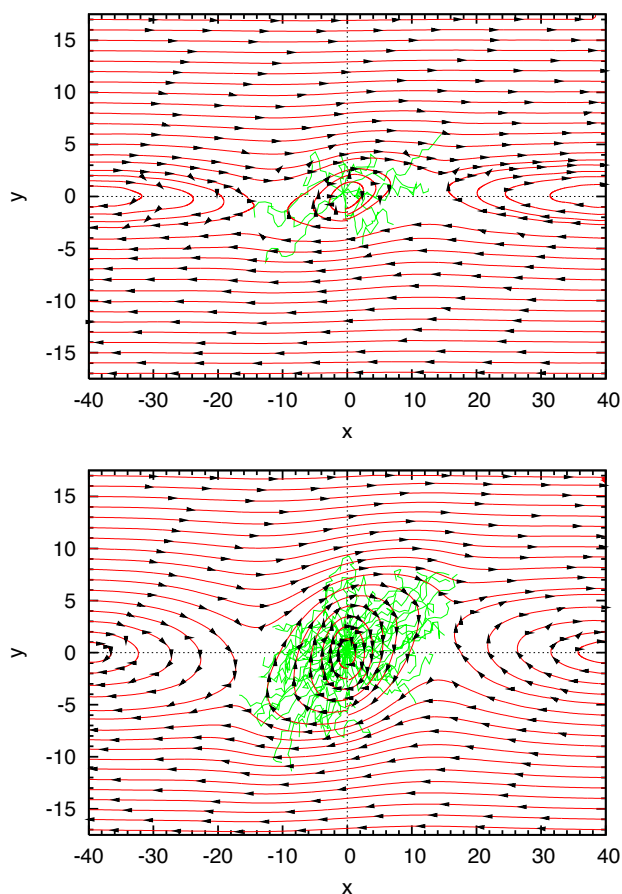


Figure 1-7 – Flow field induced by two star polymers of different functionality from multi-particle collision dynamics simulations [26]

The work on stars is promising, but may not translate directly to spherical micelles. One key difference between micelles and star polymers is that the polymeric arms of a star have a common chemical bonding point. Micelles on the other hand are held together by entropic and energetic forces – at a given temperature and concentration, it is most favorable for the system to organize into micelles. This difference should become important as the system is perturbed further away from equilibrium, such as at very high shear rates.

To our knowledge, there are no existing publications addressing flow disturbances arising from the presence of micelles. Furthermore, it is difficult to directly experimentally validate dynamic behavior at these exceedingly small length and time scales. For these reasons, the focus here is develop a qualitative understanding of these systems and draw comparisons to similar systems such as vesicles and star polymers. At a minimum, we hope that our work here will provide motive for further exploratory studies, and perhaps, one day, evaluation through novel experimental techniques.

1.4 Dynamics of soft particles in shear flow

As the previous section has clearly shown, soft bodies, whether vesicles or star polymers, induce measurable flow disturbances through both obstruction and dynamic motion. The latter, the dynamic aspects, encompass a broad spectrum of behaviors which may include tumbling, trembling, stretching and contraction, tank-treading, and sometimes fusion and fission.

DNA is a good example illustrating many of these behaviors. As with vesicles, DNA's biological importance and relatively large size has made it the subject of many experimental and theoretical investigations. In the quiescent state, DNA will adopt a conformation that greatly depends on temperature and solvent conditions. For example, lambda bacteriophage DNA in a sugar solution adopts an elliptical conformation with a hydrodynamic diameter of $\sim 2\text{nm}$ [30], [31]. Under shear, the DNA molecule may undergo a variety of behavior depending on the strength of the applied field. Stretching always occurs, with elongation in the direction of shear or along an axis slightly inclined. Contraction may follow, collapsing the DNA back into

its spherical conformation. Often this pattern of stretching and contraction is periodic in the steady state, which would then be termed a “trembling” behavior. The DNA molecule may also tumble in the flow, where the end-to-end length remains relatively constant, but the end-to-end vector rotates. Figure 1-8 gives an example of some of these behaviors for DNA in shear flow [30].

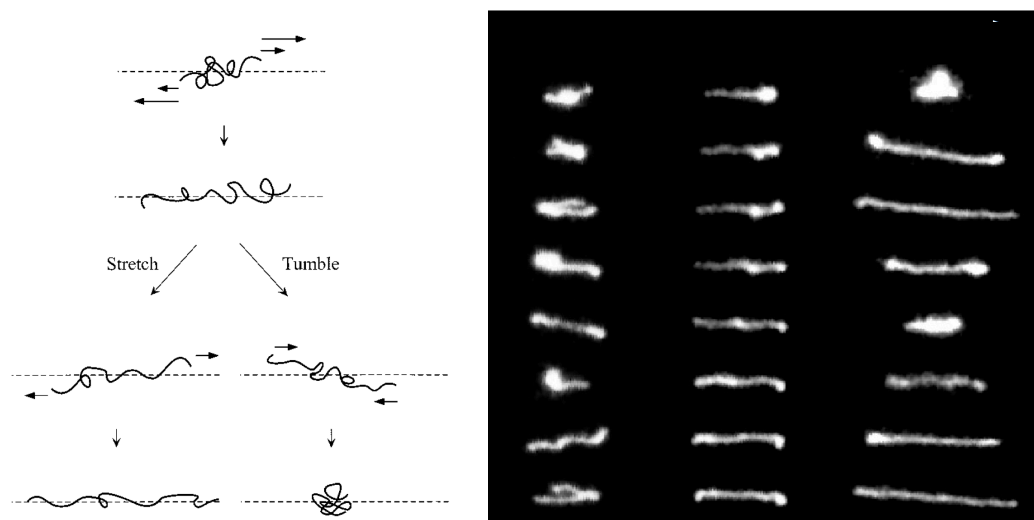


Figure 1-8 – DNA in shear flow, taken from [30]. Left shows a cartoon of several different behaviors the polymer participates in depending on the Weissenberg number. The right figure shows snapshots at different times of the polymer a $Wi = 19$. Each column shows a different transitory behavior; from left to right: tumbling, mass propagation, and stretching/collapsing (trembling).

Many of the behaviors seen in single polymer chains are also seen in fluid vesicles. Fluid vesicles lack the one dimensionality of polymer chains but retain the viscoelasticity as they are merely an encapsulation of a fluid by a flexible, elastic membrane. Like DNA, vesicles have also been studied extensively, in part, owing to their both their biological importance and larger size. However, it is important to note

that vesicles range in diameter from nanometers (liposomes) to hundreds of microns in (red blood cells). They also accommodate an additional behavior that would not be well defined in single-polymer dynamics: tank-treading. Figure 1-9 provides an illustration of the primary dynamic regimes seen for fluid vesicles.

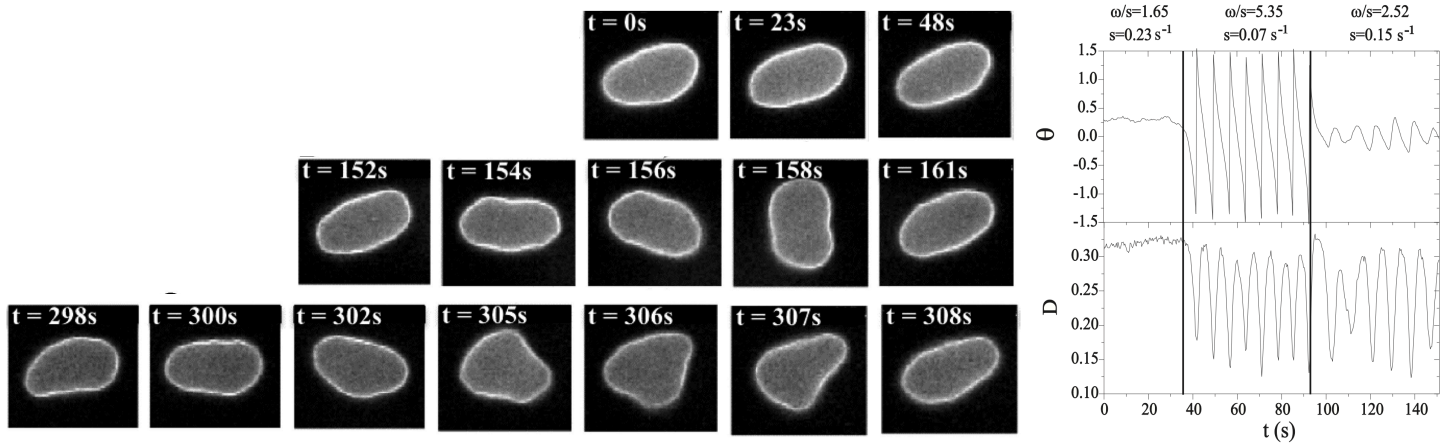


Figure 1-9 – (Left) Snapshots of a fluid vesicle in three different dynamic regimes. (Right) Incline angle (top) and an asphericity parameter (bottom) for the three different regimes. The three regimes are, from top-to-bottom (left) and left to right (right): steady tank-treading, tumbling, and trembling [24].

Understanding vesicle systems is important in, for example, blood rheology, where strong shear forces are present near the vessel walls. Models have been developed to attempt to capture qualitatively and quantitatively the characteristics of the dynamics, as well as the transitions as a function of key parameters. The dynamics of a vesicle are commonly- modeled by three parameters: the viscosity contrast (the ratio of the viscosities for the encapsulated fluid and surrounding fluid), the swelling parameter, and the shape relaxation time [32], [33]. The aforementioned Keller Skalak model [19], originally developed for tank-treading ellipsoids, qualitatively

captures the physics for vesicles in shear flow quite well, and quantitatively in two dimensions [33]. This is a surprising result, since shape deformations (beyond the idealized ellipsoidal vesicle) occur in realistic systems. Boundary integral and advected-field (AF) methods have also been somewhat successful at capturing and predicting the physics of deformable vesicles, using a minimal number of adjustable parameters. The energy dissipation in the surrounding fluid using the AF method is shown in Figure 1-10

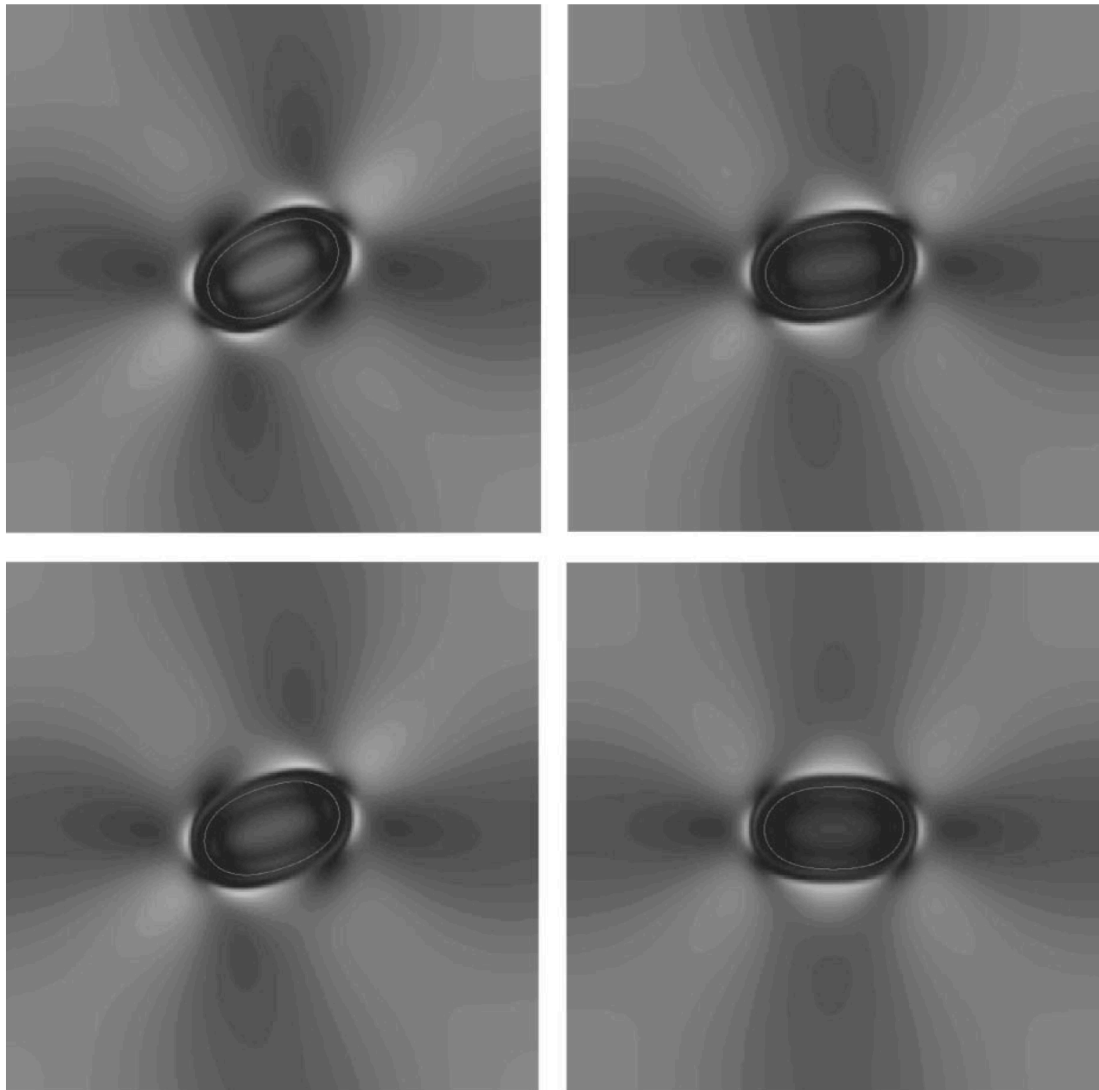


Figure 1-10 – Contour plot of energy dissipation surrounding a vesicle modeled using the advected-field (AF) method at four different viscosity ratios, $r = 2, 4, 6$ and 7.8 . Lighter colors indicate greater dissipation. Taken from [33].

Star polymer dynamics have also been investigated using multiparticle collision dynamics method mentioned previously [25], [26], [28]. Unlike vesicles, there is no corresponding ratio of viscosities to characterize the star polymer behavior. Nonetheless, these studies have shown that star polymers may exhibit many of same behaviors seen in fluid vesicles. Rather than a ratio of viscosities, an increased functionality (the number of polymer arms) results in a transition from polymer-like to capsule-like dynamics. Moreover, these studies have successfully collapsed the predominant behavior -- tank-treading at a constant inclination angle -- using a characteristic relaxation time, as shown in Figure 1-11. More interestingly, there are two distinct regions of rotation: one at low Wi , where the stars rotate proportionally to the applied shear, and one at high Wi , where the rotation rate becomes sub-linear. We will explore this phenomena and its importance in polymeric micelles in more detail in the final chapter of this work.

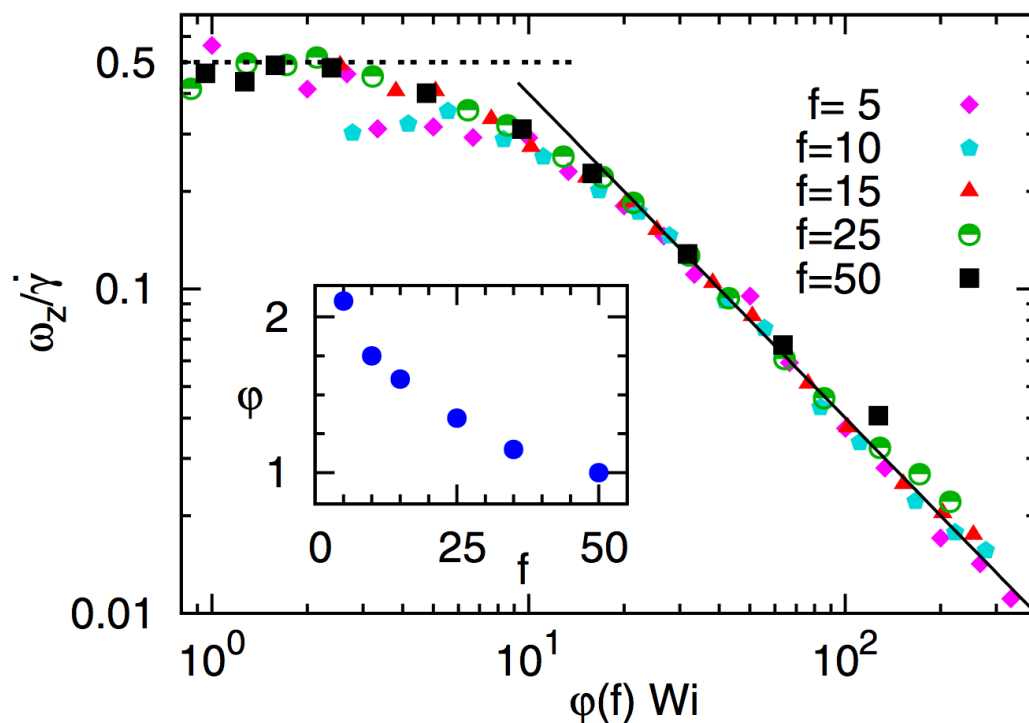


Figure 1-11 – Normalized rotational frequency about the vorticity axis for simulated star polymers as a function of functionality-corrected Weissenberg number. The data collapse onto one master curve. Taken from [25].

Inspired by the simulation work done with star and branched polymers, we apply the tools of analysis by those authors to dilute systems of polymeric micelles. The similarity between micelles and star polymers leads us to suspect that the dynamics we see should be similar at comparable Weissenberg values and that our data should also collapse under a suitable choice of a relaxation time. However, the differences that do exist, most notably the deformable core of the micelle, present new challenges that in this analysis that we will try to address. To this end, we also look at an intermediary: a colloid particle with polymers tethered to its surface. This type of particle has the tremendous advantage of tune-able “softness” through varying the

length of the tethered polymers. No literature exists, to our knowledge, addressing the dynamics of either tethered nanoparticles or micelles.

REFERENCES

- [1] F. S. Bates and G. H. Fredrickson, "Block copolymer thermodynamics: theory and experiment.," *Annu. Rev. Phys. Chem.*, vol. 41, pp. 525–557, 1990.
- [2] K. Almdal, K. a Koppi, F. S. Bates, and K. Mortensen, "Multiple ordered phases in a block copolymer melt," *Macromolecules*, vol. 25, pp. 1743–1751, 1992.
- [3] G. Wanka, H. Hoffmann, and W. Ulbricht, "Phase diagrams and aggregation behavior of poly (oxyethylene)-poly (oxypropylene)-poly (oxyethylene) triblock copolymers in aqueous solutions," *Macromolecules*, pp. 4145–4159, 1994.
- [4] B. J. Ackerson, "Shear induced order and shear processing of model hard sphere suspensions," *J. Rheol. (N. Y. N. Y.)*, vol. 34, no. 4, p. 553, May 1990.
- [5] W. Loose and B. J. Ackerson, "Model calculations for the analysis of scattering data from layered structures," *J. Chem. Phys.*, vol. 101, no. 9, p. 7211, 1994.
- [6] F. R. Molino, J.-F. Berret, G. Porte, O. Diat, and P. Lindner, "Identification of flow mechanisms for a soft crystal," *Eur. Phys. J. B*, vol. 3, pp. 59–72, 1998.
- [7] M. J. Park, J. Bang, T. Harada, K. Char, and T. P. Lodge, "Epitaxial transitions among FCC, HCP, BCC, and cylinder phases in a block copolymer solution," *Macromolecules*, vol. 37, pp. 9064–9075, 2004.
- [8] K. Mortensen, "Structural studies of aqueous solutions of PEO-PPO-PEO triblock copolymers, their micellar aggregates and mesophases; a small-angle neutron scattering study," *J. Phys. Condens. Matter*, vol. 103, no. 8, pp. A103–A124, 1996.
- [9] K. Mortensen and J. S. Pedersen, "Structural study on the micelle formation of poly(ethylene oxide)-poly(propylene oxide)-poly(ethylene oxide) triblock copolymer in aqueous solution," *Macromolecules*, vol. 26, no. 4, pp. 805–812, Jul. 1993.
- [10] D. C. Pozzo, K. R. Hollabaugh, and L. M. Walker, "Rheology and phase behavior of copolymer-templated nanocomposite materials," *J. Rheol. (N. Y. N. Y.)*, vol. 49, no. 3, p. 759, 2005.
- [11] D. C. Pozzo and L. M. Walker, "Small-angle neutron scattering of silica nanoparticles templated in PEO–PPO–PEO cubic crystals," *Colloids Surfaces A Physicochem. Eng. Asp.*, vol. 294, no. 1–3, pp. 117–129, Feb. 2007.

- [12] C. G. Goltner, S. Henke, M. C. Weissenberger, and M. Antonietti, “Mesoporous Silica from Lyotropic Liquid Crystal Polymer Templates,” *Angew. Chemie Int. Ed.*, vol. 37, pp. 613–616, 1998.
- [13] D. C. Pozzo and L. M. Walker, “Shear Orientation of Nanoparticle Arrays Templated in a Thermoreversible Block Copolymer Micellar Crystal,” *Macromolecules*, vol. 40, no. 16, pp. 5801–5811, Aug. 2007.
- [14] G. Jeffery, “The motion of ellipsoidal particles immersed in a viscous fluid,” *Proc. R. Soc. London. Ser. A, ...*, 1922.
- [15] E. Hinch and L. Leal, “Rotation of small non-axisymmetric particles in a simple shear flow,” *J. Fluid Mech.*, vol. 92, 1979.
- [16] F. P. Bretherton, “The motion of rigid particles in a shear flow at low Reynolds number,” *J. Fluid Mech.*, vol. 14, no. 1956, p. 284, 1962.
- [17] D. R. Mikulencak and J. F. Morris, “Stationary shear flow around fixed and free bodies at finite Reynolds number,” *J. Fluid Mech.*, vol. 520, pp. 215–242, Dec. 2004.
- [18] H. L. Goldsmith and J. Marlow, “Flow Behaviour of Erythrocytes. I. Rotation and Deformation in Dilute Suspensions,” *Proc. R. Soc. B Biol. Sci.*, vol. 182, no. 1068, pp. 351–384, Oct. 1972.
- [19] S. Keller and R. Skalak, “Motion of a tank-treading ellipsoidal particle in a shear flow,” *J. Fluid Mech.*, vol. 120, no. -1, p. 27, Apr. 1982.
- [20] F. Rioual, T. Biben, and C. Misbah, “Analytical analysis of a vesicle tumbling under a shear flow,” *Phys. Rev. E*, vol. 69, no. 6, p. 061914, Jun. 2004.
- [21] T. Biben, A. Farutin, and C. Misbah, “Three-dimensional vesicles under shear flow: Numerical study of dynamics and phase diagram,” *Phys. Rev. E*, vol. 83, no. 3, p. 031921, Mar. 2011.
- [22] H. L. Goldsmith, “The microrheology of red blood cell suspensions.,” *J. Gen. Physiol.*, vol. 52, no. 3, pp. 5–28, 1968.
- [23] M. Abkarian, M. Faivre, and A. Viallat, “Swinging of Red Blood Cells under Shear Flow,” *Phys. Rev. Lett.*, vol. 98, no. 18, p. 188302, Apr. 2007.
- [24] J. Deschamps, V. Kantsler, E. Segre, and V. Steinberg, “Dynamics of a vesicle in general flow.,” *Proc. Natl. Acad. Sci. U. S. A.*, vol. 106, no. 28, pp. 11444–7, Jul. 2009.

- [25] M. Ripoll, R. Winkler, and G. Gompper, “Star Polymers in Shear Flow,” *Phys. Rev. Lett.*, vol. 96, no. 18, p. 188302, May 2006.
- [26] M. Ripoll, R. Winkler, and G. Gompper, “Hydrodynamic screening of star polymers in shear flow,” *Eur. Phys. J. E*, vol. 23, no. 4, pp. 349–54, Aug. 2007.
- [27] S. P. Singh, D. a Fedosov, A. Chatterji, R. G. Winkler, and G. Gompper, “Conformational and dynamical properties of ultra-soft colloids in semi-dilute solutions under shear flow.,” *J. Phys. Condens. Matter*, vol. 24, no. 46, p. 464103, Nov. 2012.
- [28] S. P. Singh, A. Chatterji, G. Gompper, and R. G. Winkler, “Dynamical and Rheological Properties of Ultrasoft Colloids under Shear Flow,” *Macromolecules*, vol. 46, no. 19, pp. 8026–8036, Oct. 2013.
- [29] A. Nikoubashman and C. N. Likos, “Branched Polymers under Shear,” *Macromolecules*, vol. 43, no. 3, pp. 1610–1620, Feb. 2010.
- [30] D. E. Smith, “Single-Polymer Dynamics in Steady Shear Flow,” *Science (80-.)*, vol. 283, no. 5408, pp. 1724–1727, Mar. 1999.
- [31] R. Pecora, “DNA: a model compound for solution studies of macromolecules.,” *Science*, vol. 251, no. MARCH 1991, pp. 893–898, 1991.
- [32] W. Helfrich, “Elastic properties of lipid bilayers: theory and possible experiments.,” *Z. Naturforsch. C.*, vol. 28, pp. 693–703, 1973.
- [33] J. Beaucourt, F. Rioual, T. Séon, T. Biben, and C. Misbah, “Steady to unsteady dynamics of a vesicle in a flow,” *Phys. Rev. E*, vol. 69, no. 1, pp. 1–17, Jan. 2004.

CHAPTER 2

2 SHEAR ORDERING OF MICELLE-NANOPARTICLE SYSTEMS UNDERGOING SHEAR

2.1 Introduction

Amphiphilic block-copolymers (BCPs) are well-known to self-assemble into micelles in solution. The micelle geometry is a function of controllable parameters including temperature, polymer structure/chemistry, concentration of polymer in solution, and the affinity of polymer blocks towards the solvent. Many of these structures exhibit lyotropic behavior, forming cubic, hexagonal or lamellae phases [1], [2]. For example, spherical micelles will assemble into face-centered cubic (FCC) or body-centered cubic (BCC) structures in an analogous fashion to concentrated colloidal suspensions [3], [4]. Under an applied shear field, these cubic micelle structures have been shown to align into a single crystal orientation, generally with the hexagonal planes parallel to the shear direction[5], [6]. When nanoparticles are included in the solution, they can become templated by the micelles, given that the nanoparticles are small enough to fit into the interstitial spaces within the micelle lattice[7]. These so-called shear-induced binary crystals are analogous to the arrangement of Na (micelles) and Cl atoms (nanoparticles) in the FCC NaCl crystal.

Shear induced ordering is an example of directed assembly; these methods applied to nanoparticles are of great interest due to the interesting and sometimes unexpected behavior of the ordered assembly. The periodic spacing and resulting

interactions can lead to new optical, electronic, and magnetic properties that have promising applications in sensors and nanoelectronics [8]–[10]. Furthermore, the top-down nature of shear-directed assembly affords a scalable synthesis for obtaining nanostructured materials and can be controlled by a number of accessible parameters.

Controllability of the degree of ordering and the type of lattice formed can be achieved by varying the strength and type of shear applied. Small-angle neutron scattering (SANS) experiments have shown that nanoparticle/micelle suspensions are mostly oriented to a single direction at even low shear rates ($1-10\text{s}^{-1}$)[7], [11]. The degree of ordering is further improved by then applying large-amplitude oscillatory shear (LAOS). However, oscillatory shear alone fails to orientate the binary crystal from its powdered state.

Limited simulation work has focused on the shear-induced templating properties of these micelle solutions. Many studies have investigated the equilibrium structures formed in solution [12], [13] but only few have looked at shear effects on micelle-forming block copolymer solutions [14], [15]. In regards to structure, these works have generally reproduced, at least qualitatively, the results from in-situ SANS shear experiments – showing sliding of hexagonal planes (spheres) and a six-fold pattern in the shear direction for both spheres and elongated micelles. Modeling work has also predicted these sliding mechanics as well as zig-zagging mechanisms in analogous colloidal crystals[16]. Lacking from these studies are the dynamic aspects and the effects from the presence of nanoparticles. Understanding the flow mechanisms and behavior of polymeric micelles in the presence of nanoparticles is essential to gaining control of the ordered phases.

While molecular dynamics (MD) would be the most accurate approach to understanding dynamics at this level, the required computational time imposes serious limitations on the time and length scales. Instead, a coarse-grained molecular dynamics (CGMD) approach offers a framework in which dynamic simulations of meso- and multi-scale systems are computationally tractable. At the heart of this model is the grouping of atoms or molecules into single particles – this is the coarsening of the system. As a direct result, the intrinsic length and time scales are increased as functions of the model’s coarseness. Thus, the potentially long time scales inherent of dynamic simulations and the disparity in length scales between solvent and nanoparticles ($\sim O(10)$), make CGMD a natural choice to study these systems.

The aim of this work is to employ CGMD to examine, at the mesoscale, the dynamics of the ordered phases produced in neat block copolymer solutions and with the inclusion of nanoparticles. We begin by studying how the structure and geometry of block copolymer micelle forming solutions are affected by shear under a variety of concentrations and hydrophilic block lengths. We then make note of the anisotropic flows surrounding micelles under steady shear and the importance of this flow for nanoparticle stability. Finally, we consider the inclusion of nanoparticles in these solutions, their dynamics, and how they affect the micelle structures.

2.2 Model Details

2.2.1 Interaction Potentials

To study the dynamics of micelle templated nanoparticle systems, we employ CGMD in a form based on the MARTINI model [17], [18]. A solvent particle in this model represents four real water molecules with a diameter $\sigma = 4.7 \text{ \AA}$. The real unit equivalents of the reduced units used in this model are presented in Table 2-1.

| MD Unit | Real Value | MD Unit | Definition | Real Value |
|------------|------------------|---------|---------------------------|----------------------------|
| σ | 4.7 \AA | τ | $\sigma\sqrt{m/\epsilon}$ | 1.78 ps |
| ϵ | 5 kJ/mol | P^* | ϵ/σ^3 | 8.00 x 10 ⁷ MPa |
| m | 72.06 g/mol | T^* | ϵ/k_B | 600K |

Table 2-1 MD Reduced Units

All polymers studied here are constructed as diblock copolymers with a hydrophilic and a hydrophobic block with monomer groupings equal in mass and size to the solvent particles. Solvent and polymer particles are modeled with a 12-6 Lennard-Jones (LJ) potential using a GROMACS style tail correction from $r_1 = 1.9149$ to 2.5 such that the energy is zero at the cut-off radius (r_c)

$$U_{ij}(r) = 4\epsilon \left[\left(\frac{\sigma}{r}\right)^{12} - \left(\frac{\sigma}{r}\right)^6 \right] + S_{LJ}(r), \quad r < r_c \quad \text{Equation 2-1}$$

$$S_{LJ}(r) = \begin{cases} C & r < r_1 \\ \frac{A}{3}(r - r_1)^3 + \frac{B}{4}(r - r_1)^4 + C & r_1 < r < r_c \end{cases} \quad \text{Equation 2-2}$$

where subscripts ij indicate the pair interaction between two different particles i and j . Bonded monomer particles are held together with a finitely extensible nonlinear elastic (FENE) potential

$$U_{FENE}(r) = -0.5KR_0^2 \ln \left[1 - \left(\frac{r}{R_0}\right)^2 \right] \quad \text{Equation 2-3}$$

in addition to a more short-ranged and purely repulsive 12-6 Lennard-Jones – the Weeks-Chandler-Andersen (WCA) potential:

$$U_{ij}(r) = \begin{cases} 4\epsilon \left[\left(\frac{\sigma}{r}\right)^{12} - \left(\frac{\sigma}{r}\right)^6 \right] & r < 2^{\frac{1}{6}}\sigma \\ 0 & r > 2^{\frac{1}{6}}\sigma \end{cases} \quad \text{Equation 2-4}$$

FENE parameters K and R_0 define the strength (energy/distance²) and bond range (distance) respectively. These were set to $K = 30.0 \epsilon/\sigma^2$ and $R_0 = 1.5 \sigma$ to mimic polymer behavior and to prevent bond dissociation[19].

Nanoparticles interact via the standard colloid potential $U_{nn}(r) = U_{nn}^A(r) + U_{nn}^R(r)$, where U_{nn}^A is the attractive NP-NP interaction and U_{nn}^R is the repulsive portion. The colloidal interaction assumes the nanoparticles are made up of a uniform distribution of Lennard-Jones particles with σ_n and ϵ_{nn} as parameters. For two spherical particles of equal radius a , the attractive portion has the form

$$U_{nn}^A(r) = -\frac{A_{nn}}{6} \left[\frac{2a^2}{r^2 - 4a^2} + \frac{2a^2}{r^2} + \ln \left(\frac{r^2 - 4a^2}{r^2} \right) \right] \quad \text{Equation 2-5}$$

where $A_{nn} = 4\pi^2\epsilon_{nn}\rho_1\rho_2\sigma_n^6$ is the Hamaker constant for nanoparticles in this formulation[20]. The values ρ_1 and ρ_2 are number densities LJ atoms making up each nanoparticle. Thus, colloidal interactions depend not only on the size of the nanoparticles, but also on the size and density of the constituent LJ atoms. In our simulations, we set ρ_1 and ρ_2 equal to each other and to the solvent density ($\rho\sigma^3 = 0.869$) implying that $A_{nn} = 29.81\epsilon_{nn}$. The repulsive portion of the potential is [21]

$$13U_{nn}^R(r) = -\frac{A_{nn}}{37800} \frac{\sigma_n^6}{r} \left[\frac{r^2 - 14ra + 54a^2}{(r - 2a)^7} + \frac{(r^2 + 14ra + 54a^2)}{(r + 2a)^7} - \frac{2(r^2 - 30a^2)}{r^7} \right]. \quad \text{Equation 2-6}$$

The same type of interaction can be derived for solvent/polymer-nanoparticle interactions. However, we have instead used a radially shifted LJ potential for these types of interactions as it allows for better control over the depth and position of the potential's minimum

$$U_{ns}(r) = 4\epsilon \left[\left(\frac{\sigma}{r - r_{shift}} \right)^{12} - \left(\frac{\sigma}{r - r_{shift}} \right)^6 \right] \quad r < r_c + r_{shift}. \quad \text{Equation 2-7}$$

The potential is infinite for values of r less than r_{shift} .

| Key | Explanation of interaction potentials |
|--------|--|
| I | 12-6 LJ: $\epsilon = 1.0$, $\sigma = 1.0$, $r_c = 2.5$ |
| II | 12-6 LJ: $\epsilon = 0.25$, $\sigma = 1.0$, $r_c = 2^{1/6}$ |
| III. A | Shifted 12-6 LJ: as (I), $r_{shift} = (a + \sigma)/2$ |
| III. R | Shifted 12-6 LJ: as (II), $r_{shift} = (a + \sigma)/2$ |
| IV | Hamaker: $\rho = \rho_w$, $\sigma_n = 1.0$, and $\epsilon_n = 1.0$. |
| * | Gromacs tail correction: $r = 1.915$ to 2.5 . |
| ^ | $\epsilon = 0.8$ |

Table 2-2 - Details of interaction parameters used in this paper.

| | W | A | B | NP |
|----|----|----|-----|-------|
| W | I* | II | I* | III.A |
| A | | I* | II | III.R |
| B | | | II^ | III.A |
| NP | | | | IV |

Table 2-3 – Interaction matrix; W = Water/Solvent, A = A-type copolymer, B = B-type copolymer, and C = colloid.

Interactions between particles are tuned by changing ϵ in the Lennard-Jones potential or the ϵ of the fictitious particles that make up the nanoparticles (effectively changing the Hamaker constant A_{nn}). A summary of all interaction parameters are shown in Table 2-2 and Table 2-3. Neutral interactions, such as solvent-solvent (W-W, A-A, B-W) have an interaction energy of $\epsilon = 1.0 kT$. Hydrophobic interactions (A-W, A-B) are created using a purely-repulsive Lennard-Jones potential with $\epsilon = 0.25 kT$. The B-B interaction was initially given a neutral A-A-like interaction, but this led to a collapsed corona as opposed to the desired solvent-swollen corona. For this reason, the B-B interaction was chosen to be repulsive with $\epsilon = 0.8 kT$. These parameters were ultimately chosen by trial and error to produce the expected micelle morphologies as a function of concentration and were matched qualitatively with experimental results available in the literature[22]. Colloidal interactions can also be tuned by careful choice of ϵ_{nn} in the Hamaker constant A_{nn} . An increase (or decrease) in ϵ_{nn} corresponds to an increase (or decrease) in the attractiveness of the NP-NP interactions. Purely repulsive NP-NP interactions are obtained by truncating the colloidal potential at its minimum. Finally, nanoparticle-solvent/polymer interactions can be tuned through ϵ in the radially shifted U_{ns} potential. The nanoparticles in this paper were given a strong solvent-NP ($\epsilon_{ns} = 2.0$) interaction to hydrate the particles but not so strong that solvent layers formed at the nanoparticle surface.

2.2.2 Dissipative particle dynamics

Temperature is kept constant using a dissipative particle dynamics (DPD) thermostat [23]. In traditional DPD, the equations of motion are solved with two additional forces

$$\frac{d\vec{p}}{dt} = \sum_{i \neq j} \vec{F}_{ij}^C + \sum_{i \neq j} \vec{F}_{ij}^D + \sum_{i \neq j} \vec{F}_{ij}^R \quad \text{Equation 2-8}$$

The two forces added in addition to the conservative forces, \vec{F}^C , are the dissipative force, \vec{F}^D , and the random force, \vec{F}^R , which serve as a heat sink and source, respectively. The dissipative force acts along the vector connecting the particles and has the form

$$\vec{F}_{ij}^D = -\zeta \omega^2(r_{ij})(\vec{v}_{ij} \cdot \hat{r}_{ij})\hat{r}_{ij} \quad \text{Equation 2-9}$$

where ζ is a friction parameter and $\omega(r)$ is a weighting function. The friction parameter was set to $1.0\tau^{-1}$, but measured transport properties were not found to be sensitive to reasonable choices of ζ . The weighting function has the simple form $\omega(r) = 1 - r/r_c$ with $r_c = 2.5\sigma$. The random force is defined as

$$\vec{F}_{ij}^R = \sigma_N \omega(r_{ij}) \xi_{ij} \hat{r}_{ij} \quad \text{Equation 2-10}$$

where σ_N is a noise parameter representing the root mean square of the thermal fluctuations and ξ_{ij} is a Gaussian random number with zero mean and unit variance.

From the fluctuation-dissipation theorem

$$\sigma_N = \sqrt{2k_B T \zeta} \quad \text{Equation 2-11}$$

where k_B is the Boltzmann constant.

$$\omega(r) = 1 - r/r_c \quad \text{Equation 2-12}$$

DPD is chosen as a thermostat in these systems because it conserves momentum between particles and therefore captures any hydrodynamic effects. With the DPD parameters we used, shear rates above a value of $\dot{\gamma} = 0.1\tau^{-1}$ led to an increase in the system temperature beyond the set point. The results of this work are therefore restricted to shear rates an order of magnitude smaller (see Table 2-4).

2.3 Simulation Details

All simulations were performed using the open-source molecular dynamics package LAMMPS distributed by Sandia National Labs.[24]

2.3.1 Method and validation

The simulation parameters discussed here are summarized in Table 2-4. A cubic box of side length 33.28σ with periodic boundaries (PB) on all faces was used for all results presented here unless otherwise stated. The box size was chosen to be large enough to allow for multiple micelle formation and for larger structures to form under shear, but small enough for the simulations to be computationally tractable. Shear was applied through a constant triclinic deformation in LAMMPS with particle velocities remapped when a shear-gradient boundary is crossed. This implementation is equivalent to the classic Lees-Edwards boundary conditions.

The system number density was chosen such that the solvent density in real units is 1 g/cm³ ($\rho^* \sigma^3 = 0.868$). This density is applied to the polymer-solvent matrix and is held constant. With this constraint, the total number of matrix particles decreases to compensate for the volume of added nanoparticles. All simulations are relaxed from a random configuration using soft potentials. Further relaxation using full 12-6 Lennard-Jones potentials is applied before setting the individual interaction parameters. All relaxations are performed at $T^* = 1.0 k_B T$ (600K) and all main-run simulations are performed at $T^* = 0.5 k_B T$ (300K). The time step used for MD integration was 0.01τ (17.6 fs) – a more conservative choice as compared to the 50 fs time step used by Marrink et al.[17]

| Symbol | Definition | MD Value | MD Units | Real Value | Real Units |
|----------------|------------------------------|-----------------|------------------|---------------------------|-------------------------|
| L | Box Length | 33.28 | σ | 15.64 | nm |
| ρ^* | Number Density | 0.8685 | σ^{-3} | 1 | g/cm³ |
| T^* | Temperature | 0.5 | ϵ/k_b | 300 | K |
| D^* | Measured Solvent Diffusivity | 0.0719 | σ^2/τ | 1.484×10^{-9} | m²/s |
| η_0^* | Measured Solvent Viscosity | 5.99 | $P^* \cdot \tau$ | 8.5×10^{-4} | Pa · s |
| $\dot{\gamma}$ | Shear Rate | 0.001-0.01 | τ^{-1} | $5.69 \times (10^8-10^9)$ | s⁻¹ |

Table 2-4 – Simulation Parameters

The solvent was measured to have a diffusivity of $D^* = 0.0120 \sigma^2/\tau$ ($1.484 \times 10^{-9} \text{ m}^2/\text{s}$) and a zero-shear viscosity of $\eta_0^* = 5.99 P^* \cdot \tau$ ($8.5 \times 10^{-4} \text{ Pa} \cdot \text{s}$). The actual measured experimental values for water at 300K are $D = 2.40 \times 10^{-9} \text{ m}^2/\text{s}$ [25] and $\eta_0 = 8.53 \times 10^{-4} \text{ Pa} \cdot \text{s}$ [26]. The small disagreement in the diffusivity is consistent with the MARTINI model and is acceptable for our purposes.

2.3.2 Structural analysis

Order in the systems studied here is quantified using a 2D static structure factor in its explicit form

$$S(\mathbf{k}) = \frac{1}{N} \left\langle \sum_i^N \sum_j^N e^{-i\mathbf{k}(\mathbf{r}_i - \mathbf{r}_j)} \right\rangle \quad \text{Equation 2-13}$$

where \mathbf{k} is a 2D wave vector whose magnitude $|\mathbf{k}|$ is limited to values of $n\pi/L$ due to the periodic boundaries. The brackets indicate an average over many simulation snapshots after steady-state has been reached. The positions \mathbf{r} can be projected onto a plane of choice – here they will always be projected onto the gradient-vorticity plane. The structure factor models the scattering pattern that would be obtained from those particles in a scattering experiment. Hence, the static structure factor is a natural choice for direct comparison to published experimental results. The average is taken over a number of snapshots during the steady-state duration and can be performed over any set of particles. Here, structure factors are only calculated for micelle centers of mass, which is generally acceptable because micelle projections are circular in the plane of interest.

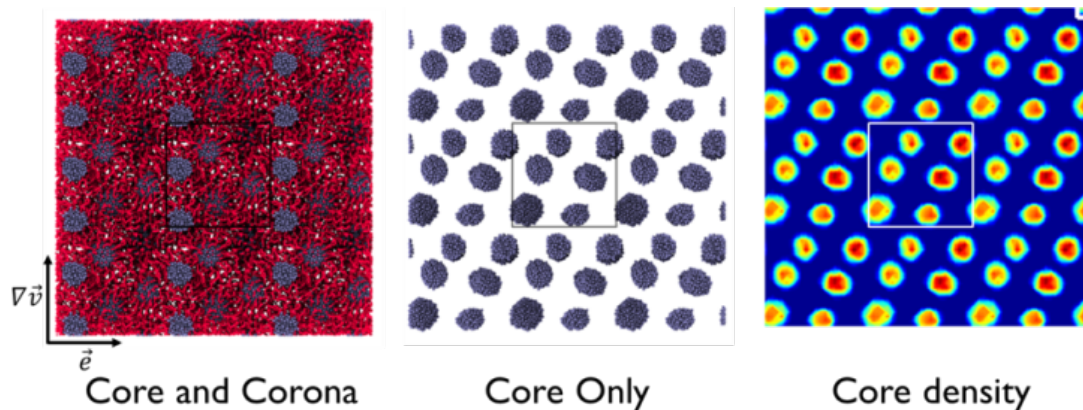


Figure 2-1 – Example of a 2D density projection calculated by projecting the 3D micelle-core density into two dimensions. Notice that brighter colors indicate greater density in the flow direction – information which is not available in the core-only projection.

In the formulation employed here, the structure factor only provides accurate information about the spatial order in systems -- it does not give information about micelle geometry. A method we employ to more clearly show both structural and geometrical qualities is to “flatten” the system into a density-based contour map. This result can then be replicated in both the x and y directions to clarify the order in the system. A white-outlined box indicates the size of the actual simulation box in all such figures. For this paper, the density projections are drawn only for the core particles. Steinhardt bond-order parameters are used to quantify 3D structure -- they have the form [27]

$$\psi_l(i) = \sqrt{\frac{4\pi}{2l+1} \sum_{m=-l}^l |q_{lm}(i)|^2} \quad \text{Equation 2-14}$$

The complex vector $q_{lm}(i)$ can be defined from the spherical harmonics Y_{lm} as

$$q_{lm}(i) = \frac{1}{N_b(i)} \sum_{j=1}^{N_b(i)} Y_{lm}(\mathbf{r}_{ij}) \quad \text{Equation 2-15}$$

Here, N_b is the number of nearest neighbors to particle i , which are determined by a voronoi tessellation on micelle centers of mass. An average value $\langle \psi_l \rangle$ is obtained by considering all micelles in the system.

2.4 Results and Discussion

The results here are divided into two main categories. First we discuss systems of neat polymer solutions in the quiescent and sheared state followed by how flow dynamics are important and affected by the micelle corona. Next, we discuss the influence of nanoparticles on the morphology and structure of the micelles and the stability of these systems.

2.4.1 Micelle formation in neat polymer solutions

2.4.1.1 Quiescent systems

In the quiescent state, simulated diblock copolymers (A6B12, A6B9, A6B6, and A6B3) spontaneously assemble into micelle structures with a concentration dependent morphology. The resultant micelles, regardless of the hydrophilic block length, do not exhibit polymer exchange within the time frame of these simulations (2000τ or 3.56ns) and are thought to be kinetically frozen [28]. This conclusion is supported by the fact that the application of shear induces micelle-micelle fusion events and that these new, larger micelles are stable after the cessation of shear. A kinetic limitation should not be an issue for the purposes of our study as we are more interested in the behaviour of the micelles as a whole as opposed to their assembly dynamics. In fact, a more efficient approach may be to treat the micelles as “soft” colloids with effective interactions derived from all-atom or coarse-grained results in an analogous fashion to work that has been done with star-polymers [29].

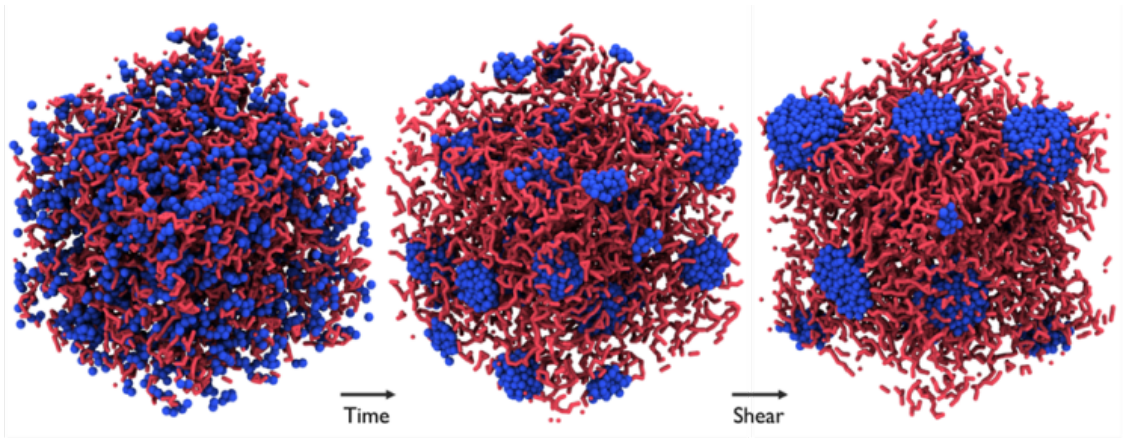


Figure 2-2 – Snapshots for a 30% neat polymer solution at three stages of micelle formation (solvent omitted for clarity). First is the random starting configuration. Second is the non-sheared ‘equilibrated’ morphology. Third is the shear-induced morphology at $\dot{\gamma} = 0.002\tau^{-1}$. In each case, the snapshots were chosen after the system reached its stable state where the micelles were no longer changing in the duration of the simulations.

2.4.1.2 Sheared Systems

Shear in these systems, even at the lowest rates tested ($\dot{\gamma} = 0.001\tau^{-1}$), is substantial enough that convection dominates and micelles become deformed from their equilibrium morphologies. Such tendencies can be described by the dimensionless Péclet number ($Pe = \dot{\gamma}R_M/D_M$) and Weissenberg number ($Wi = \dot{\gamma}\tau_R$); here, R_M is the average micelle radius, D_M is the micelle diffusion coefficient determined from mean-squared displacement data for micelle centers-of-mass following the cessation of shear and τ_R is the longest relaxation time of the micelles. At $\dot{\gamma} = 0.002\tau^{-1}$, values for Pe generally fall between $Pe = 10 - 100$ (for the solvent

$Pe = 0.04$). From the simulations performed, the longest micelle relaxation times yield values for Wi between 3 and 10.

In the sheared state, the micelle solutions relax into concentration-dependent stress minimizing configurations as seen in Figure 2-1. Six-fold symmetries are usually observed in the gradient-vorticity plane (the other two planes often show staggering of micelles and sliding plane formation, but no clear order). Both visual inspection and the presence of higher order peaks in structure factor indicate the highest degree of order for polymer concentrations of 40% and 100%. These systems are composed of non-spherical micelles: the 40% solution having elongated micelles with aspect ratios of 2-3:1 in the flow-direction whereas the 100% solution having purely flow-aligned hexagonal cylinders (periodic boundary crossing). Despite these differences, the micelle cross-sections are circular in the gradient-vorticity plane, giving rise to similar 2D micelle arrangement. In contrast, the spherical micelles observed in 30% solutions show slight oscillations between several simple six-fold oblique lattice structures in the vorticity-gradient plane similar to previous simulation work [14]. Interestingly, the 50 and 60% solutions are best approximated by a quasicrystal truncated square tiling with the relatively smaller micelles forming the octagonal vertices, and the largest, cylindrical micelle placed in the center.

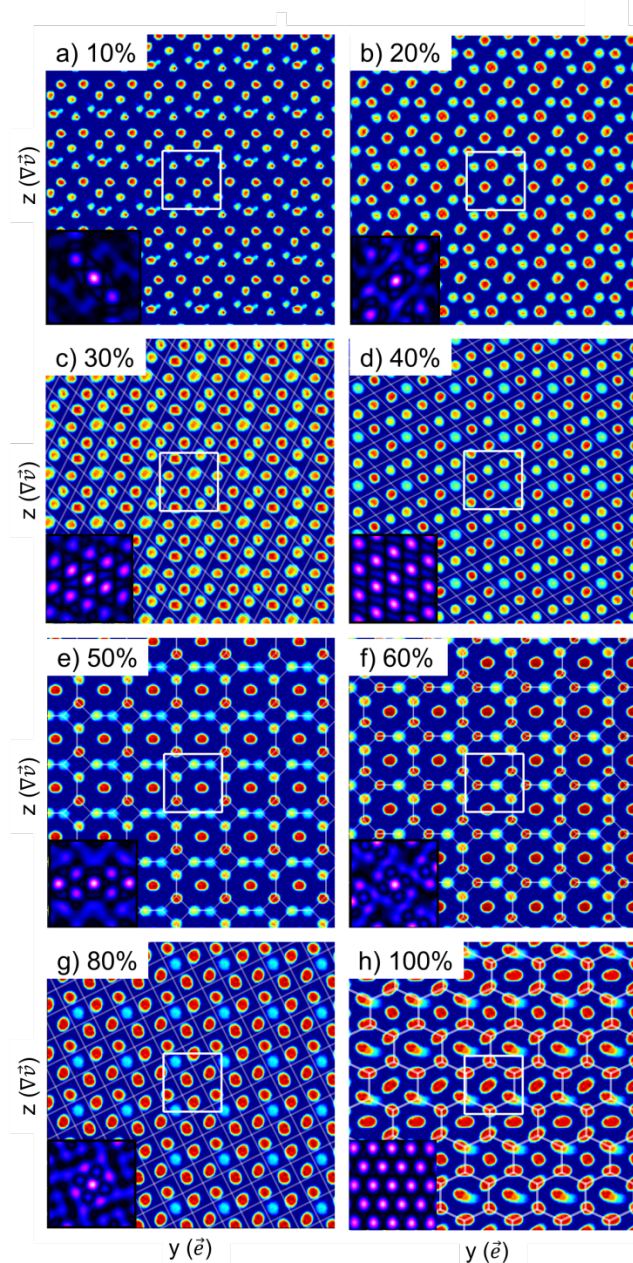


Figure 2-3 – Sheared ($\dot{\gamma} = 0.002 \tau^{-1}$) structures of BCP solutions formed as a function of concentration. 10% (a) and 20% (b) states show no discernible lattice configuration. (c) 30% shows an unstable oblique lattice while the 40% solution (d) shows a stable oblique lattice. 50% (e) and 60% (f) solutions show a stable truncated

square tiling with cylindrical micelles at the tile centers. (g) 80% shows a stable square lattice and (h) 100% shows a stable hexagonal lattice.

The structure of the sheared state is dependent on the strength of the shear-field as can be seen in Figure 2-4 and Figure 2-5. As shear rate is increased in a 30% polymer solution, the micelles elongate, thereby reducing the size of their vorticity-gradient cross-section. They further display strong six-fold symmetry in this same plane. The six-fold pattern is similar to what is seen in experiments[5] and simulations[14] where it is explained as the sliding of 2D hexagonally close-packed (HCP) layers parallel to the flow-vorticity plane. Although we observe sliding planes, we generally do not find 2D HCP order in any plane orthogonal to the gradient-vorticity plane. This disagreement may be a consequence of the simulation box size and is discussed further later. Although not shown, scattering peaks indicative of two-fold symmetry appear in the vorticity-gradient plane as shear rate increases. When shear rate is increased even further ($0.008\tau^{-1}$), parallel planes of micelles organize perpendicular to the vorticity direction. This is a result also seen in previous simulation work[14]. At this transition point, elongation of the micelle morphology in the gradient-flow plane precludes organization into a neat 3D structure. However a stable oblique lattice is seen in the vorticity-gradient plane with the (1,0) direction parallel to the gradient direction.

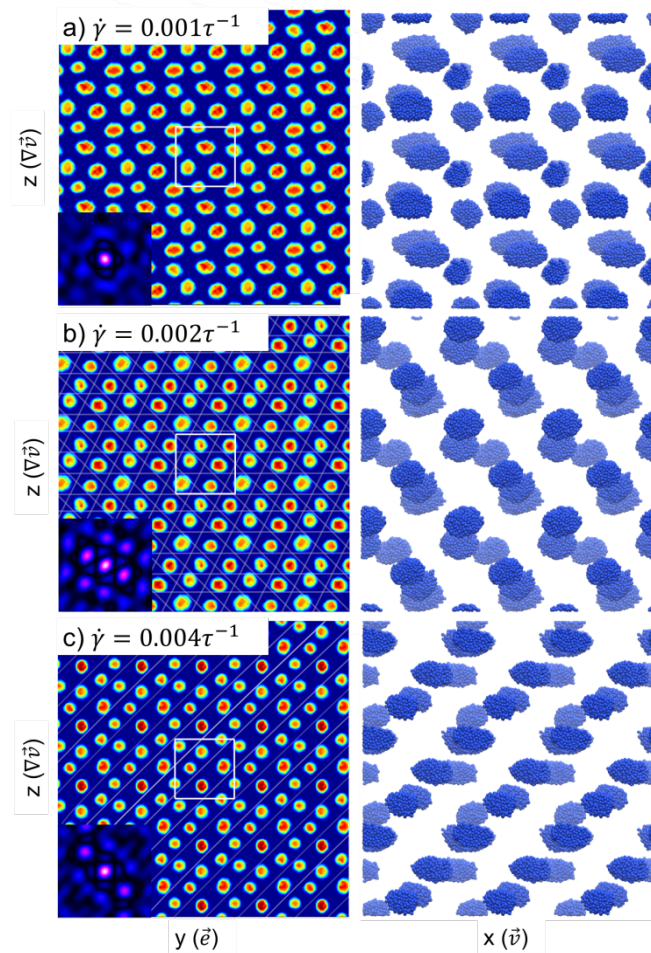


Figure 2-4 – (Left) Gradient-vorticity plane structures of BCP solutions formed at lower shear rates (a) $0.001\tau^{-1}$, (b) $0.002\tau^{-1}$, and (c) $0.004\tau^{-1}$. The insets show time-averaged structure factors in the same plane as the density projections. (Right) Gradient-shear snapshots (with 3x3 duplicates for clarity) showing mostly spherical or slightly elliptical micelle morphologies.

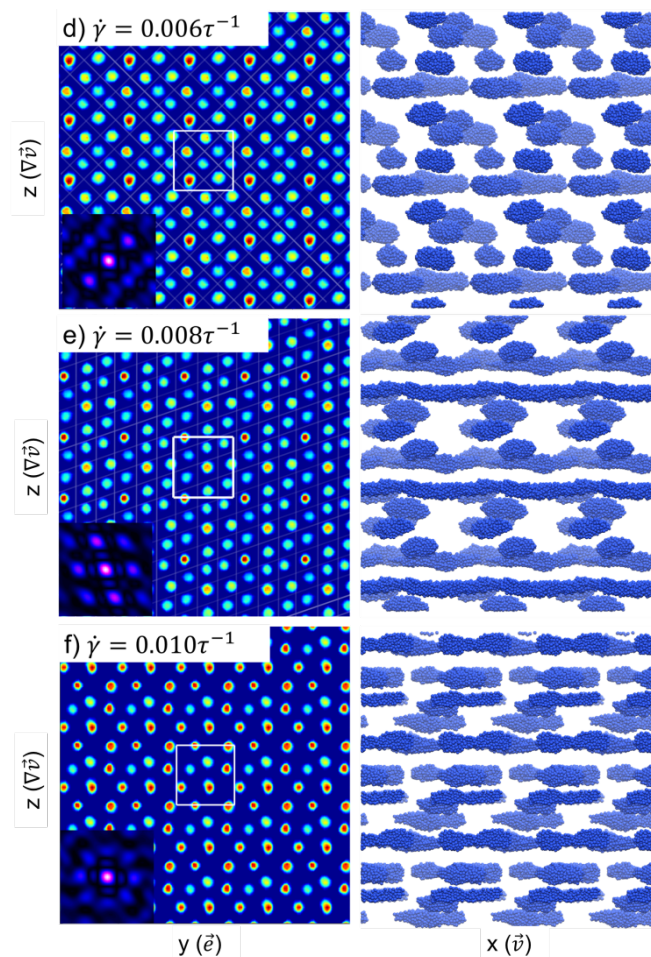


Figure 2-5 – (Left) Gradient-vorticity plane structures of BCP solutions formed at higher shear rates (a) $0.006\tau^{-1}$, (b) $0.008\tau^{-1}$, and (c) $0.01\tau^{-1}$. (Right) Gradient-shear snapshots (with 3x3 duplicates for clarity) showing the sphere to elongated morphology transition that occurs at higher shear rates.

2.4.1.3 The effect of the corona length

The role of the micelle corona was investigated by running both quiescent and simple shear simulations on polymers with differing hydrophilic block lengths. The hydrophobic block length and overall polymer particle concentration were kept constant. Three corona lengths were probed in addition to the 12-particle block (A6B12) and are shown in

Figure 2-6: a 9-particle (A6B9), 6-particle (A6B6), and 3-particle (A6B3), giving total polymer lengths of 15, 12, and 9 respectively.

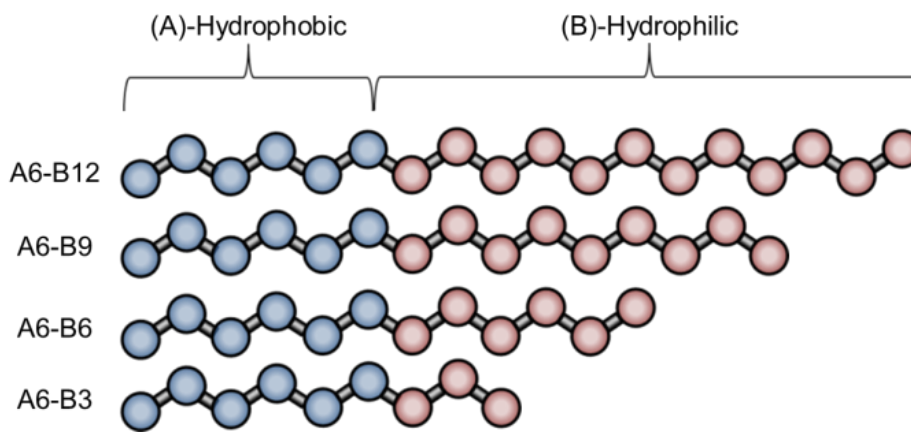


Figure 2-6 – Schematic of different hydrophilic block lengths used in the corona length study.

The quiescent behaviour of the A6B9 and A6B6 polymers was qualitatively similar to the A6B12 system. Each formed 18-22 kinetically arrested micelles with similar aggregate size distributions. In contrast, the shortest hydrophilic block length, A6B3, formed only 8 micelles with a significant variation in aggregate size.

Shear applied at a rate of $\dot{\gamma} = 0.002\tau^{-1}$ led to significant aggregation of the quiescent micelles for all hydrophilic block lengths. In the A6B12 system, six spherical micelles ultimately formed, each with similar aggregate sizes, whereas in the 9, 6, and 3 corona-length polymer systems, only five micelles formed with broader size distributions. Each of the shorter corona systems also shows at least one micelle elongated into the flow direction. Elongation in these systems is not surprising when one considers the presence of the larger aggregates (relative to the A6B12 system).

For example, the A6B6 polymer solution contained an aggregate of ~ 2700 particles, compared to the largest aggregate in the A6B12 system of fewer than 2000 particles.

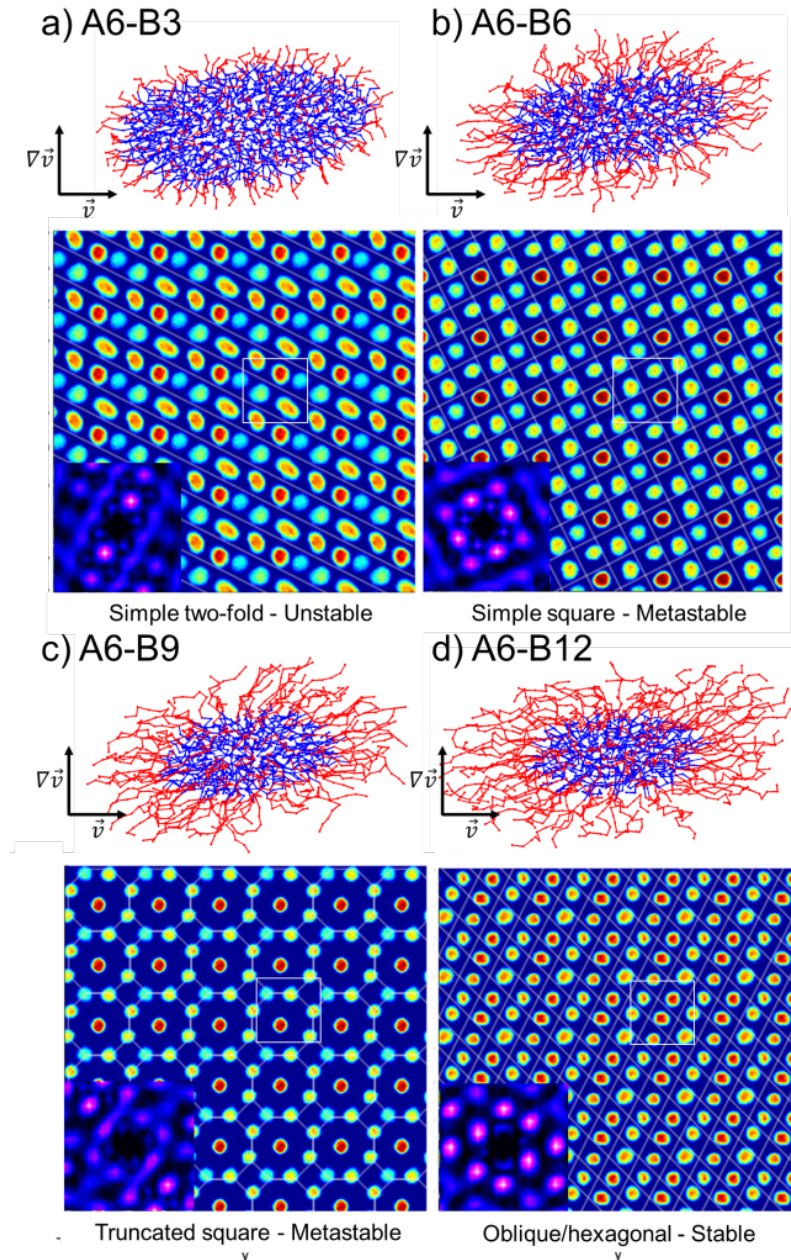


Figure 2-7 – Sheared ($\dot{\gamma} = 0.002 \tau^{-1}$) structures of BCP solutions formed as a function of hydrophilic-block length. (a) A6B3 – Unstable oblique lattice; snapshot here showing two-fold order. (b) A6B6 – Metastable square lattice, snapshot chosen to

show square lattice, but other snapshots show a less or more ordered state. (c) A6B9 – Stable truncated square tiling with cylindrical micelle at the tile center. (d) A6B12 – Stable oblique lattice, indicated by the strong peaks in the time-averaged structure factors.

Figure 2-7 shows the 2D lattice configurations formed under shear as a function of the hydrophilic block length. Of the four corona lengths, the A6B12 system showed the highest degree of ordering, forming a stable oblique lattice oscillating in and out of alignment. The shorter corona length systems also show order, but to a lesser extent. In the case of the shortest corona, A6B3, the symmetry was only two-fold, and fluctuated, whereas the A6B6 system formed a metastable square lattice. Interestingly, the A6B9 system contained one large, nearly cylindrical micelle, surrounded by smaller spherical micelles in a truncated square tiling. This structure is similar to the structures that formed at concentrations of 50 and 60%, where a single cylindrical micelle and several elongated micelles co-existed.

2.4.1.4 Flow around micelles and the effect of the corona length

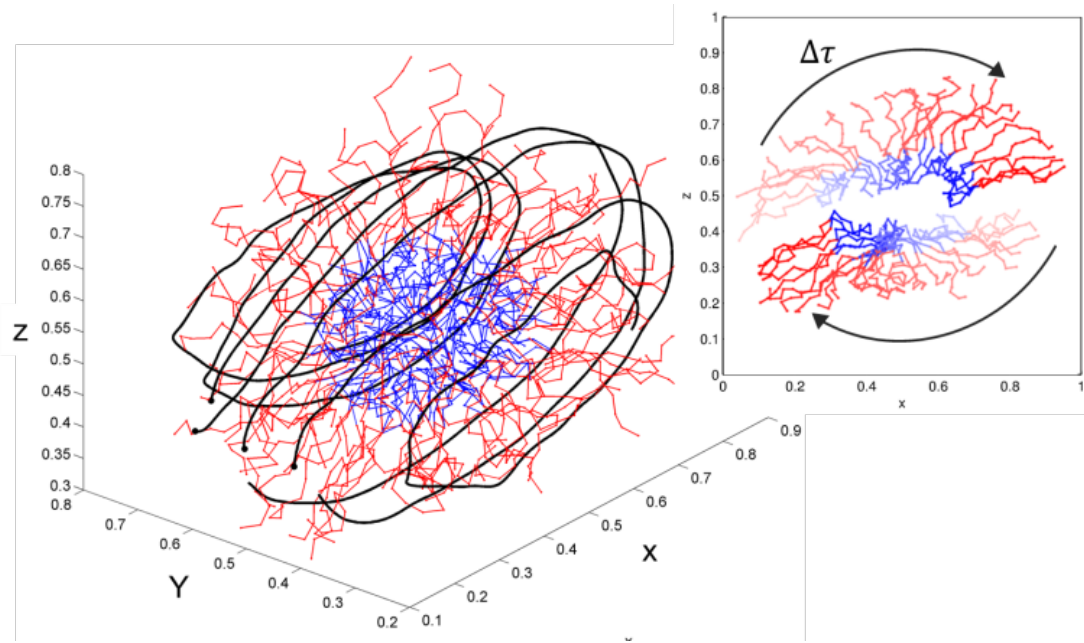


Figure 2-8 – Selected streamlines for a sheared ($\dot{\gamma} = 0.002 \tau^{-1}$) A6B12 micelle containing 1764 polymer particles. The streamlines show the rotational behaviour of the fluid surrounding the micelle. The inset figure demonstrates the tank-treading behaviour by tracking two micelle polymers in time.

Micelles in our simulations participate in dynamic flow behaviour that includes trembling, tank-treading, and stretching. Stretching and eventual fission/fusion dynamics are generally restricted to highly non-spherical micelles or spherical micelles undergoing a transition to an elongated, steady-state geometry. Trembling, or a vacillating-breathing behaviour, is seen in many of the micelles and can be described as an initial rotation of the micelle into declined orientation (negative inclination) to the shear-field, followed by a compression of the micelle and a stretching into a positive inclination. This behaviour is similar to what is observed with vesicles under simple shear fields[30], [31]. Tank-treading is present for all micelles undergoing

shear flow and leads to anisotropy in the surrounding solvent flow as shown in Figure 2-8 and Figure 2-9. This anisotropy is easily understood when one considers that the corona is solvated, and hence, solvent particles are conveyed by the tredding motion of the corona. The resulting flow field forms two hyperbolic stagnation points in the flow-direction that straddle the micelle. Outside of these stagnation points is a flow reversal in the form of a counter-rotating vortex. These are flow characteristics similar to that of a freely rotating sphere or elliptical cylinder in shear flow [32], [33] and closely resemble simulated star-polymers at moderate Weissenberg numbers [34]. However, the presence of multiple micelles and moderate polymer concentrations make our simulations significantly more complicated than previous flow studies. Indeed, preliminary simulations on single micelles in the same shear field suggest that the aforementioned trembling behaviour is a direct consequence of micelle-micelle dynamics.

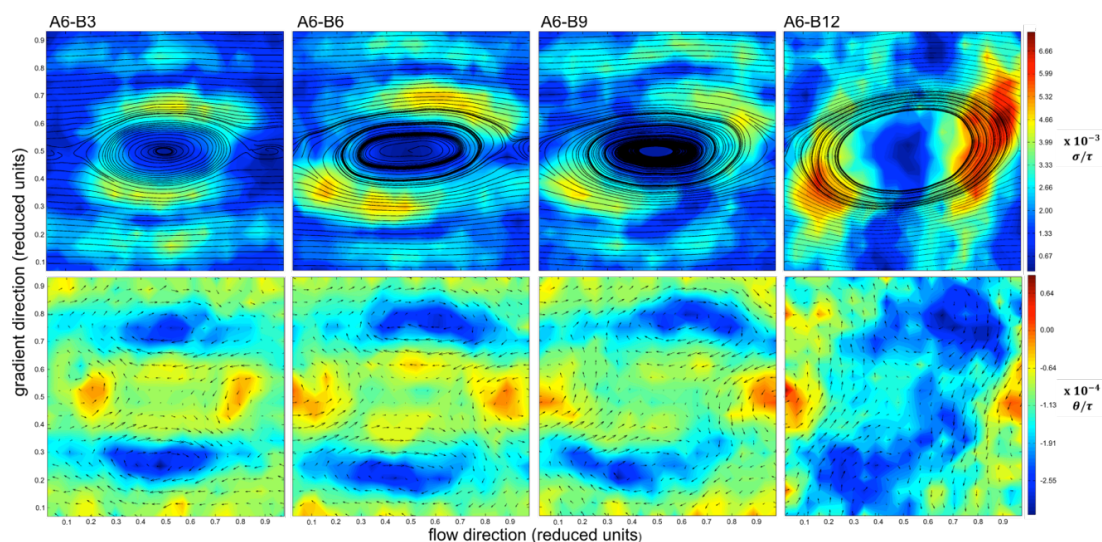


Figure 2-9 – Disturbance to a linear shear flow profile as a function of corona length for selected micelles. The micelle sizes from left to right are: 1548, 1968, 1980 and

1764 particles. Note that identical micelle sizes were not available across all four systems. Top row shows the flow streamlines superimposed over a contour plot of the magnitude of the deviation (for reference, the wall velocity would be $0.0287 \sigma/\tau$). Bottom row shows the disturbance vector field superimposed over the angular velocity.

Notably, stagnation points are only seen for small micelles and those with the shortest corona length. Larger micelles (or larger coronas) have a correspondingly larger disturbance field, as seen in Figure 2-9. The extent of this disturbance reaches the periodic bounds of the simulation box and is therefore self-interacting. The micelle self-image becomes the counter rotating vortex with a stagnation point on the boundary. A larger simulation wherein the box size was doubled confirms that this is a finite size effect, and not intrinsic nature resulting from the larger size of the micelle or corona. In that simulation, two discrete flanking stagnation points appear with corresponding regions of flow reversal.

2.4.2 Dynamics of Micelle/Nanoparticle Systems

Nanoparticles were added to several polymeric systems based on similarities to previous experimental work and candidacy to serve as templates. For the 30% solution, nanoparticles were varied in number and size to determine whether a combination of the two parameters would yield a templated structure. As a starting point, the one-to-one of assumption of a completely filled binary crystal lattice was used. Since there are typically 5-7 micelles in the simulation box, the nanoparticle number was varied between 2 and 10. Similarly, the diameter of the nanoparticles was chosen based on the assumption that nanoparticles would be occupying these

interstitial sites in the micelle lattice – the diameter being a function of the micelle lattice formed. In an FCC lattice, octahedral sites are 0.414 of the hard-sphere diameter, and tetrahedral sites 0.225 of this diameter. The dense cores of the spherical micelles have an approximate diameter of 10σ . However, the diffuse corona surrounding the core increases the effective diameter of the micelles, making it difficult to define an exact micelle diameter. Nonetheless, the range of nanoparticle diameters was broad with values between 4 and 10σ .

2.4.2.1 The dynamic interaction between micelles and nanoparticles

In nearly all the sheared systems in which nanoparticles were added, translational motion in the gradient-vorticity plane was significant, contrary to what is observed with the neat micelle solutions. Furthermore, nanoparticles exhibited a tendency to flow around the micelles as opposed to occupying stable positions relative to the micelles. As previously described, the presence of a stagnation point relative to any given micelle depends on the size of the micelle and the length of the corona. Large micelles, or those having long coronal chains, tend to have flow-field perturbations on the order of the simulation box length. Smaller micelles, or those having short coronal chains, often have flanking stagnation points in-line with the flow direction. In particular, the stagnation points around micelles in the A6B3 system have been observed serving as metastable occupation sites for nanoparticles. However, for the nanoparticles studied, occupation of these sites is transient, with perturbations leading to translational motion away from the stagnation point as seen in Figure 2-10.

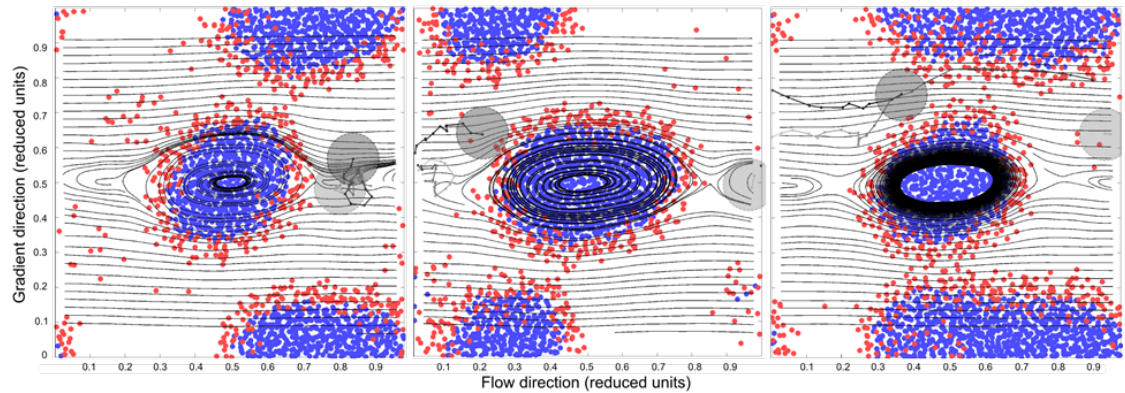


Figure 2-10 – Examples of nanoparticle stability relative to several different A6B3-type micelles. The light-to-dark paths indicate the position of the nanoparticle at various times. (Left) A stable nanoparticle within the sample timeframe near the stagnation point of a 1143 particle micelle. (Middle) A nanoparticle perturbed from an initially metastable stagnation/vortex region surrounding a 1737 particle micelle. (Right) An unstable nanoparticle moving between two micelle lanes.

The nanoparticles here are modelled with point-particle type potentials and therefore lack any rotational freedom – another factor influencing nanoparticle instability. As a result, perturbations can only be dissipated through translational motion of the nanoparticle. For example, the observed rotational flow surrounding stagnation points (see Figure 2-10) will have the tendency to dislodge particles whose radius is comparable to the vortex unless they are somehow able to accommodate the flow. This problem could be easily overcome by switching to a particle-surface model for the nanoparticles whereby the flow could affect a torque and hence induce rotational motion.

2.4.2.2 B.2. The effect of NPs on micelle morphology and ordering

The presence of nanoparticles in the 30% polymer solutions affected micelle structure, but no clear evidence of nanoparticle ordering was observed. Visual inspection shows that the nanoparticles generally maintained freedom of movement within the space between micelle cores (corona and solvent). Nanoparticle diffusion has been suspected by other authors as an explanation for weaker nanoparticle organization as seen in scattering experiments[11]. The nanoparticle movement we observe is more dynamic than simple diffusive behaviour and is subject to the flow fields previously noted.

In some cases, the micelles relaxed into more well defined structures when compared to the nanoparticle-free system at the same concentration. Although all the corona lengths were not tested with nanoparticles, the A6B3 system discussed in this same context earlier showed a transition to a more well-ordered micelle state following the inclusion of nanoparticles (see Figure 2-11). When 5 nanoparticles with diameters of 6σ were included, the micelles became hexagonally packed in the gradient-vorticity plane. When larger 8σ particles were added instead, the structure became transitory, but the average structure factor still shows increased ordering.

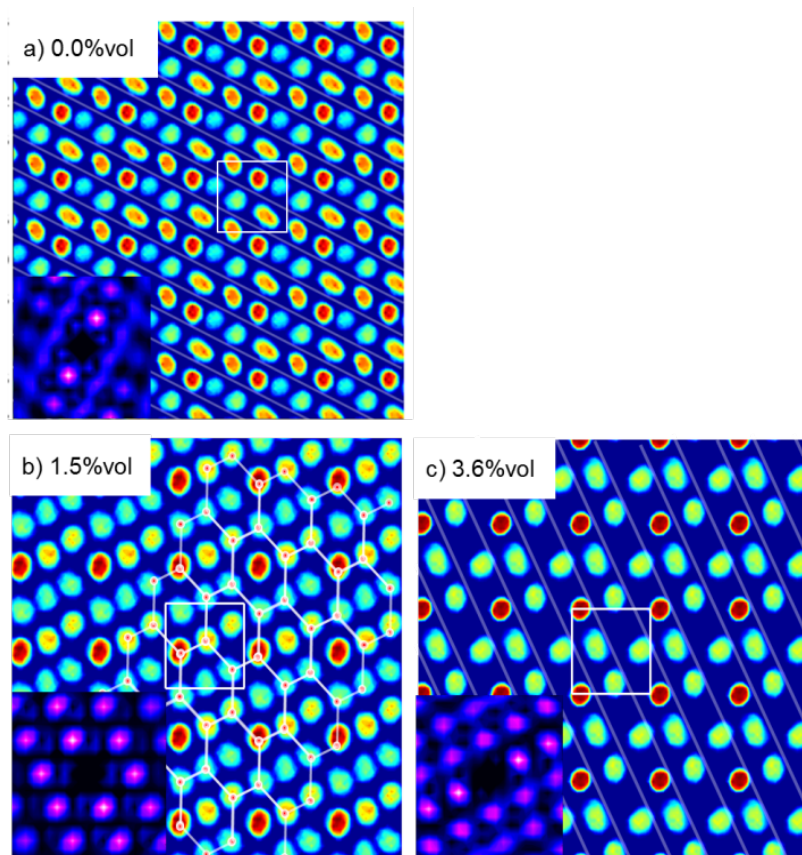


Figure 2-11 – The effect of nanoparticles on the structural organization of the A6B3 micelles. The nanoparticle-free system is included for reference. Note that 1.5 vol% corresponds to five particles with diameters of 6.0σ , where as 3.6 vol% corresponds to the same number of particles but with diameters of 8.0σ .

Nanoparticles with diameter 6σ and numbering 5 and 10 were included in a 40% polymer solution due to its propensity to form elongated/rod-like micelles and very well defined order in the shear direction. The lengthened morphology of the individual micelles and the overall higher concentration of polymer also reduce the translational freedom of the nanoparticles. Again, our results show that the nanoparticles still move relatively freely within the cavities and are not templated into

a neat structure. However, the presence of nanoparticles in these solutions induced aggregation of some micelles into boundary-crossing cylindrical morphologies. As a direct consequence, the micelles reorganized into a shear-aligned close-packed hexagonal configuration.

2.4.2.3 Post-shear micelle ordering

Three-dimensional order is observed in the A6B12 system and its smaller counterpart, A3B6, following the cessation of shear. In the A6B12 system, the 3-D structure is a simple rhombic crystal whereas a mixed crystal is seen for the A3B6 system. In both cases, calculated bond-order parameters of the centers of mass indicate the development of 3-D order from a previously 2-D only configuration which can be seen by the clear separation of bond-order parameters in Figure 2-12 following the cessation of shear. A similar effect has been observed in simulations of soft-colloids in supercooled liquids which develop into an FCC lattice following a sheared state where 2D hexagonal order is present with string formation in the flow direction[35].

The addition of 5 nanoparticles (1.5%vol) of diameter 6σ to the A6B12 simulation yielded slightly different shear and post-shear results as compared to the neat solution. In particular, a smaller number of larger micelles formed yielding a broader size distribution. The sheared state shows a nearly perfect square lattice in the gradient-vorticity plane as opposed to the six-fold structure seen in the neat solution. Moreover, the cessation of shear allows the system to relax into a cubic organization, with the smallest micelle existing as a defect. At this time, it is not clear as to whether the presence of nanoparticles is responsible for the changes in the micelle morphology.

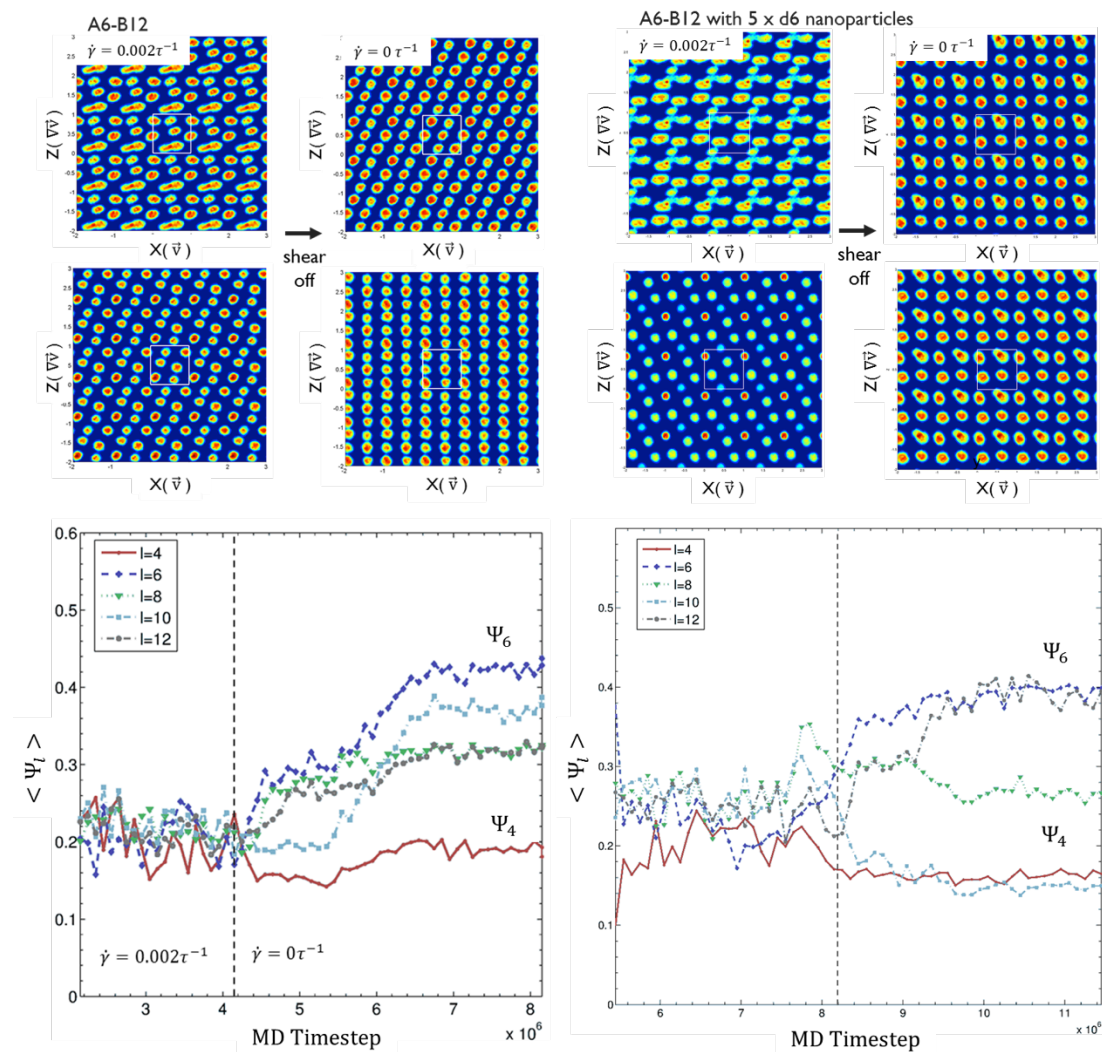


Figure 2-12 – Comparison of shear and post-shear structure in a neat A6B12 solution (left) and a A6B12 system with 5 (1.5%vol) diameter 6σ nanoparticles (right). Below are plotted bond-order parameters (Ψ_l) calculated from micelle centers of mass as a function of timestep. Under shear, the bond-order parameters are constant and equal. Following shear, there is sharp separation of the different Ψ_l 's, indicative of 3-D organization. y-axis scales are the same; x-axis scales are different by a factor of two. Notice the square lattice formed with the nanoparticles included instead of a rhombic

lattice of the neat solution. Averaged bond-order parameters (Ψ_l) calculated from micelle centers of mass as a function of timestep.

Shear cessation in the A6B3 system, with or without nanoparticles, does not lead to any stable 3-D structure in our simulations. In fact, the 2-D order that existed under shear deteriorates relatively quickly as diffusion forces takeover. The shorter corona appears to decouple micelle-micelle interactions leading to increased translational freedom and thereby precluding the possibility of a stable 3-D structure. Another factor affecting the lack of a neat crystal structure is the broader distribution of micelle sizes in the A6B3 system as compared to the A6B12 system or A3B6 systems. Any well-organized structure would need to accommodate the inhomogeneous micelle sizes, and with the only six micelles, we would not expect to see any such structure.

2.5 Conclusions

A coarse-grained molecular dynamics (CGMD) model is applied to systems of amphiphilic diblock copolymers and nanoparticles to study their dynamic (shear) behaviour. Self-assembly into micelles is a spontaneous process in this model. As a function of concentration, the observed micelle morphologies agree qualitatively with morphologies seen experimentally and in other simulation work for similar polymers. When the hydrophobic polymer block is held at a constant length of 6 particles, the length of the micelle corona plays an important role in the shear morphologies obtained. Generally, more unstable structures are favoured when the corona is short. Thus, the interactions between micelles with longer corona chains appear to be

stabilizing at moderate shear rates. However, the shear-induced micelle dynamics, especially the so-called “tank-treading” motion, leads to a flow disturbance similar to that of Stokes flow around a freely rotating ellipsoid or flow around star polymers at moderate Weissenberg numbers. This disturbance is rotational and enhanced in magnitude and radius with increasing corona length. The nanoparticles used in this study are intrinsically irrotational and are therefore incapable of accommodating rotational flow without translational motion and thus are generally unstable. Nanoparticles do influence the micelle structures formed under shear despite their own lack of organization. Indeed, the addition of a low volume fraction of moderately sized nanoparticles appears to enhance the stability of an otherwise unstable 2D structure. Future work should focus using nanoparticles with rotational freedom and shear rates that do not create significant disturbances to the surrounding flow-field.

REFERENCES

- [1] G. Wanka, H. Hoffmann, and W. Ulbricht, "Phase diagrams and aggregation behavior of poly (oxyethylene)-poly (oxypropylene)-poly (oxyethylene) triblock copolymers in aqueous solutions," *Macromolecules*, pp. 4145–4159, 1994.
- [2] P. Alexandridis, "Poly(ethylene oxide)/poly(propylene oxide) block copolymer surfactants," *Curr. Opin. Colloid Interface Sci.*, vol. 2, no. 5, pp. 478–489, Oct. 1997.
- [3] C. Murray, C. Kagan, and M. Bawendi, "Self-organization of CdSe nanocrystallites into three-dimensional quantum dot superlattices," *Science (80-.)*, vol. 270, no. November, pp. 1335–1338, 1995.
- [4] E. V Shevchenko, D. V Talapin, C. B. Murray, and S. O'Brien, "Structural characterization of self-assembled multifunctional binary nanoparticle superlattices.," *J. Am. Chem. Soc.*, vol. 128, no. 11, pp. 3620–37, Mar. 2006.
- [5] G. McConnell, M. Lin, and A. Gast, "Long range order in polymeric micelles under steady shear," *Macromolecules*, pp. 6754–6764, 1995.
- [6] K. Mortensen, "Structural studies of aqueous solutions of PEO-PPO-PEO triblock copolymers, their micellar aggregates and mesophases; a small-angle neutron scattering study," *J. Phys. Condens. Matter*, vol. 103, no. 8, pp. A103–A124, 1996.
- [7] D. C. Pozzo and L. M. Walker, "Shear Orientation of Nanoparticle Arrays Templated in a Thermoreversible Block Copolymer Micellar Crystal," *Macromolecules*, vol. 40, no. 16, pp. 5801–5811, Aug. 2007.
- [8] S. Maier, M. Brongersma, and P. Kik, "Plasmonics—a route to nanoscale optical devices," *Adv. Mater.*, no. 19, pp. 1501–1505, 2001.
- [9] J. Matsui, K. Akamatsu, S. Nishiguchi, D. Miyoshi, H. Nawafune, K. Tamaki, and N. Sugimoto, "Composite of Au nanoparticles and molecularly imprinted polymer as a sensing material.," *Anal. Chem.*, vol. 76, no. 5, pp. 1310–5, Mar. 2004.
- [10] Z. Nie, A. Petukhova, and E. Kumacheva, "Properties and emerging applications of self-assembled structures made from inorganic nanoparticles.," *Nat. Nanotechnol.*, vol. 5, no. 1, pp. 15–25, Jan. 2010.

- [11] D. C. Pozzo and L. M. Walker, "Small-angle neutron scattering of silica nanoparticles templated in PEO-PPO-PEO cubic crystals," *Colloids Surfaces A Physicochem. Eng. Asp.*, vol. 294, no. 1–3, pp. 117–129, Feb. 2007.
- [12] V. Ortiz and S. Nielsen, "Computer simulation of aqueous block copolymer assemblies: length scales and methods," *J. Polym. Scienc Part B Polym. Phys.*, vol. 44, pp. 1907–1918, 2006.
- [13] J. a Anderson, C. D. Lorenz, and a Travasset, "Micellar crystals in solution from molecular dynamics simulations.," *J. Chem. Phys.*, vol. 128, no. 18, p. 184906, May 2008.
- [14] I. Rychkov and K. Yoshikawa, "Structural Changes in Block Copolymer Solutions under Shear Flow as Determined by Non-Equilibrium Molecular Dynamics," *Macromol. theory ...*, vol. 13, no. 3, pp. 257–264, 2004.
- [15] X. Zhang, S. Yuan, and J. Wu, "Mesoscopic Simulation on Phase Behavior of Ternary Copolymeric Solution in the Absence and Presence of Shear," *Macromolecules*, vol. 39, no. 19, pp. 6631–6642, Sep. 2006.
- [16] W. Loose and B. J. Ackerson, "Model calculations for the analysis of scattering data from layered structures," *J. Chem. Phys.*, vol. 101, no. 9, p. 7211, 1994.
- [17] S. J. Marrink, A. H. de Vries, and A. E. Mark, "Coarse Grained Model for Semiquantitative Lipid Simulations," *J. Phys. Chem. B*, vol. 108, no. 2, pp. 750–760, Jan. 2004.
- [18] S. J. Marrink, H. J. Risselada, S. Yefimov, D. P. Tieleman, and A. H. de Vries, "The MARTINI force field: coarse grained model for biomolecular simulations.," *J. Phys. Chem. B*, vol. 111, no. 27, pp. 7812–24, Jul. 2007.
- [19] K. Kremer, G. S. Grest, I. Festkörperforschung, F. Julich, W. Germanj, I. Physik, U. Mainz, D.- Mainz, and W. Germany, "Dynamics of entangled linear polymer melts : A molecular-dynamics simulation Dynamics of entangled linear polymer melts : A molecular-dynamics simulation," *Simulation*, vol. 5057, 1990.
- [20] H. C. Hamaker, "The London-van der Waals Attraction Between Spherical Particles," *Physica*, vol. IV, no. 10, 1937.
- [21] R. Everaers and M. Ejtehadi, "Interaction potentials for soft and hard ellipsoids," *Phys. Rev. E*, vol. 67, no. 4, Apr. 2003.

- [22] A. Khandpur, S. Foerster, and F. Bates, "Polyisoprene-polystyrene diblock copolymer phase diagram near the order-disorder transition," *Macromolecules*, pp. 8796–8806, 1995.
- [23] T. Soddemann, B. Dünweg, and K. Kremer, "Dissipative particle dynamics: A useful thermostat for equilibrium and nonequilibrium molecular dynamics simulations," *Phys. Rev. E*, vol. 68, no. 4, pp. 1–8, Oct. 2003.
- [24] S. Plimpton, "Fast Parallel Algorithms for Short – Range Molecular Dynamics," vol. 117, no. June 1994, pp. 1–42, 1995.
- [25] M. Holz, S. Heil, and A. Sacco, "Temperature-dependent self-diffusion coefficients of water and six selected molecular liquids for calibration in accurate 1H NMR PFG measurements," *Phys. Chem. Chem. Phys.*, pp. 1–3, 2000.
- [26] J. Kestin, M. Sokolov, and W. A. Wakeham, "Viscosity of Liquid Water in the Range -8C to 150C," *J. Phys. Chem. Ref. Data*, vol. 7, no. 3, pp. 941–948, 1978.
- [27] P. Steinhardt, D. Nelson, and M. Ronchetti, "Bond-orientational order in liquids and glasses," *Phys. Rev. B*, vol. 28, pp. 784–805, 1983.
- [28] T. Nicolai, O. Colombani, and C. Chassenieux, "Dynamic polymeric micelles versus frozen nanoparticles formed by block copolymers," *Soft Matter*, vol. 6, no. 14, p. 3111, 2010.
- [29] D. Marzi, C. N. Likos, and B. Capone, "Coarse graining of star-polymer--colloid nanocomposites.," *J. Chem. Phys.*, vol. 137, no. 1, p. 014902, Jul. 2012.
- [30] C. Misbah, "Vacillating Breathing and Tumbling of Vesicles under Shear Flow," *Phys. Rev. Lett.*, vol. 96, no. 2, p. 028104, Jan. 2006.
- [31] J. Deschamps, V. Kantsler, E. Segre, and V. Steinberg, "Dynamics of a vesicle in general flow.," *Proc. Natl. Acad. Sci. U. S. A.*, vol. 106, no. 28, pp. 11444–7, Jul. 2009.
- [32] D. R. Mikulencak and J. F. Morris, "Stationary shear flow around fixed and free bodies at finite Reynolds number," *J. Fluid Mech.*, vol. 520, pp. 215–242, Dec. 2004.
- [33] C. M. Zettner and M. Yoda, "Moderate-aspect-ratio elliptical cylinders in simple shear with inertia," *J. Fluid Mech.*, vol. 442, pp. 241–266, Aug. 2001.

- [34] M. Ripoll, R. Winkler, and G. Gompper, “Hydrodynamic screening of star polymers in shear flow,” *Eur. Phys. J. E*, vol. 23, no. 4, pp. 349–54, Aug. 2007.
- [35] A. Nikoubashman, G. Kahl, and C. N. Likos, “Flow quantization and nonequilibrium nucleation of soft crystals,” *Soft Matter*, vol. 8, no. 15, p. 4121, 2012.

CHAPTER 3

3. FLOW DISURBANCES AROUND SOFT PARTICLES

3.1 Introduction

Due to their broad spectrum of applications, dynamics of soft matter systems which consist of micelles, colloids, or both, have been the focus of decades of scientific inquiry. The bulk, or rheological properties of these systems have been the topic of entire fields of study, whereas the behavior of individual soft particles in flow has received relatively less attention. However, the understanding of the complex flow around individual particles in these systems is often a prerequisite to understanding the rheological behavior. Among these soft particles, vesicles are the subject of the greatest quantity of published work, owing to their biological importance and relatively larger size. This body of work has been supported experimentally [1], [2], theoretically [3]–[5], and computationally [6], [7]. Other soft particles in shear flow have been studied less extensively; these include: droplets, capsules, polymer-grafted nanoparticles (PGNs), star polymers, and branched polymers.

Deformable bodies exhibit a rich set of behaviors when subjected to shear flow including tank-treading, tumbling, trembling, stretching, collapse, and fission, and many of these can occur simultaneously [1], [8], [9]. For example, vesicles transition between tank-treading, tumbling, and trembling depending on shear rate, viscosity ratio, membrane elasticity, and size. Shape restoring forces with characteristic relaxation times play a determinant role in these dynamics[1]. Star-polymers are also

thought to exhibit similar dynamic regimes, with relaxation times of the complex polymer playing a key role [8], [9], although these systems are considerably less-well understood. Micelles occupy a region between these two soft matter extremes: they consist of a deformable hydrophobic core, like vesicles, and a hydrophilic corona of polymer “arms”, like a star-polymer.

Though much of the work done on other soft particle systems has only occurred in the last few decades, *dynamics* of individual polymeric micelles are still, in large part, missing from this knowledgebase. Several authors have used computational approaches to explore the behavior of concentrated micelle suspensions [10], [11], as well as extensive experimental studies [12]–[15], but to our knowledge, no one has yet thoroughly looked at the flow disturbance and dynamics of individual micelles in shear flow.

In this paper, we employ a computational model to simulate various individual particles, such as free colloids, colloids with tethered polymers, and polymeric micelles, subjected to shear fields. Understanding the complex behavior of individual micelles in response to flow is the first step in developing a complete model of how micelles behave in more concentrated systems. To this end, we first validate our coarse-grained molecular dynamics (CGMD) modeling by examining the dynamics of a spherical colloid particle under shear, followed by the study of those of a colloid with different lengths of tethered polymer chains on the surface under various flow strengths. Finally, we investigate the dynamics of a single micelle with various corona lengths under shear and compare them with those of colloids with tethered polymers. Leveraging this data could lead to new methods toward the prediction and control

macroscopic phenomena including shear-ordering/templating, shear-thinning, and other rheological properties.

3.2 Methods and Models

3.2.1 Coarse Grained Model

To probe the dynamic behavior of individual micelles, we build on our existing model for concentrated micelle suspensions[11]. As such, we employ a version of coarse-grained molecular dynamics (CGMD) that allows us to explore the length and time scales needed in non-equilibrium simulations. For the details of this model, we refer the reader to our previous paper and will only outline the most pertinent features and those unique to this work.

Our coarse-grained model has at its foundations the MARTINI force-field[16], where water molecules are joined into a group of 4, forming a single solvent particle of diameter $\sigma = 4.7 \text{ \AA}$ (σ being the distance parameter in the 12-6 Lennard-Jones (LJ) potential). Polymers are formed by joining CG particles with a finitely-extensible non-elastic (FENE) bond. Hydrophilic and hydrophobic interactions were obtained by tuning parameters of the LJ potentials [11]. A summary of parameters used in our model is included in Table 3-1, Table 3-2, and Table 3-3.

| MD Unit | Real Value | MD Unit | Definition | Real Value |
|------------|-------------|---------|---------------------------|----------------------------|
| σ | 4.7 Å | τ | $\sigma\sqrt{m/\epsilon}$ | 1.78 ps |
| ϵ | 5 kJ/mol | P^* | ϵ/σ^3 | 8.00 x 10 ⁷ MPa |
| m | 72.06 g/mol | T^* | ϵ/k_B | 600K |

Table 3-1 – MD Units

| Key | Explanation of interaction potentials |
|-----|---|
| I | 12-6 LJ: $\epsilon = 1.0, \sigma = 1.0, r_c = 2.5$ |
| II | 12-6 LJ: $\epsilon = 0.25, \sigma = 1.0, r_c = 2^{1/6}$ |
| * | Gromacs tail correction: $r = 1.915$ to 2.5 . |
| ^ | $\epsilon = 0.8$ |

Table 3-2 – Details of interaction parameters used in this paper.

| | W | A | B | C |
|---|----|----|-----|-----|
| W | I* | II | I* | II |
| A | | I* | II | N/A |
| B | | | II^ | II |
| C | | | | N/A |

Table 3-3 – Interaction matrix; W = Water/Solvent, A = A-type copolymer, B = B-type copolymer, and C = colloid.

We thermostat the system with dissipative particle dynamics (DPD), wherein the conservative forces have been replaced with the LJ forces previously discussed[11], [17]. DPD is chosen over other thermostats because it conserves linear momentum between particles and therefore captures hydrodynamic interactions. Our tests have shown that, given the damping parameters in our DPD implementation, shear rates above $\dot{\gamma} = 0.1\tau^{-1}$ result in an increase in temperature. However, the results presented here are restricted to shear rates one full order of magnitude below this limitation.

3.2.2 Simulation details

All simulations were performed using the open-source molecular dynamics package LAMMPS distributed by Sandia National Labs [18].

The simulation parameters discussed here are summarized in Table 3-4. A cubic box of side length 41.93σ with periodic boundaries (PB) on all faces was used for all results discussed here. This choice in box size is sufficient for finite size effects to be negligible for the size of the soft objects examined here. Indeed, we do not see noticeable changes in the flow behaviour as we increase the box size further. Shear was applied through a constant triclinic deformation in LAMMPS with particle velocities remapped when a shear-gradient boundary is crossed. This implementation is equivalent to the classic Lees-Edwards boundary conditions.

| Symbol | Definition | MD Value | MD Units | Real Value | Real Units |
|----------------|------------------------------|------------|--|---------------------------|----------------------------|
| L | Box Length | 41.925 | σ | 19.70 | nm |
| ρ^* | Number Density | 0.8685 | σ^{-3} | 1 | g/cm^3 |
| T^* | Temperature | 0.5 | ϵ/k_b | 300 | K |
| D^* | Measured Solvent Diffusivity | 0.0719 | σ^2/τ | 1.484×10^{-9} | m^2/s |
| η_0^* | Measured Solvent Viscosity | 5.99 | $\mathbf{P}^* \cdot \boldsymbol{\tau}$ | 8.5×10^{-4} | $\text{Pa} \cdot \text{s}$ |
| $\dot{\gamma}$ | Shear Rate | 0.001-0.01 | $\boldsymbol{\tau}^{-1}$ | $5.69 \times (10^8-10^9)$ | s^{-1} |

Table 3-4 – Simulation Parameters

The system number density was chosen such that the solvent density in real units is $1 \text{ g}/\text{cm}^3$ ($\rho^*\sigma^3 = 0.868$). This density is applied to the polymer-solvent matrix and is held constant. All simulations are relaxed from a random configuration using soft potentials. Further relaxation using full 12-6 Lennard-Jones potentials is applied before setting the individual interaction parameters. All relaxations are performed at $T^* = 1.0 k_B T$ (600K) and all main-run simulations are performed at $T^* = 0.5 k_B T$ (300K). The time step used for MD integration was 0.01τ (17.6 fs).

Construction simulations were necessary to control the exact characteristics of the soft objects. For the polymeric micelle simulations, we choose a representative

micelle from our previous work on concentrated suspensions. This micelle was self-assembled in those simulations, and comprises of 71 A6B12 diblock copolymers, for a total of 1278 particles. The micelle was then thoroughly relaxed in a solvent bath using the previously mentioned methods, with a total particle count of 64,000. To obtain the necessary corona lengths, ranging from B1 to B9, the hydrophilic polymers were “trimmed” by removing bonds and converting the freed polymer particles into solvent particles, whereby the system was then relaxed further. The micelles here comprise no more than 1.6% of the system, by weight.

Colloids were constructed to closely match the size and mass of the micelle core and are composed of 314, 1.0σ diameter surface particles and have an overall radius of 5σ . Surface particles have no intra-colloid interactions and form a rigid body -- that is, surface forces are converted into torques and translations about the center of mass. The colloid is made neutrally buoyant by ensuring the mass of the surface particles is such that the total mass of the colloid is equal to the mass of the displaced water particles, or

$$N_c m_c = \rho_w \left(\frac{4}{3}\right) \pi (R_c + r_c)^3$$

where the subscript c and w represent colloid and solvent CG particles, respectively, and R represents the colloid radius.

Colloids with coarse-grained polymers tethered to their surface provide a reasonable model of polymer-grafted nanoparticles (PGNs) or “hairy nanoparticles” as illustrated in the work of our colleagues Goyal and Escobedo[19]. PGNs use the aforementioned colloid as their core. A series of construction simulations were

employed to uniformly distribute B12 polymers on the surface, with a grafting density of 22% (71 polymers). These were then trimmed in an identical fashion to the micelles to obtain the desired corona length (B1-B9). Snapshots of each type of body discussed here are shown in Figure 3-1.

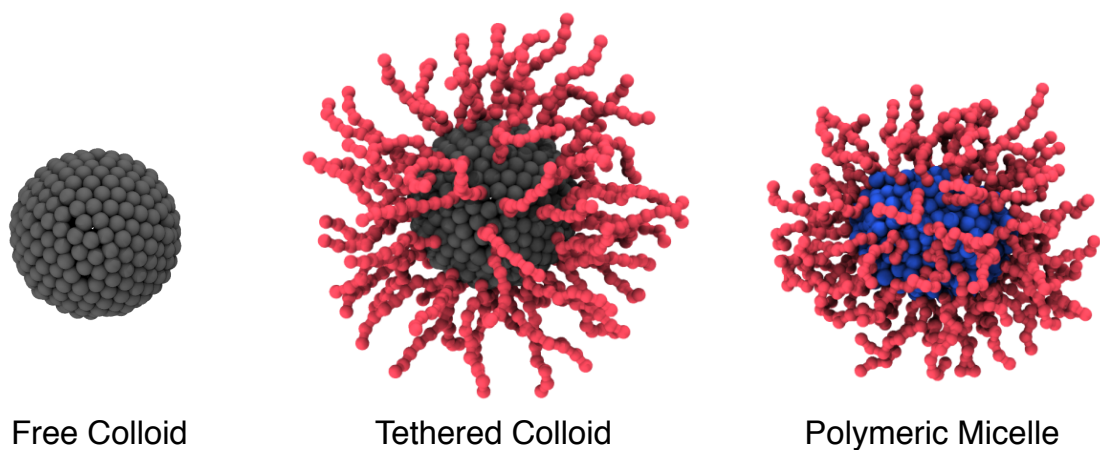


Figure 3-1– Examples of the three different types of objects studied in this paper.

Velocity fields are generated through the following procedure. First, raw simulation data are re-mapped such that the observer follows the center-of-mass of the soft body. Then, the system is discretized into bins, and velocities for every *solvent* particle in every bin are computed by tracking the displacement of the particle between two data time steps. Next, the procedure is repeated for every simulation data snapshot available, using the same bins, and the results are added to previous values. Finally, binned displacement data is normalized by the number of sample time steps and converted into a velocity by the difference in time between time steps. In other words, the velocity at any given bin is defined as

$$\mathbf{u}(i, j, k) = \frac{1}{M-1} \sum_{t=1}^{M-1} \sum_{N_{ijk}} (\mathbf{x}_{t+1} - \mathbf{x}_t) / (N_{ijk}) \quad \text{Equation 3-1}$$

where M is the number of sample time steps, N_{ijk} is the number of particles in bin position (i, j, k) , and \mathbf{x} is the position of a particle. We found that 40 box-lengths of accumulated strain, at a sampling interval of 50τ , was sufficient to obtain good data. For $\dot{\gamma} = 0.001\tau^{-1}$ that corresponds to 8,000,000 steps (800 samples) and for $\dot{\gamma} = 0.008\tau^{-1}$, 1,000,000 steps (100 samples).

Though it is well-established that spheres in shear flow may induce a velocity disturbance in the vorticity direction, and at finite Re numbers, this disturbance is more significant [20], the effect is small and our interest is primarily confined to the flow-gradient plane. To that end, we take a slice approximately 5.0σ in width, centered at the center-of-mass (COM) of the body in question, over which to average the velocity data. Or

$$\mathbf{u}(i, j) = \sum_{k=K}^{K+w} \frac{\mathbf{u}(i, j, k)}{w+1} \quad \text{Equation 3-2}$$

where K and $K+w$ form the bin-index bounds for the 5.0σ slice. The flow *disturbance* is found by subtracting the undisturbed flow field from the measured field, i.e. $\mathbf{u}' = (\mathbf{u} - \mathbf{u}^\infty)$. For simple shear, \mathbf{u}^∞ is simply $u_x = \dot{\gamma}y$, with the other components being zero. All velocity data are normalized by a characteristic velocity, $|u_c| = \dot{\gamma}a$, where a is the colloid diameter, and is equal to 10σ , regardless of the type of soft body considered.

3.3 Results and Discussion

We present our results in order of increasing object “softness”. We first validate our methods of measuring flow disturbances from shear fields by showing results of a spherical colloid in shear flow and comparing these to the known behavior of spheres in shear flow at low Re number. From here, we demonstrate how tethering polymers to the surface of this rigid colloid to produce a polymer-grafted nanoparticle (PGN) dramatically influences the observed flow behavior. Finally, we substitute the PGN with a self-assembled, deformable micelle of similar radius and repeat the analysis. Figure 3-9 shows an example of the flow characteristics for each type of object discussed in this section.

3.3.1 Colloid

The shear range used in this study ($0.001 - 0.01\tau^{-1}$) is within the low Reynolds number regime for a spherical colloid of diameter 10σ ($Re \approx 0.015 - 0.15$). We therefore use the Stokes-flow solutions and low but finite Re number numerical solutions as a benchmark for our results.

Figure 3-2 shows the velocity disturbance field generated by a single colloid in a shear field. These simulations were performed at a shear rate of $0.008\tau^{-1}$ ($Pe \approx 225, Re \approx 0.12$). Also shown in this figure are the Stokes solutions for a spherical particle (note that in the Stokes flow solution, the size of the particle does not affect the shape of the flow field). The stokes solutions take the form [20]

$$u_x = \frac{1}{2}y(1 - r^{-5}) + \frac{1}{2}y(1 - r^{-3}) - \frac{5}{2}x^2y(r^{-5} - r^{-7}) - \frac{\Omega y}{r^3} \quad \text{Equation 3-3}$$

$$u_y = \frac{1}{2}x(1 - r^{-5}) + \frac{1}{2}x(1 - r^{-3}) - \frac{5}{2}x^2y(r^{-5} - r^{-7}) - \frac{\Omega y}{r^3} \quad \text{Equation 3-4}$$

$$u_z = -\frac{5}{2}xyz(r^{-5} - r^{-7}) \quad \text{Equation 3-5}$$

where r is the distance from the sphere surface, and Ω is vorticity of the shear field, and is equal to $1/2$ in the scaling used here. Setting Ω to zero gives the fixed sphere solution. Both cases are considered: one where the colloid is held fixed, and is not free to translate or rotate, and the other where the colloid is not constrained in any way. Because the unconstrained colloid rotates in response to a torque, it is termed a torque-free object, whereas the fixed colloid acquires a torque (equal and opposite to the force required to prevent rotation).

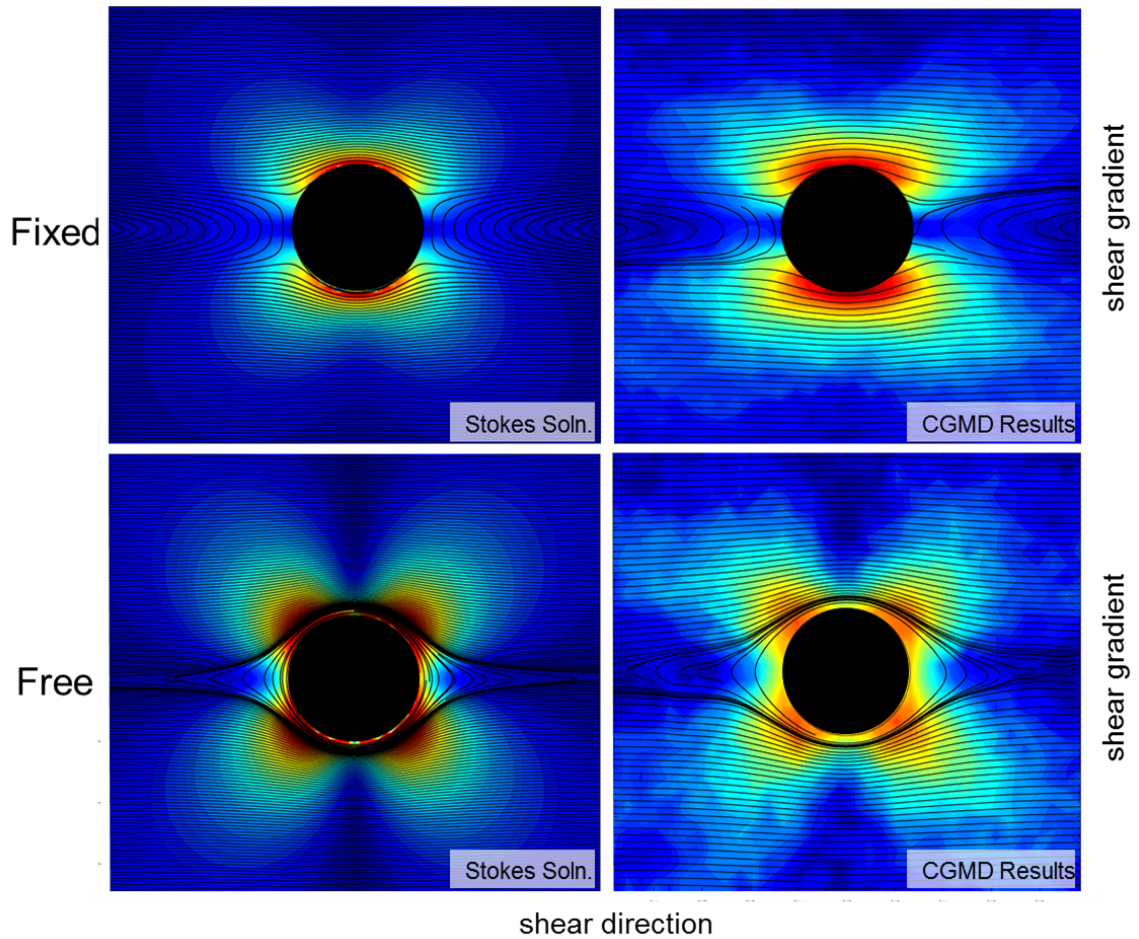


Figure 3-2 - Streamlines for velocity field and contour plots for velocity disturbance magnitude are shown for fixed and free colloids. The left pane shows the Stokes solutions for a sphere under these conditions, and the right pane shows the CGMD results obtained.

As Figure 3-2 clearly shows, our results agree quite well with the Stokes-flow solutions, with only slight differences in the streamlines. The torque-free sphere contrasts slightly in the positioning and extent of the closed streamlines as well as the region of flow reversal. Although it has been shown that small departures from $Re = 0$ can lead to a collapse in the limiting closed streamlines and distance to the

stagnation points[20], [21], we attribute these small deviations to the discrete nature of the coarse-grained solvent and the flow measurement, and perhaps the periodic boundaries, rather than the effects of finite Re number.

3.3.2 Polymer-grafted Nanoparticles

Polymers tethered to the surface of the colloid surface induce a markedly different response to the imposed shear as compared to the polymer-free colloid. The deformability of the soft corona results, on average, in a non-spherical conformation that becomes more pronounced at higher shear rates and with increasing the length of the tethered polymer chains. We first present the effect of the flow strength on the dynamics of polymer-grafted nanoparticles at a given tethered chain length. Figure 3-3 shows probability density profiles computed for the duration of the simulations for the two shear extremes. At low shear, the ellipsoid profile is nearly spherical with a major axis highly inclined to the flow direction. Conversely, at high shear the corona adopts an elongated ellipsoidal conformation with a much lower inclination angle.

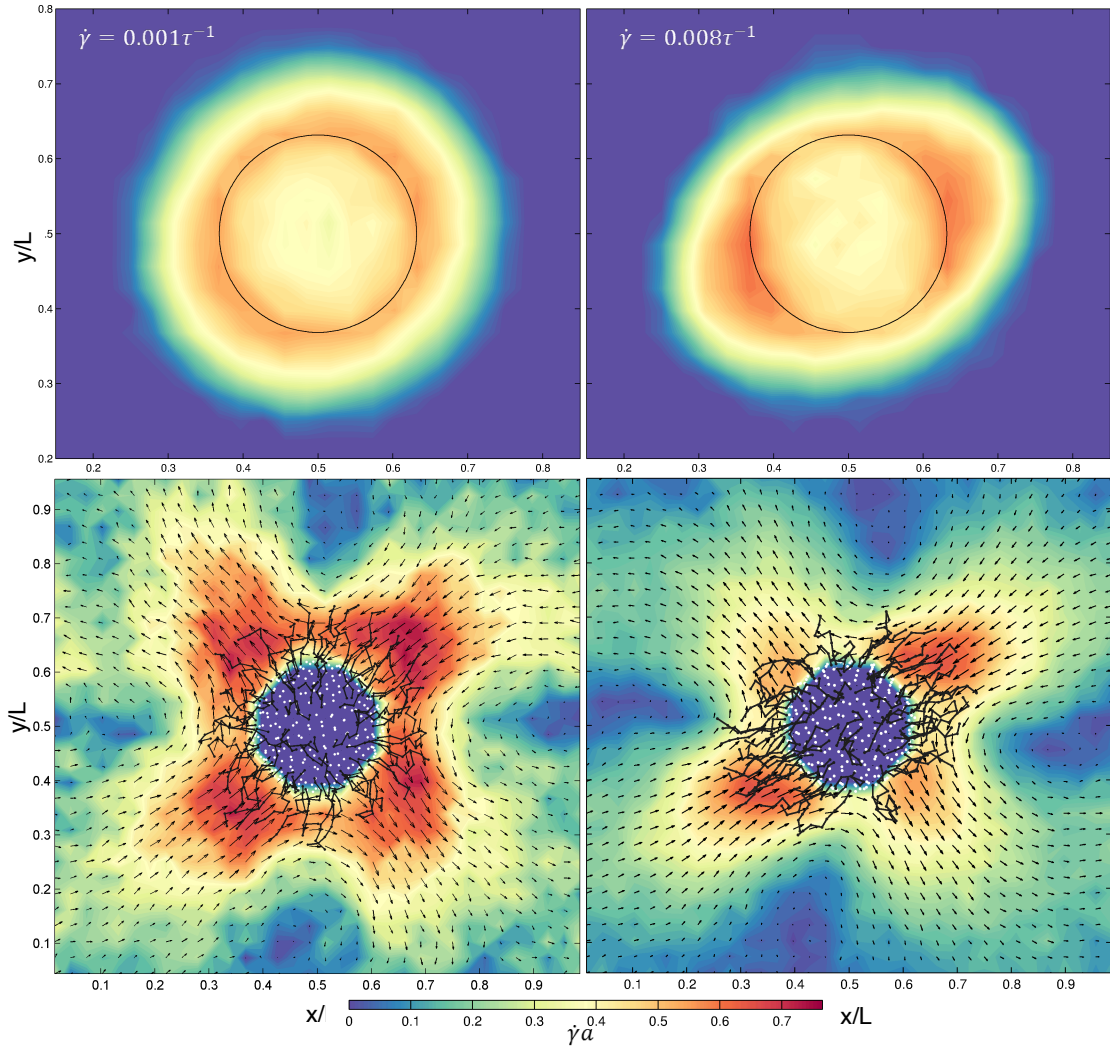


Figure 3-3 – Time-averaged polymer probability density plots (top) and time-averaged velocity disturbance fields (bottom) for the two shear extremes for B7 PGNs. Note that the density data are calculated the entire omitted vorticity axis whereas velocity field data are calculated within a vorticity-direction slice $\sim 6\sigma$ wide, centered at the center of mass. Snapshots of the PGNs are shown overlaid the disturbance fields.

The shift in inclination angle is an expected result. For vesicles and star polymers in the tank-treading regime, a decrease in inclination angle has been predicted, simulated, and observed throughout the literature [5], [6], [22]–[24]. For

tank-treading ellipsoids, it is generally accepted that the inclination angle decreases along with the sphericity index [5]. Simulation work on star polymers in shear has revealed similar behavior, where the normally spherical distribution of arms becomes ellipsoidal, tilted into the flow, and substantially reduced in the shear-gradient direction [9], [25]. A decrease in the inclination angle was also associated with these changes in the configurations of the arms.

A detailed view of the induced flow disturbance by the presence of a polymer-grafted nanoparticle is also shown in Figure 3-3 and those as a function of tethered length and shear rate, are collated into a matrix in Figure 3-4. There are two primary features that can be identified from all the disturbance fields: one rotational, one extensional, and both opposing the shear field. The source of these features arises as the colloid rotates in the flow. Individual tethered polymers are brought either into or out of the shear-gradient, or travel along the flow direction. Meanwhile, solvent in the swollen corona is advected during this rotation. Because the rotation rate of the colloid is necessarily slower than that of the rotational component of the applied shear field (Ω), the solvent rotating within the colloid's corona produces a disturbance that has a rotational component in the opposite direction (counter-clockwise). In a similar fashion, in the regions where polymers are brought into or out of the shear gradient (i.e. at $y = 0.5$, if $COM = (0.5, 0.5)$) solvent is advected perpendicularly away from the flow direction, leading to an extensional component opposite to that of the shear field. The combined result is primarily a quadrupole disturbance.

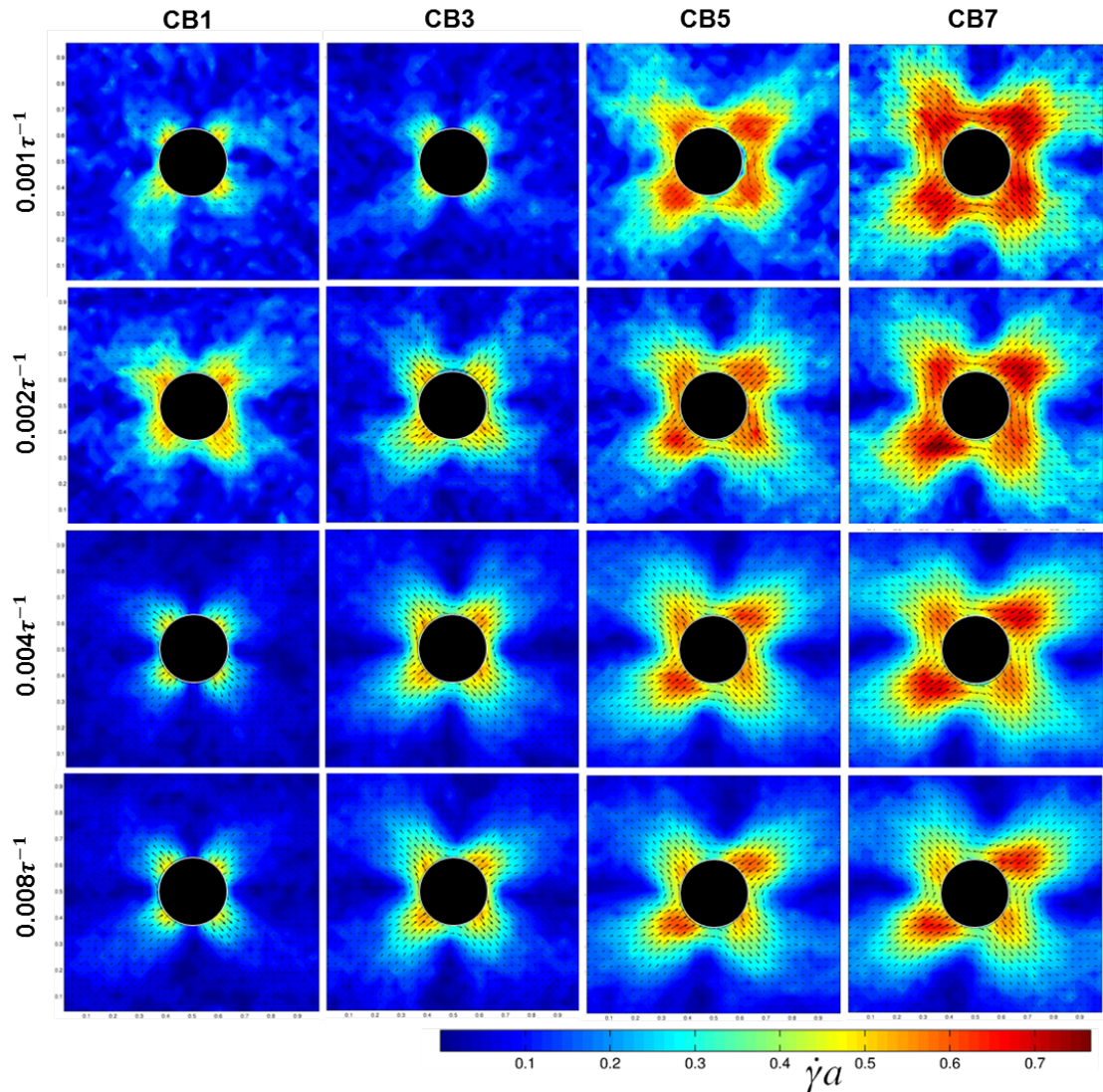


Figure 3-4 - Matrix showing the magnitude of the flow deviation as a function of both corona length and shear rate for the PGN. Contour plots represent the magnitude of the deviation from a linear field of the shear rate applied to the cell. Vector fields show the directionality of the deviation in the 2D cross-section.

Within the shear regime we explore, there is very little effect on the flow disturbance for short tethered polymers (< 3 bonded particles). This result is somewhat trivial, as solvent particles do not become trapped and advected by the corona. As the

tethered length increases, the shape of the flow disturbance becomes skewed into the flow direction. Simultaneously, the extent of disturbance grows proportionally to the contour length of the tethered polymers. Finally, there is change in the quadrupole symmetry, with the leading and trailing edges providing the strongest disruption to the linear shear profile.

Although the disruption to the symmetry that develops at long polymer/high shear is evident in Figure 3-4, the differences can be more precisely characterized by mapping the intensity of the disturbance as a function of an angle relative to the flow. Figure 3-5 shows this data for both the PGNs and micelles. Focusing on PGNs at low shear rates and short polymer lengths (top left), the intensity peaks are evenly spaced. As the shear rate and polymer length increase (bottom left), the spacing between peaks becomes uneven, corresponding to a decreased inclination angle of the colloid corona. This effect is most pronounced at the higher shear rates, where in Figure 3-5, the first and third peaks are seen to shift left, closer to the second and fourth peaks, respectively, whereas the second and fourth peaks remain at 45 degrees inclined (or declined) to the flow.

Figure 3-5 also shows more clearly the difference in magnitude of the flow disturbance around the colloid. This effect is again most evident at the higher shear rate, where we see a shift from peaks of equal magnitude at small tethered polymer length, to a clear increase of the disturbance along the inclination axis (i.e. the first and third peaks).

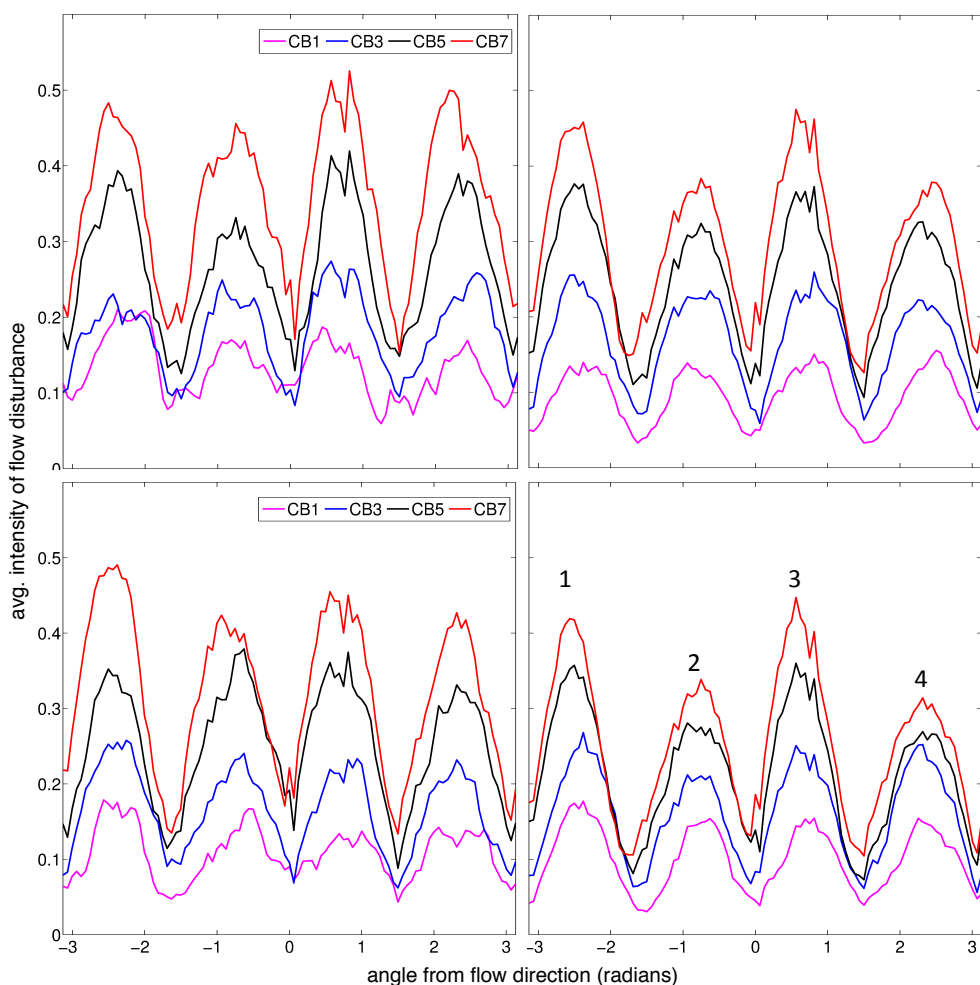


Figure 3-5 - Intensity data from flow disturbance magnitudes for PGNs (left) and polymeric micelles (right) as a function of angle from the flow. Here, an angle of 0 corresponds to the direction of the flow, and an angle of ± 180 degrees corresponds to the direction away from the flow.

3.3.3 Polymeric Micelles

Micelles are the “softest” particles presented here. Under shear, the micelles, on average, deform into an elongated ellipsoid inclined to the flow as seen in Figure 3-6. The minor axis of this ellipsoid is compressed, and inclination angle is decreased, as compared to the corresponding PGN. These differences are attributed to the

deformable micelle core and ability of the individual polymers to freely diffuse within the micelle.

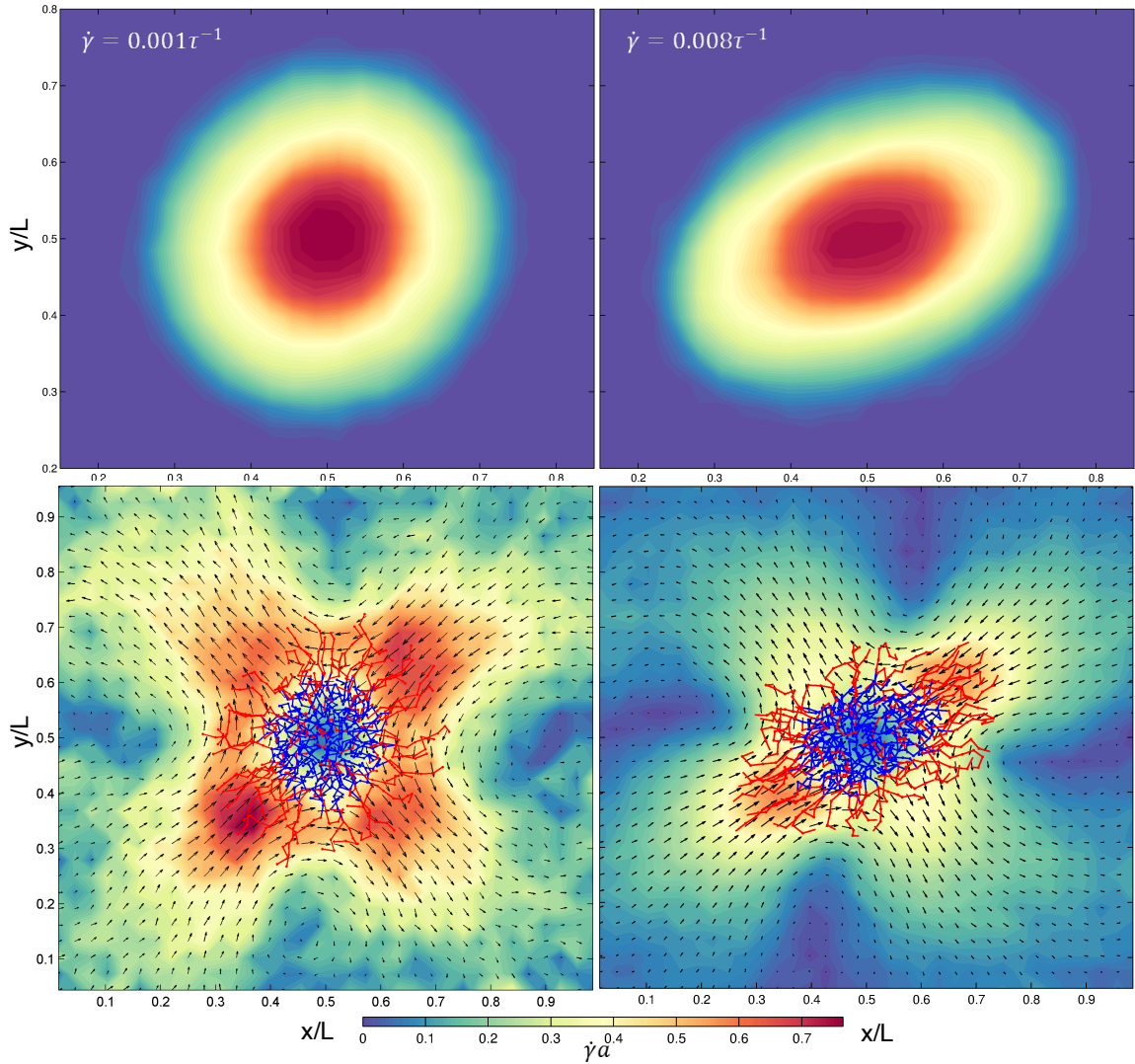


Figure 3-6 – Time-averaged polymer probability density plots (top) and time-averaged velocity disturbance fields (bottom) for the two shear extremes for A6B7 micelles. Note that the density data are calculated the entire omitted vorticity axis whereas velocity field data are calculated within a vorticity-direction slice $\sim 6\sigma$ wide, centered at the center of mass. Snapshots of the micelles are shown overlaid the disturbance fields.

As before, we have collated the disturbance field results for the micelles into a matrix as shown in Figure 3-7. The general trend of an increased extent of disturbance and the development of an asymmetry as we increase the corona length/shear strength is retained from the PGN results. These aspects are also shown more quantitatively with the intensity plots in Figure 3-5. To better understand the effects of shear and corona length on flow disturbance, we employ the dimensionless Weissenberg number $Wi = \dot{\gamma}\tau_R$, which relates the shear rate to the longest relaxation time τ_R of the micelle. Here, τ_R is taken from long-time exponential decay of the correlation function

$$C_{ee}(t) = \frac{\langle \mathbf{R}_{ee}(t)\mathbf{R}_{ee}(0) \rangle}{\langle \mathbf{R}_{ee}(0)\mathbf{R}_{ee}(0) \rangle} \quad \text{Equation 3-6}$$

where \mathbf{R}_{ee} is the end-to-end vector of an individual polymer and the average is taken over all polymers [9], [26]. These measurements were performed on zero-shear simulations for each micelle. We found that $\tau_R \propto L^{2.63}$, where L is the total contour length of the polymer. From this, values for Wi have been computed and overlaid atop the flow disturbance matrix in Figure 3-7. Unsurprisingly, the Weissenberg number follows the departure from a uniform quadrupole disturbance to a bimodal, skewed disturbance, and occurs only when $Wi > 20$.

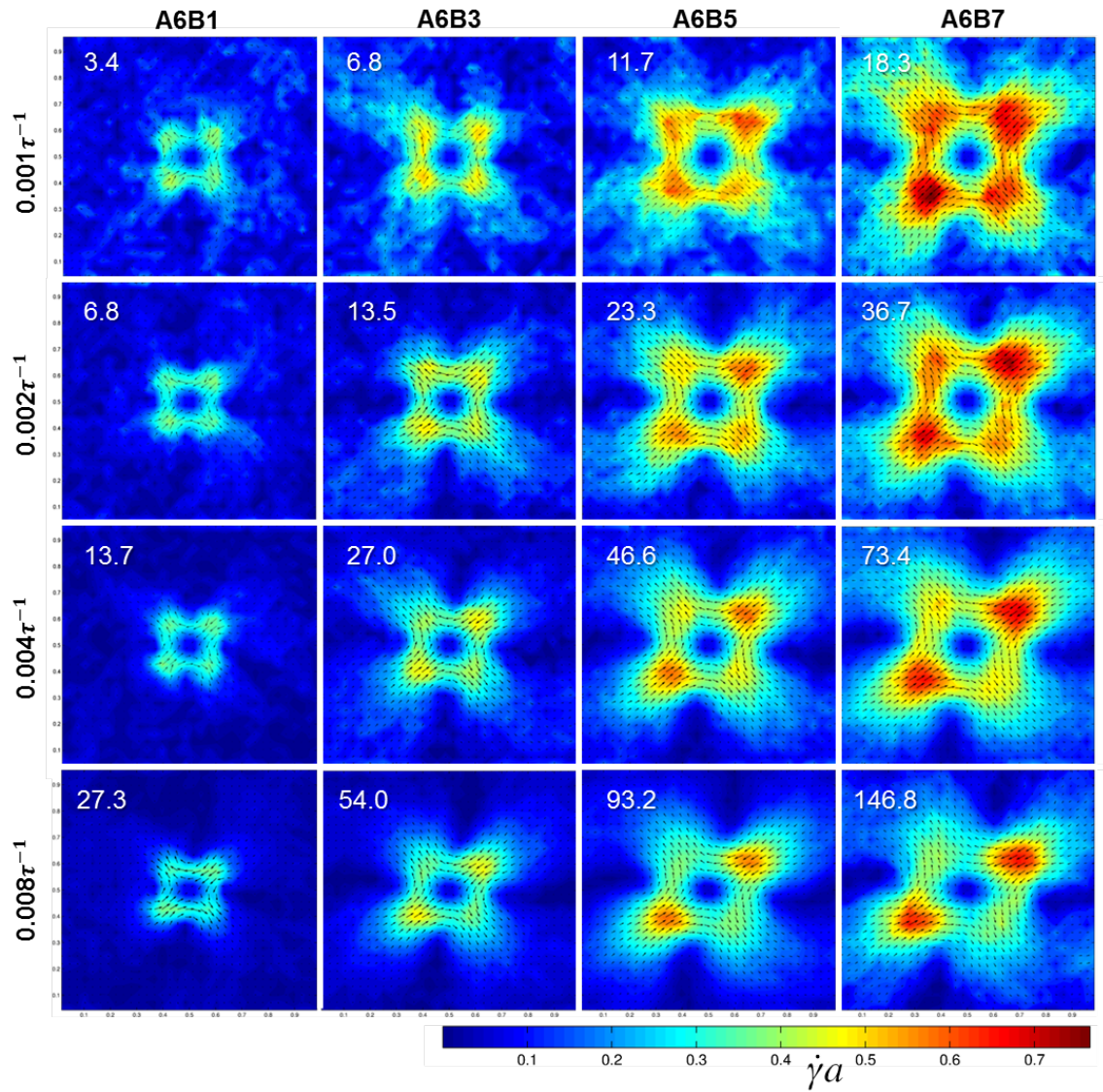


Figure 3-7 - Matrix showing the magnitude of the flow deviation as a function of both corona length and shear rate for a micelle. Contour plots represent the magnitude of the deviation from a linear field of the shear rate applied to the cell. Vector fields show the directionality of the deviation in the 2D cross-section. Overlaid numeric values correspond to the Wi number.

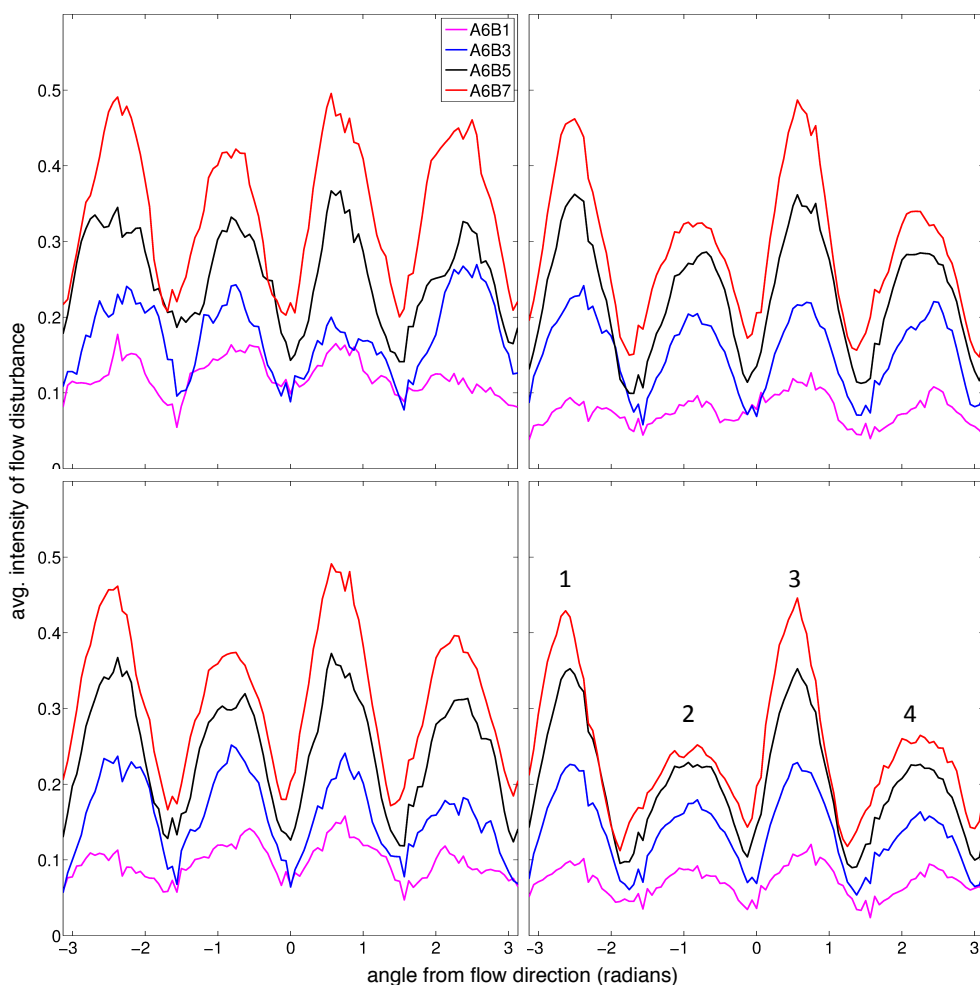


Figure 3-8 – Intensity data from flow disturbance magnitudes for PGNs (left) and polymeric micelles (right) as a function of angle from the flow. Here, an angle of 0 corresponds to the direction of the flow, and an angle of ± 180 degrees corresponds to the direction away from the flow.

There are important differences in the flow behavior between the two types of particles presented here. First, it should be noted that we observe a number of time-transient differences in the inclination angle, gyration tensor, relaxation processes, and shape parameters between the PGN and micelles, but due to their complexity and

focus of this work, those results will be presented in detail in a separate publication. For the micelles, the break in the quadrupole symmetry is even evident even for the shortest corona micelle, A6B1, at the highest shear rate of $0.008\tau^{-1}$ ($Wi = 27.3$). This result contrasts with the equivalent PGN, in which we see no measurable difference in the overall shape of the disturbance field (i.e. the quadrupole disturbance is retained). Though the corona is short to non-existent for the A6B1 micelles, the stretching and contracting of the soft core allow for significant interactions with the solvent particles near the surface. In contrast, the colloid is rigid and solvent-surface interactions are restricted to rotational motion. Similar observations hold for the A6B3 and CB3 systems. A summary of key differences is provided in Table 3-5.

| | Behavior | Flow disturbance | Observations |
|----------------|-----------------|--|--|
| Colloid | Rotational | Symmetric Quadrupole | Closely matches Stokes-Flow solutions |
| PGN | Rotational | Symmetric Quadrupole to Bimodal Skewed | Quadrupole retained for short corona. Pronounced disturbance/vorticity shedding. |
| Micelle | Tank-Treading | Symmetric Quadrupole to Bimodal Skewed | Break in quadrupole for short corona. Predominately bimodal disturbance at high Wi . |

Table 3-5 – Summary of important results

There are other more pronounced differences between PGNs and micelles and their effect on the surrounding flow. At the higher shear rates, the primary disruption to the shear field occurs in two places for both particles. These occur along the inclination axis. Though the PGNs share this region of peak disturbance, they also exhibit a strong flow disturbance along the colloid's surface leading into these peaks.

This ‘shedding’ behavior is best defined as occurring when the strongest disruption (along the inclination axis) is attached back to the surface of the colloid, and deformed outward into the flow direction. We see this shedding behavior more clearly in the flow *vorticity*, as highlighted in Figure 3-9. Furthermore, the non-quadrupole micelle disturbances are more strongly bimodal as compared to their PGN counterparts and are illustrated in Figure 3-9.

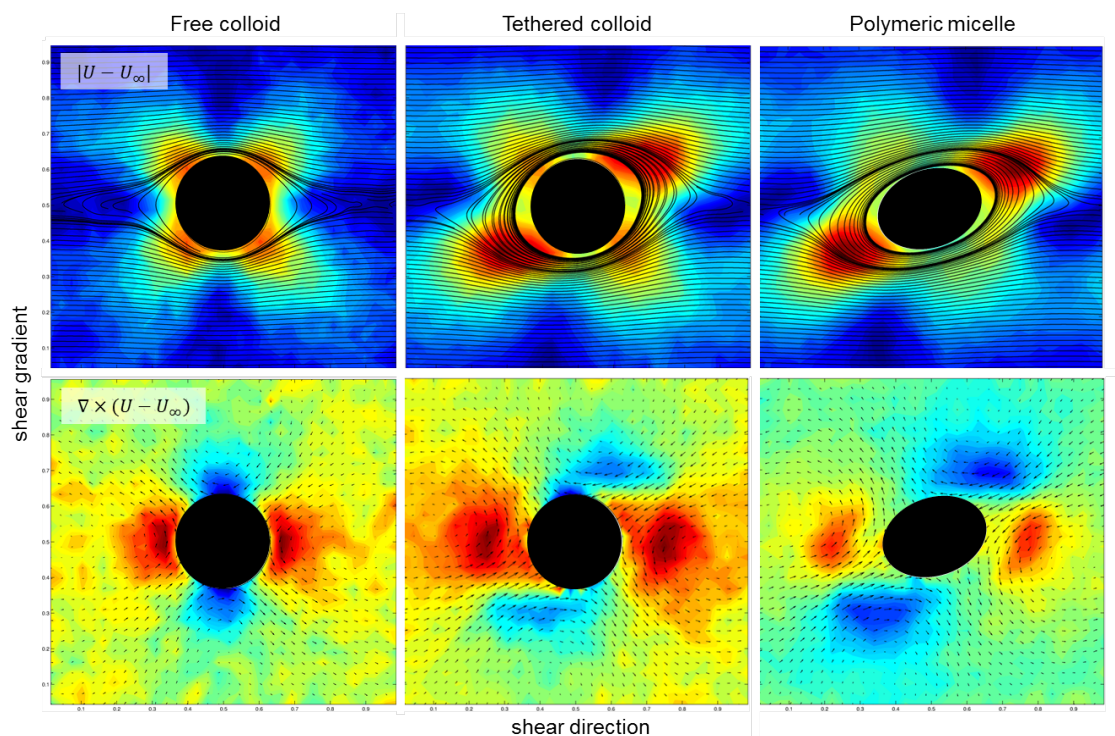


Figure 3-9 - A comparison of the flow characteristics of a free colloid, a PGN (CB9) and a micelle (A6B9), left to right, subjected to simple shear ($\dot{\gamma} = 0.008\tau^{-1}$). The top row shows the streamlines of the flow, with flow disturbance magnitudes as the contour background. The bottom row shows the deviation velocity field with the background contour field representing the relative magnitudes of the vorticity.

The differences observed in the surrounding flow between the PGN and micelle are consistent with what one would expect based on the constraints imposed upon the associated polymers. In both cases, the individual polymers respond to the shear field through stretching, rotation, and translation. In the micelle, solvent forces maintain the micelle core structure while allowing freedom for polymers to diffuse within this core. Additionally, the overall core shape responds to the shear field by stretching, rotating, and compressing, resulting in a trembling motion. On the other hand, the tethered polymers stretch and re-align, but their translational and rotational behavior are limited by the movement and rotation of the rigid colloid. The shedding behavior seen in the PGNs is then explained as a result of the difference in timescales between the slower rotating colloid and the faster individual polymers realigning to the flow.

Traversing Figure 3-9 from left to right best summarizes the important results between the different bodies. Without a soft, deformable component, the free colloid rotates in the flow, disturbing the linear shear field, and creates a region of closed streamlines consistent with low Re solutions. As flexible, hydrophilic polymers are tethered to the surface of this colloid, the extent of the disturbance expands, and the deformability and time-scales associated with the polymers result in skewed disturbances and inclination of the rotational flow. When the rigid body of the colloid is replaced with the soft deformable core of a micelle, disturbance flow becomes further exaggerated with an associated decrease in inclination angle owing to the overall deformability.

3.4 Conclusions

We have shown in this work that polymer-grafted nanoparticles and polymeric micelles induce flow disturbances similar to those of other soft bodies in response to simple shear flow. The extent of these disturbances are proportional to the contour length of the corona, and the strongest deviations occur along the inclination axis – which itself decreases between the two particles and with increasing shear. There are differences in the exact shape of the quadrupole and bimodal disturbance fields that we attribute to the deformability of the core portion of the soft body. For the polymeric micelles, the quadrupole to bimodal transition is well predicted by the Weissenberg number, and occurs for values greater than 20. These results may have important implications for applications where high shear rates are present, such as electro and centrifugal spinning processes. Further studies to characterize dynamic behavior of individual micelles and their impact in multi/concentrated micelle systems are currently underway.

Acknowledgements

We would like to thank the National Science Foundation for funding through the National Science Foundation Graduate Research Fellowship Program (NSFGRFP) under Grant No. DGE-1144153. This work was also supported by the computational facilities (Darter and Kraken) provided by the National Institute of Computational Sciences (NICS) and made available through the NSFGRFP.

REFERENCES

- [1] J. Deschamps, V. Kantsler, E. Segre, and V. Steinberg, “Dynamics of a vesicle in general flow.,” *Proc. Natl. Acad. Sci. U. S. A.*, vol. 106, no. 28, pp. 11444–7, Jul. 2009.
- [2] T. Fischer, M. Stohr-Lissen, and H. Schmid-Schonbein, “The red cell as a fluid droplet: tank tread-like motion of the human erythrocyte membrane in shear flow,” *Science (80-.)*, vol. 202, no. 4370, pp. 894–896, Nov. 1978.
- [3] M. Kraus, W. Wintz, U. Seifert, and R. Lipowsky, “Fluid Vesicles in Shear Flow.,” *Phys. Rev. Lett.*, vol. 77, no. 17, pp. 3685–3688, Oct. 1996.
- [4] F. Rioual, T. Biben, and C. Misbah, “Analytical analysis of a vesicle tumbling under a shear flow,” *Phys. Rev. E*, vol. 69, no. 6, p. 061914, Jun. 2004.
- [5] S. Keller and R. Skalak, “Motion of a tank-treading ellipsoidal particle in a shear flow,” *J. Fluid Mech.*, vol. 120, no. -1, p. 27, Apr. 1982.
- [6] H. Zhao and E. S. G. Shaqfeh, “The dynamics of a vesicle in simple shear flow,” *J. Fluid Mech.*, vol. 674, pp. 578–604, Mar. 2011.
- [7] H. Noguchi and G. Gompper, “Fluid vesicles with viscous membranes in shear flow,” *Phys. Rev. Lett.*, pp. 0–3, 2004.
- [8] M. Ripoll, R. Winkler, and G. Gompper, “Star Polymers in Shear Flow,” *Phys. Rev. Lett.*, vol. 96, no. 18, p. 188302, May 2006.
- [9] S. P. Singh, A. Chatterji, G. Gompper, and R. G. Winkler, “Dynamical and Rheological Properties of Ultrasoft Colloids under Shear Flow,” *Macromolecules*, vol. 46, no. 19, pp. 8026–8036, Oct. 2013.
- [10] J. Castillo-Tejas, J. F. J. Alvarado, S. Carro, F. Pérez-Villaseñor, F. Bautista, and O. Manero, “Rheology of wormlike micelles from non-equilibrium molecular dynamics,” *J. Nonnewton. Fluid Mech.*, vol. 166, no. 3–4, pp. 194–207, Feb. 2011.
- [11] B. a. Rolfe, J. Chun, and Y. L. Joo, “Dynamics of micelle–nanoparticle systems undergoing shear: a coarse-grained molecular dynamics approach,” *Soft Matter*, vol. 9, no. 43, p. 10294, 2013.
- [12] G. Arya, J. Rottler, A. Z. Panagiotopoulos, D. J. Srolovitz, and P. M. Chaikin, “Shear ordering in thin films of spherical block copolymer.,” *Langmuir*, vol. 21, no. 24, pp. 11518–27, Nov. 2005.

- [13] G. E. Newby, I. W. Hamley, S. M. King, C. M. Martin, and N. J. Terrill, "Structure, rheology and shear alignment of Pluronic block copolymer mixtures.," *J. Colloid Interface Sci.*, vol. 329, no. 1, pp. 54–61, Jan. 2009.
- [14] H. Watanabe, "Feature Article Rheology of diblock copolymer micellar systems," 1997.
- [15] P. Alexandridis, "Poly(ethylene oxide)/poly(propylene oxide) block copolymer surfactants," *Curr. Opin. Colloid Interface Sci.*, vol. 2, no. 5, pp. 478–489, Oct. 1997.
- [16] S. J. Marrink, H. J. Risselada, S. Yefimov, D. P. Tieleman, and A. H. de Vries, "The MARTINI force field: coarse grained model for biomolecular simulations.," *J. Phys. Chem. B*, vol. 111, no. 27, pp. 7812–24, Jul. 2007.
- [17] P. Español, "Dissipative particle dynamics with energy conservation," *EPL (Europhysics Letters)*, vol. 40, no. 6, p. 631, 1997.
- [18] S. Plimpton, "Fast Parallel Algorithms for Short – Range Molecular Dynamics," vol. 117, no. June 1994, pp. 1–42, 1995.
- [19] S. Goyal and F. a Escobedo, "Structure and transport properties of polymer grafted nanoparticles.," *J. Chem. Phys.*, vol. 135, no. 18, p. 184902, Nov. 2011.
- [20] D. R. Mikulencak and J. F. Morris, "Stationary shear flow around fixed and free bodies at finite Reynolds number," *J. Fluid Mech.*, vol. 520, pp. 215–242, Dec. 2004.
- [21] G. G. Poe and A. Acrivos, "Closed-streamline flows past rotating single cylinders and spheres: inertia effects," *J. Fluid Mech.*, vol. 72, no. 04, p. 605, Mar. 1975.
- [22] V. Kantsler and V. Steinberg, "Orientation and Dynamics of a Vesicle in Tank-Treading Motion in Shear Flow," *Phys. Rev. Lett.*, vol. 95, no. 25, p. 258101, Dec. 2005.
- [23] Y. Sui, H. T. Low, Y. T. Chew, and P. Roy, "Tank-treading, swinging, and tumbling of liquid-filled elastic capsules in shear flow," *Phys. Rev. E*, vol. 77, no. 1, p. 016310, Jan. 2008.
- [24] M. Ripoll, R. Winkler, and G. Gompper, "Hydrodynamic screening of star polymers in shear flow," *Eur. Phys. J. E*, vol. 23, no. 4, pp. 349–54, Aug. 2007.

- [25] G. Gompper, T. Ihle, D. M. Kroll, and R. G. Winkler, “Particle-Based Mesoscale Simulation Approach to the Hydrodynamics of Complex Fluids,” *Soft Condens. Matter*, 2008.
- [26] G. S. Grest, K. Kremer, S. T. Milnerpt, and T. A. Wittent, “Self-Entangled Many-Arm Star Polymers,” pp. 1904–1910, 1989.

CHAPTER 4

4. DYNAMICS OF SOFT PARTICLES IN SHEAR FLOW

4.1 Introduction

Among soft particles, vesicles are the subject of the greatest quantity of published work, owing to their biological importance and relatively larger size. This body of work has been supported experimentally [1], [2], theoretically [3]–[5], and computationally [6], [7]. Other soft particles in shear flow have been studied less extensively; these include: polymer-grafted nanoparticles (PGNs)[8], star polymers [9], branched polymers[10], among others.

Deformable bodies exhibit a rich set of behaviors when subjected to shear flow including tank-treading, tumbling, trembling, stretching, collapse, and fission, and many of these can occur simultaneously [1], [9], [11]. For example, vesicles transition between tank-treading, tumbling, and trembling depending on shear rate, viscosity ratio, membrane elasticity, and size. Shape restoring forces with characteristic relaxation times play a determinant role in these dynamics [1]. Star-polymers are also thought to exhibit similar dynamic regimes, with relaxation times of the complex polymer playing a key role [9], [11], although these systems are considerably less-well understood. Micelles occupy a region between these two soft matter extremes: they consist of a deformable hydrophobic core, like vesicles, and a hydrophilic corona of polymer “arms”, like a star-polymer. Meanwhile, PGNs lie somewhere between a fully soft micelle, and a completely rigid particle, depending on the tethered polymer length.

Though much of the work done on other soft particle systems has only occurred in the last few decades, *dynamics* of individual polymeric micelles are still, in large part, missing from this knowledgebase. Several authors have used computational approaches to explore the behavior of concentrated micelle suspensions [12], [13], as well as extensive experimental work in the field of rheology [14]–[17]. To our knowledge, however, there are no comprehensive studies on the steady-state dynamics of individual micelles and PGNs in shear flow.

In this paper, we analyze the dynamical behavior of soft PGNs and micelles in equilibrium and under applied shear using coarse-grained molecular dynamics (CGMD). The inclusion of PGNs in the analysis is two fold: one is fundamental, in that their individual flow behavior has not been the scrutiny of any scientific studies; one is practical, in that their “softness” is adjustable through changing the length of tethered polymers, and therefore provide a means to isolate physical mechanisms at play. Given the importance of relaxation phenomena in governing dynamics of ultrasoft particles [10], [11], [18]–[20], we first perform a detailed study of the dominant relaxation modes of both types of particles. In other soft particles, these modes range from fast elastic relaxations of individual polymers to very slow conformational relaxations governed by diffusive regimes. Since micelles and PGNs are similar in many fundamental aspects to star polymers and vesicles, similar relaxation modes and time scales are expected to be present. Proper treatment of relaxation time scales allows for a meaningful analysis of dynamics. To that end, we measure the primary steady-state dynamics that are present in other soft matter

systems including shear-alignment, rotation and tank-treading, and shear-induced deformation.

The remainder of this paper is organized as follows: we first provide an overview of our computational model. We then proceed by introducing the methods of our analysis on relaxation and dynamic characterization. Results are then presented, in order, for relaxation phenomena, shape deformation, shear-alignment, and finally rotational motion. In our conclusions, we summarize our important findings and provide direction for future work.

4.2 Methods and Models

4.2.1 Coarse Grained Model

To probe the dynamic behavior of individual micelles and PGNs, we build on our existing model for concentrated micelle suspensions[13]. As such, we employ a version of coarse-grained molecular dynamics (CGMD) that allows us to explore the length and time scales needed in non-equilibrium simulations. For the details of this model, we refer the reader to our previous paper and will only outline the most pertinent features and those unique to this work.

Our coarse-grained model has at its foundations the MARTINI force-field[21], where water molecules are joined into a group of 4, forming a single solvent particle of diameter $\sigma = 4.7 \text{ \AA}$ (σ being the distance parameter in the 12-6 Lennard-Jones (LJ) potential). Polymers are formed by joining CG particles with a finitely-extensible non-elastic (FENE) bond. Hydrophilic and hydrophobic interactions were obtained by tuning parameters of the LJ potentials [13]. A summary of parameters used in our model is included in Table 4-1, Table 4-2, and Table 4-3.

| MD Unit | Real Value | MD Unit | Definition | Real Value |
|------------|-------------|---------|---------------------------|----------------------------|
| σ | 4.7 Å | τ | $\sigma\sqrt{m/\epsilon}$ | 1.78 ps |
| ϵ | 5 kJ/mol | P^* | ϵ/σ^3 | 8.00 x 10 ⁷ MPa |
| m | 72.06 g/mol | T^* | ϵ/k_B | 600K |

Table 4-1 – MD Unit definitions

| Key | Explanation of interaction potentials |
|-----|---|
| I | 12-6 LJ: $\epsilon = 1.0$, $\sigma = 1.0$, $r_c = 2.5$ |
| II | 12-6 LJ: $\epsilon = 0.25$, $\sigma = 1.0$, $r_c = 2^{1/6}$ |
| * | Gromacs tail correction: $r = 1.915$ to 2.5. |
| ^ | $\epsilon = 0.8$ |

Table 4-2 – Interaction parameters used in these simulations

| | W | A | B | C |
|---|----|----|-----|-----|
| W | I* | II | I* | II |
| A | | I* | II | N/A |
| B | | | II^ | II |
| C | | | | N/A |

Table 4-3 – Interaction matrix; W = Water/Solvent, A = A-type copolymer, B = B-type copolymer, and C = colloid.

We thermostat the system with dissipative particle dynamics (DPD), wherein the conservative forces have been replaced with the LJ forces previously discussed[13], [22]. DPD is chosen over other thermostats because it conserves linear momentum between particles and therefore captures hydrodynamic interactions. Our tests have shown that, given the damping parameters in our DPD implementation, shear rates above $\dot{\gamma} = 0.1\tau^{-1}$ result in an increase in temperature. However, the results

presented here are restricted to shear rates one full order of magnitude below this limitation.

4.2.2 Simulation details

All simulations were performed using the open-source molecular dynamics package LAMMPS distributed by Sandia National Labs [23].

The simulation parameters discussed here are summarized in Table 4-4. A cubic box of side length 41.93σ with periodic boundaries (PB) on all faces was used for all results discussed here. This choice in box size is sufficient for finite size effects to be negligible for the size of the soft objects examined here. Indeed, we do not see noticeable changes in the flow behaviour as we increase the box size further. Shear was applied through a constant triclinic deformation in LAMMPS with particle velocities remapped when a shear-gradient boundary is crossed. This implementation is equivalent to the classic Lees-Edwards boundary conditions.

| Symbol | Definition | MD Value | MD Units | Real Value | Real Units |
|----------------|------------------------------|------------|------------------|---|-------------------|
| L | Box Length | 41.925 | σ | 19.70 | nm |
| ρ^* | Number Density | 0.8685 | σ^{-3} | 1 | g/cm ³ |
| T^* | Temperature | 0.5 | ϵ/k_b | 300 | K |
| D^* | Measured Solvent Diffusivity | 0.0719 | σ^2/τ | 1.484×10^{-9} | m ² /s |
| η_0^* | Measured Solvent Viscosity | 5.99 | $P^* \cdot \tau$ | 8.5×10^{-4} | Pa · s |
| $\dot{\gamma}$ | Shear Rate | 0.001-0.03 | τ^{-1} | $5.69 \times 10^8 - 1.7 \times 10^{10}$ | s ⁻¹ |

Table 4-4 – Summary of simulation parameters

The system number density was chosen such that the solvent density in real units is 1 g/cm³ ($\rho^* \sigma^3 = 0.868$). This density is applied to the polymer-solvent matrix and is held constant. All simulations are relaxed from a random configuration using soft potentials. Further relaxation using full 12-6 Lennard-Jones potentials is applied before setting the individual interaction parameters. All relaxations are

performed at $T^* = 1.0 k_B T$ (600K) and all main-run simulations are performed at $T^* = 0.5 k_B T$ (300K). The time step used for MD integration was 0.01τ (17.6 fs).

Construction simulations were necessary to control the exact characteristics of the soft objects. For the polymeric micelle simulations, we choose a representative micelle from our previous work on concentrated suspensions. This micelle was self-assembled in those simulations, and comprises of 71 A6B12 diblock copolymers, for a total of 1278 particles. The micelle was then thoroughly relaxed in a solvent bath using the previously mentioned methods, with a total particle count of 64,000. To obtain the necessary corona lengths, ranging from B1 to B9, the hydrophilic polymers were “trimmed” by removing bonds and converting the freed polymer particles into solvent particles, whereby the system was then relaxed further. The micelles here comprise no more than 1.6% of the system, by weight.

Colloids were constructed to closely match the size and mass of the micelle core and are composed of 314, 1.0σ diameter surface particles and have an overall radius of 5σ . Surface particles have no intra-colloid interactions and form a rigid body -- that is, surface forces are converted into torques and translations about the center of mass. The colloid is made neutrally buoyant by ensuring the mass of the surface particles is such that the total mass of the colloid is equal to the mass of the displaced water particles, or

$$N_c m_c = \rho_w \left(\frac{4}{3}\right) \pi (R_c + r_c) \quad \text{Equation 4-1}$$

where the subscript c and w represent colloid and solvent CG particles, respectively, and R represents the colloid radius.

Colloids with coarse-grained polymers tethered to their surface provide a reasonable model of polymer-grafted nanoparticles, as illustrated in the work of our colleagues Goyal and Escobedo [8]. PGNs employ the aforementioned colloid as their core. A series of construction simulations were carried out to uniformly distribute B12 polymers on the surface, with a grafting density of 22% (71 polymers). These were then trimmed in an identical fashion to the micelles to obtain the desired corona length (B1-B9). Snapshots of each type of body discussed here are shown in Figure 4-1.

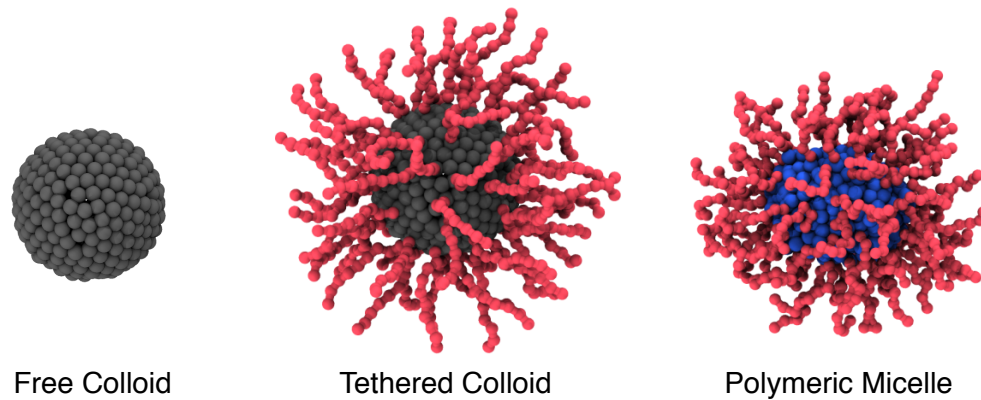


Figure 4-1– Examples of the three different types of objects studied in this paper.

4.2.3 Methods of analysis

To calculate rotational diffusivity for the PGNs, we track the surface-to-center vectors (\vec{r}_{SC}) for rigid body rotational motion. The periodic nature of the cosine

function precludes direct computation of the angular displacement at any given time step, so we define the net angular displacement using [8]

$$\vec{\phi}(t) = \int_0^t \delta\vec{\phi} dt \quad \text{Equation 4-2}$$

From these data, we then calculate the rotational diffusion via mean-squared displacement relation

$$D_R = \lim_{\Delta t \rightarrow \infty} \frac{1}{4\Delta t} \langle \phi^2(\Delta t) \rangle \quad \text{Equation 4-3}$$

We may also compare these calculated values with the Stokes-Einstein relation for an ideal sphere

$$D_{R,ideal} = \frac{k_B T}{8\pi\eta R^3} \quad \text{Equation 4-4}$$

where η is the fluid viscosity and R is the radius of the particle. The nanoparticles which serve as the core of the PGNs presented here have an ideal rotational diffusivity of $D_{R,ideal} = 2.65 \times 10^{-5} \tau^{-1}$ computed from the measured solvent viscosity $\eta = 5.99P^*\tau$ and nanoparticle radius $R = 5\sigma$.

Equation 4-2 is also employed to quantify rotational motion of both micelles and PGNs in the sheared state. End-to-center vectors \vec{r}_{EC} are used instead of surface-to-center vectors for consistency between the measurements. In the case of an untethered nanoparticle, these are identical quantities. Rotational motion $\omega = d\phi/dt$ is only presented for motions about the vorticity axis, or $\omega = \omega_y = d\phi_y/dt$.

Many non-equilibrium characteristics of the soft particles can be characterized by the gyration tensor

$$G_{\alpha\beta} = \frac{1}{N} \sum_{i=1}^N (r_{i,\alpha} - r_{CM,\alpha})(r_{i,\alpha} - r_{CM,\beta}) \quad \text{Equation 4-5}$$

where the subscript *CM* indicates center of mass over the sum of *N* particles constituting the soft particle. For the PGNs, this sum is computed over the tethered polymers, which includes the surface bond points. Non-bonded surface particles are not considered. Unless otherwise noted, all references to a gyration tensor refer to the *average* gyration tensor, which is averaged over the length of the simulations.

Under shear flow, the eigenvalues of the gyration tensor can be used to define an asphericity parameter

$$\delta = \frac{G_1}{G_3} - 1 \quad \text{Equation 4-6}$$

where G_1 and G_3 refer to the largest and smallest eigenvalues, respectively. When the particle is spherical, G_1 and G_2 are equal and the asphericity is zero and the quantity diverges for a rod of infinite aspect ratio.

Finally, the gyration tensor can be used to compute an inclination angle χ or, alternatively, an orientational resistance parameter m_g with the expression

$$m_g = \tan(2\chi) = \frac{2\langle G_{xz} \rangle}{\langle G_{xx} \rangle + \langle G_{zz} \rangle} \quad \text{Equation 4-7}$$

where G_{xx} and G_{zz} are the tensor components in the flow and gradient directions, respectively. It is important to recognize that this quantity diverges for spherical, or near spherical particles. We therefore do not present data for low shear, short corona length particles that are not deformed significantly by the flow.

To better understand the dynamics in these systems, we measured the characteristic relaxation time scales. These time scales serve to rescale shear rates into the dimensionless Weissenberg values, $Wi = \tau_R \dot{\gamma}$. Relaxations involving polymer end-to-end, end-to-center, or end-to-surface vectors are determined through a fit of an exponential decay of their time-autocorrelation functions

$$C_R(t) = \frac{\langle \mathbf{R}(t)\mathbf{R}(0) \rangle - \langle R \rangle^2}{\langle R^2 \rangle - \langle R \rangle^2} \quad \text{Equation 4-8}$$

and the fit has the general form

$$C_R(t) = a \cdot e^{-t/\tau_R} \quad \text{Equation 4-9}$$

where \mathbf{R} is the vector quantity being correlated and τ_R is the relaxation time for this quantity. The vector components may also be separated into separate correlations for each primary direction, and the analysis is identical. Longer relaxation time scales can also be approximated through the measured diffusion coefficients

$$\tau_{RR} \sim \frac{1}{D_R} \quad \text{Equation 4-10}$$

4.3 Results and Discussion

We first discuss the dominant relaxation time scales and how these are affected by corona and tethered polymer lengths. With this context, we then show results for micelle and PGN deformations both qualitatively and quantitatively as a function of shear and Wi and compare these results against similar particles in the literature. Finally, we conclude with an analysis on the tank-treading and rotational motion of the two soft particles.

4.3.1 Relaxation Phenomena

The micelles and PGNs studied here are similar in that they share a flexible, hydrophilic corona, are of similar size, and have an equivalent number of polymer “arms”. They differ, critically, in that the PGNs are constructed around a rigid nanoparticle whereas the micelle particle is self-assembled with a “soft” core, held together by energetically favorable conditions. For dilute polymer solutions, or single polymers in simulation, the relaxation of the end-to-end vector provides an appropriate relaxation time scale with which to study the polymer dynamics in flow[24]. This analysis has also been successfully applied to branched and star polymers [9], [25]. Time autocorrelations for the micelle polymer end-to-end vectors, calculated according to Equation 4-8, are shown in Figure 4-2. There appear to be at least two relaxation modes contributing to the overall decay captured by the end-to-end fluctuations; one is fast, appearing as a steep slope in Figure 4-2 at short times, and the other is slow, emerging as the long-time linear portion of the curves. At very long times, yet another regime emerges, but this is likely due to the poor statistics available in the correlation analysis at long times.

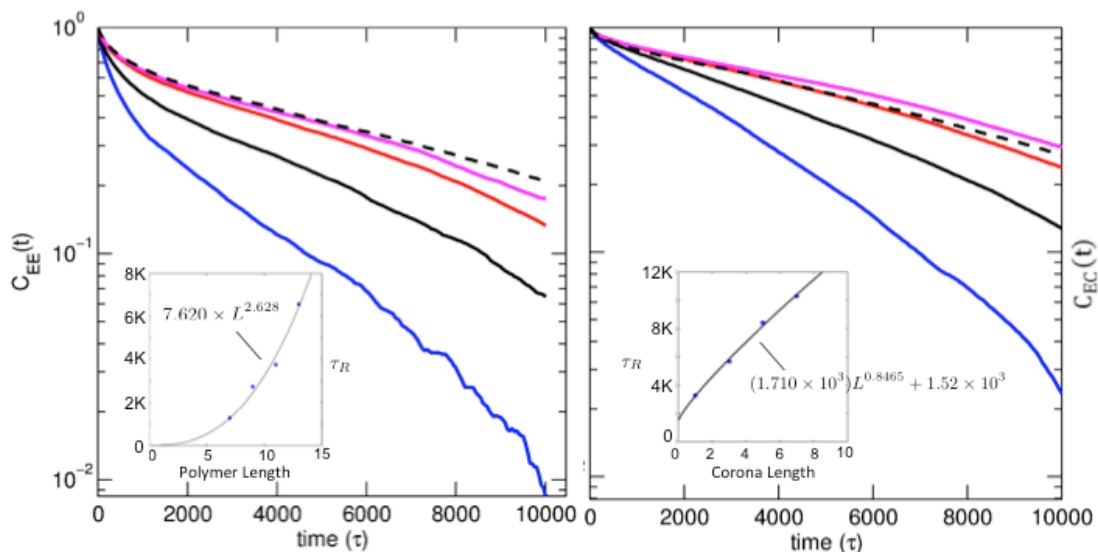


Figure 4-2 – Time autocorrelation functions for the end-to-end (left) and end-to-center (right) vectors of the constituent polymers in the micelles. Shown are A6B1 (blue), A6B3 (black), A6B5 (red), A6B7 (magenta), and A6B9 (black, dashed). All results are taken from the zero-shear state. Inset shows the relaxation times extracted from the correlation functions with a power law fit as a function of total polymer length.

The convolution of decays observed in Figure 4-2 are likely the result of a slow rotational component, and a faster stretching and compressing component of the individual corona arms. In star polymer simulations, end-to-center fluctuations are used to measure rotational relaxations [24], [25]. Micelles, unlike star polymers, are not a single bonded entity, and therefore end-to-end vectors are affected by an added component of translational freedom within the core of the micelles. All things being equal, we would therefore expect a somewhat faster relaxation in the micelle end-to-end vectors. Slower decay of the end-to-center autocorrelations for micelles, where

center refers to the center of mass, shown in Figure 4-2, support this conclusion. Nonetheless, power law fits to the relaxation data are presently phenomenological, as the complexities of the relaxation processes require further investigation.

A similar autocorrelation analysis (not shown) on the end-to-center vectors of the PGNs reveals even stronger bimodal behavior with one very fast, distinct decay mode, and one very slow, long decay mode. Unlike the micelles, PGNs can be easily manipulated in such a way to isolate different relaxation phenomena. First, to determine the contribution from the corona relaxing, we simulated polymer brushes on flat surfaces and closely matched the grafting density to that of the PGNs. Polymer lengths were varied from $N_B = 4$ to $N_B = 18$ and autocorrelation analyses were completed on the end-to-end vectors to obtain the data in Figure 4-3. In addition, we simulated PGNs in which the rigid core was frozen in space by zeroing out the forces each time step. The relaxation results for the end-to-end (end-to-surface) vectors of the polymers for the fixed colloid are also shown in Figure 4-3. These data suggest that the contribution to the overall PGN relaxation from the individual polymers is relatively small. Indeed, when the grafted polymers are very short (< 3 beads), relaxation times are on the same order of magnitude as our sampling rate. Interestingly, the spherical geometry results in a faster relaxation process as compared to the flat surface.

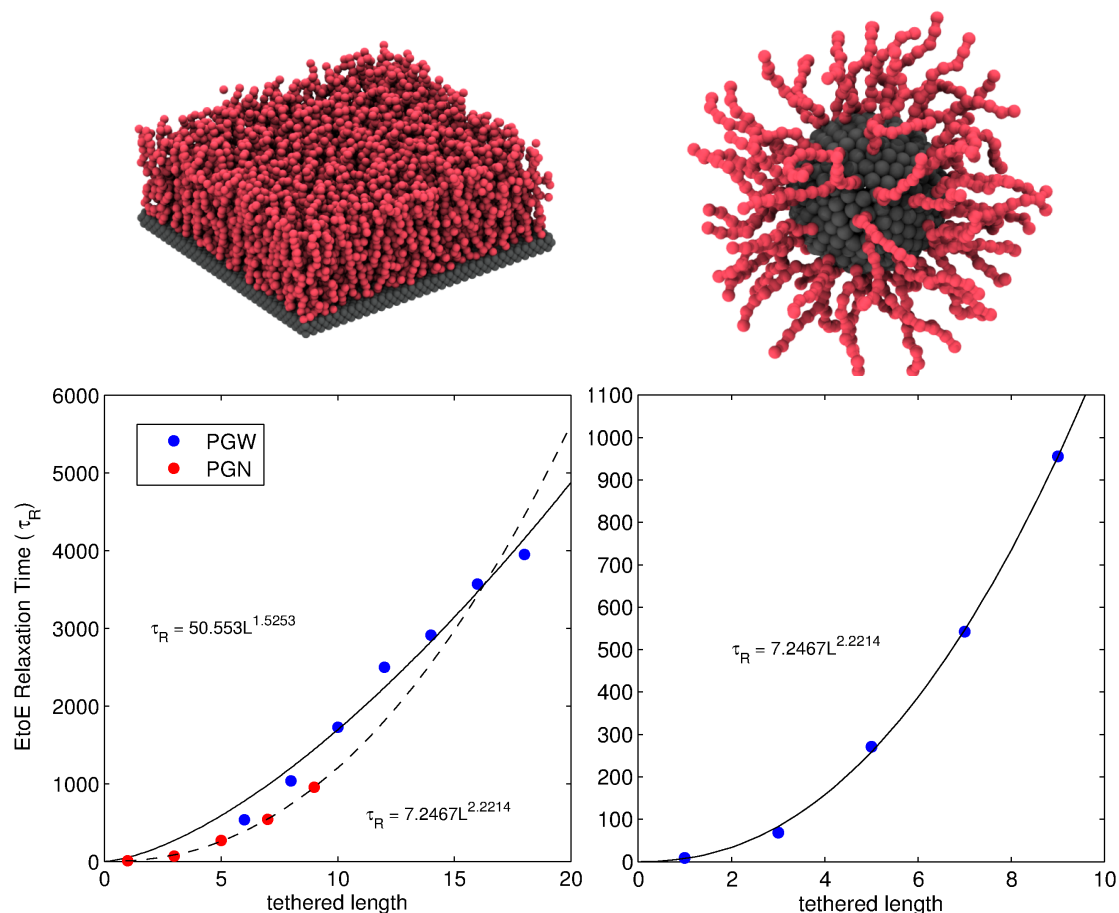


Figure 4-3 – (Top) Snapshots for the two model systems, isolating grafted polymer relaxation behavior. (Bottom) Relaxation times τ_R for polymer grafted walls (PGWs) (left) at matched grafting density to polymer grafted nanoparticles (right) plotted against grafted polymer length. The relaxations for the PGNs are for the case in which translation and rotational motions on the rigid core are removed from the simulations.

Isolating and accurately measuring rotational component of the relaxation is more difficult due to the very large time scale of this relaxation process. Exponential fits to the end-to-center autocorrelations yield results prone to statistical errors. The

Stoke-Einstein computed rotational diffusivity of the untethered nanoparticle is $D_{R,ideal} = 2.65 \times 10^{-5} \tau^{-1}$. In other words, the time scale of rotation in the quiescent state is $10^5 \tau$ —several orders of magnitude larger than the relaxation of the grafted polymer chains. Furthermore, the rotational diffusivity is strongly affected by the presence of even short grafted polymer chains. Figure 4-4 shows how the addition of 1 polymer bead, at a grafting density of 22%, reduces the rotational diffusivity by ~20%. The addition of 3-bead polymers reduces the rotational diffusivity by ~65%. Some insight can be gleaned by fitting the data based on the simplified assumption that the tethered polymers only increase the effective radius of the particle

$$D_R(L) = \frac{k_B T}{8\pi\eta(R + \alpha L)^3} \quad \text{Equation 4-11}$$

where $\alpha \approx 0.52$ based on a least-squares fit. A physical interpretation of this parameter would likely be related to the radius of gyration of a polymer with contour length L , however, our assumptions in this fit are rather naive, and instead we use it as a guide. It is noteworthy that for the longest tethered lengths, the rotational relaxation time scales are of the order $\sim 10^6 \tau$, three orders of magnitude larger than the tethered polymer relaxations, and ten times longer than our simulation runs.

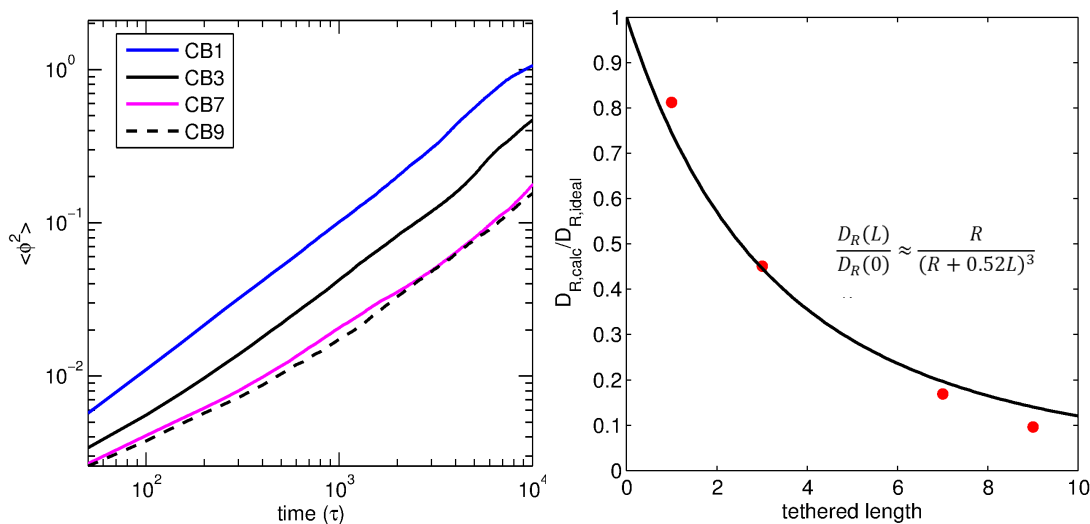


Figure 4-4 – (Left) Mean-squared angular displacement for different tethered polymer lengths. (Right) Dimensionless rotational diffusion coefficients plotted against tethered polymer length, $D_{R,ideal} = 2.65 \times 10^{-5} \tau^{-1}$.

4.3.2 Shape Deformations

Given that relaxation timescales are on the order of the applied shear, it is not surprising that the simulated micelles and PGNs deform in the sheared steady-state. It is worth clarifying the meaning of steady-state here. In most cases, the particles are within a rotational or tank-treading regime, and acquire a single, stable inclination angle. At the high end of the spectrum of shear we begin to see oscillatory stretching/contracting (trembling) behavior in the micelles. The most dynamic behavior is illustrated in the snapshots in Figure 4-5. However, these oscillations are stable, and are therefore considered steady-state behavior. Figure 4-6 shows the normalized diagonal components of the gyration tensor computed using Equation 4-5 for the extremes of each type of particle. When the corona length is short, and trivially short for the PGN, we only see small deformations in the moderate shear-regime. For

the PGN, there is no deviation in shape as the core is rigid, and the single bonded particle does not contribute any significant perturbations. The equivalent micelle exhibits diverging behavior of its flow and gradient axes, whereas the vorticity axes contracts only modestly. When the corona lengths are on the same order as the core radii, the effects of deformation are greatly enhanced. For the PGN, distortions similar to the micelle emerge, with stretched flow, and contracted gradient axes. The micelle deformations have become exaggerated, with stretching in the flow direction more than double that of the quiescent state and correspondingly greater contraction in the gradient direction.

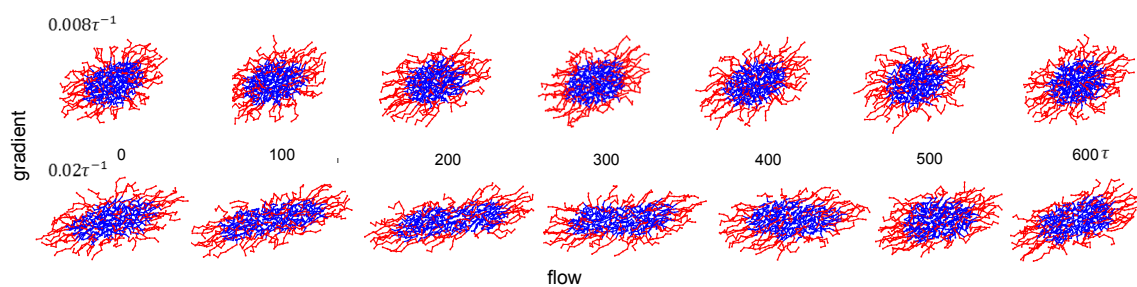


Figure 4-5 – Snapshots of A6B7 micelles demonstrating different dynamic regimes occurring at low and high shear rates. In both cases, the micelles are tank-treading.

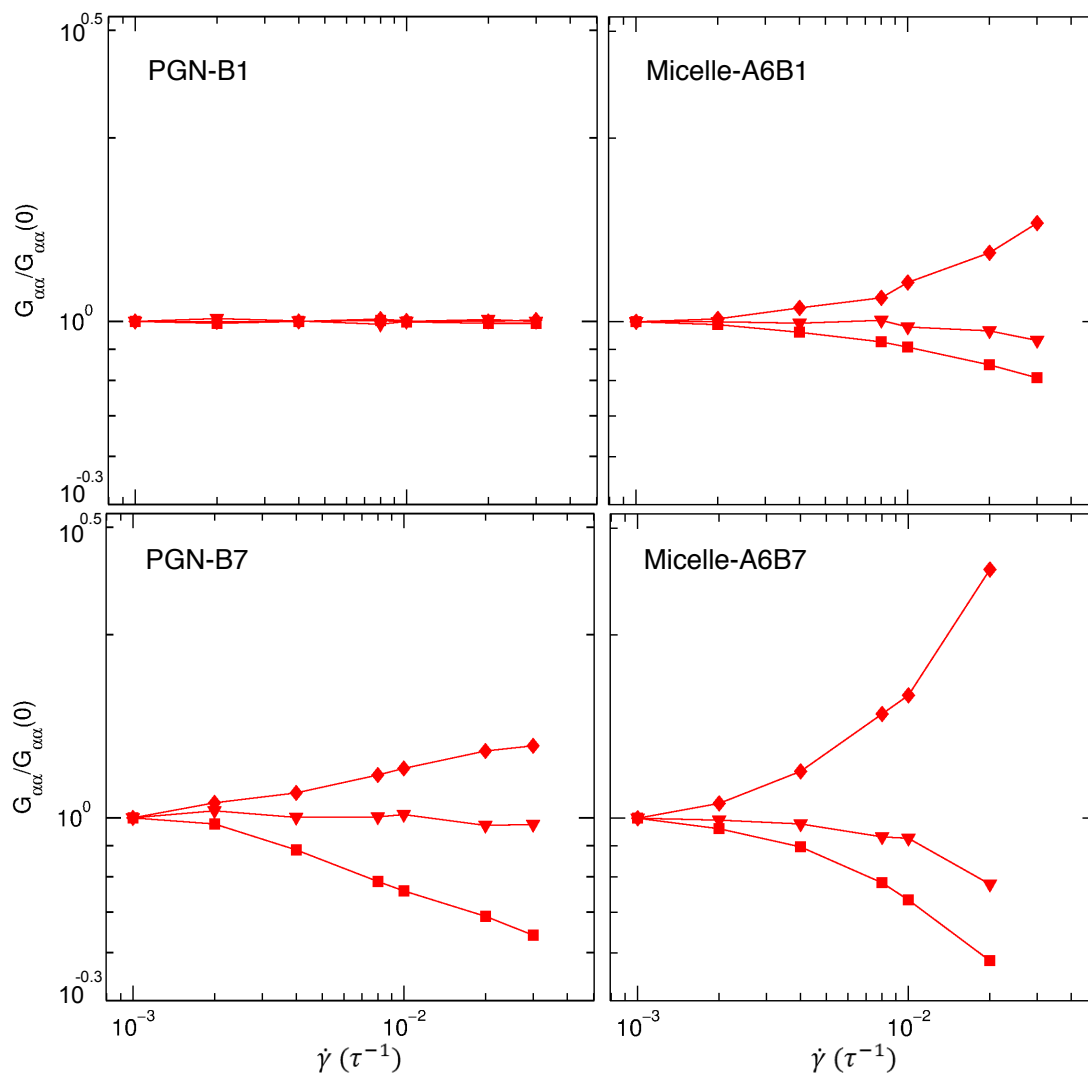


Figure 4-6 – Normalized diagonal components of the gyration tensor for the shortest and longest tethered length for PGNs (left) and micelles (right) plotted against applied shear. All quantities are time-averaged and measured in the steady-state.

The deformations as a function of shear are notably different between the two particle types. Where the micelle stretching/contracting diverges, the corresponding PGN behavior follows a power law at low shear, and then appears to approach limits. These limits are a product of the rigid surface, and correspond to the maximum stretched length of an individual polymer chain. The PGNs also differ in that the

greatest distortion is a contraction in the gradient axis, instead of a stretch along the flow axis, as with the micelles. This result is simply due to the fact that the tethered polymers entering the gradient re-orient into the flow, producing a much smaller gyration component in the gradient direction as compared to their well-solvated, extended state in equilibrium. The mechanisms in the micelle are similar, except that the core is also free to deform in response to the shear forces. As a result, stretching is dramatic, and actually grows exponentially with applied shear. In fact, data points in Figure 4-6 for the A6B7 micelle are missing at the highest shear rate, due to repeated breakage and recombination of the micelles (the latter being a result of the periodic boundaries).

Simulations of star polymers reveal trends in the deformation process similar to a combination of the PGN and micelle behavior. Star polymers deform exponentially at low shear, transition to a power law at moderate shear, and finally approach a limit at high shear. Additionally, they show the greatest deformations as a stretch in the flow direction [9]. Star polymers, being single bonded entities, are expected to reach limits in deformation – not unlike the PGN. However, star polymers are not rigid bodies, and at low shears, where elastic bond forces are still small, one would expect the deformations to be minimally affected by the common attachment point. In this regime, and at high functionalities, they behave in much the same way as micelle would.

The overall shape of the deformed particles can be further characterized by the asphericity parameter defined in Equation 4-6. Asphericity values for both particles are shown in Figure 4-7. We found that the data collapse onto a master curve, with

appropriate choice of the previously discussed relaxation timescales, when plotted against Wi . For the micelles, data collapsed reasonably using the relaxation of the end-to-end vectors of the micelles, which includes rotational aspects. For the PGNs, data collapsed very well using the isolated relaxation of the grafted polymer chains discussed earlier. These master curves highlight some of the features discussed in regard to Figure 4-6. In particular, when Wi values are very small, the particles show no deformation in the flow. This is especially true for the shortest grafted nanoparticle (CB1), where Wi values remain small regardless of the shear rate, owing to the very fast relaxation of the single bonded polymer bead. At intermediate Wi , asphericity increases with a power law dependence for both particles. At high Wi , asphericity can be seen to turn exponential for the micelles, whereas the PGN asphericity begins to flatten out. These results are consistent with the observations made in Figure 4-6, but more importantly demonstrate the importance of relaxation phenomena in governing the dynamics of micelles and PGNs.

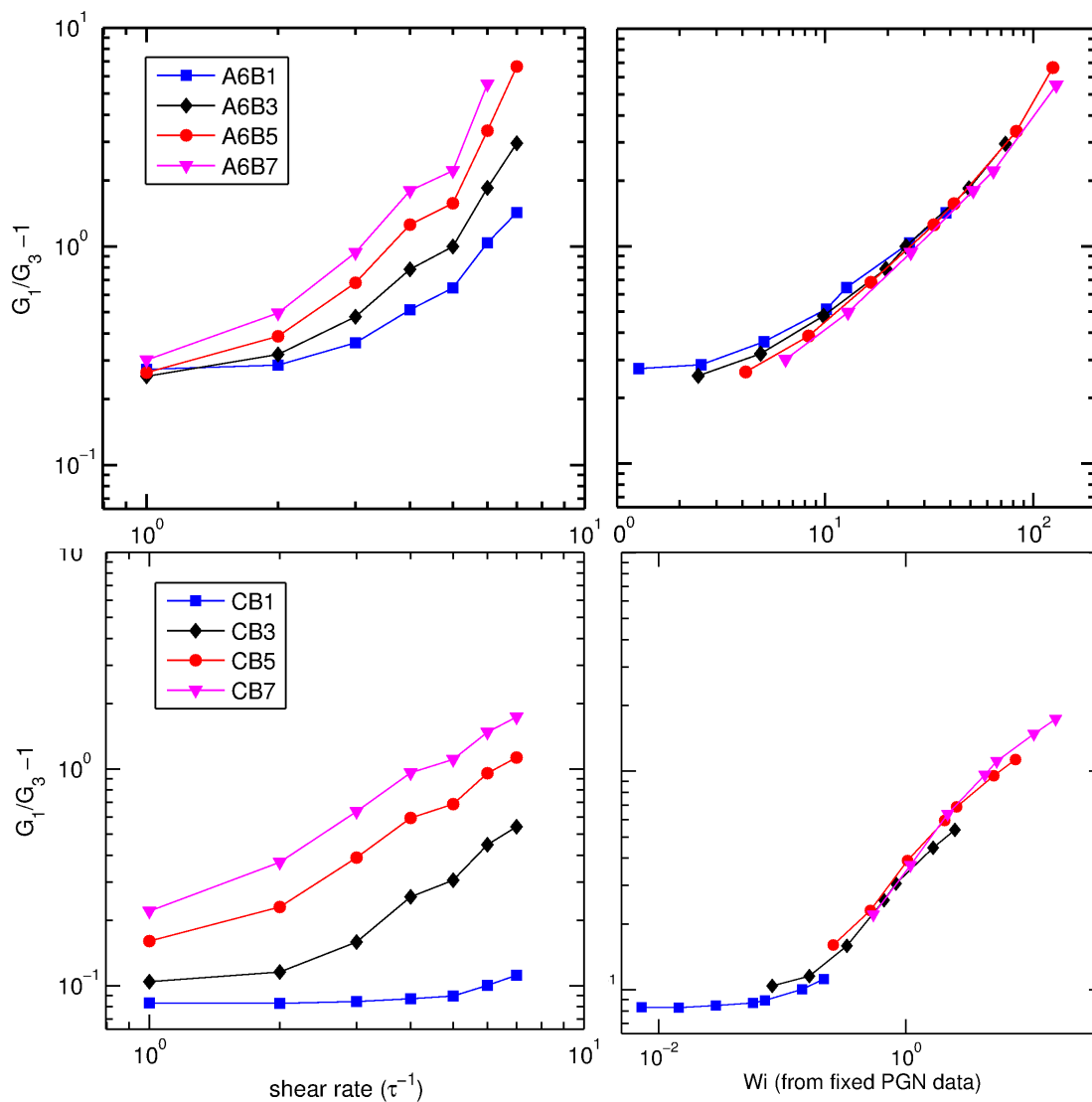


Figure 4-7 – Asphericity parameters for micelles (top) and PGNs (bottom) plotted against shear rate (left) and Wi (right). Wi values are computed by relaxation times characteristic to each particle: a relaxation of the polymer end-to-end vector for the micelles, and the isolated relaxation of the grafted polymers for the nanoparticles.

These same relaxation time scales can also be used to collapse data for the measured flow-alignment, calculated according to Equation 4-7. These results are shown in Figure 4-8 for both particles. Some data are not shown, and in particular, no

data are shown for CB1, the shortest grafted polymer. This is because Equation 4-7 diverges when the particles are nearly spherical, and the time-averaged results are no longer statistically meaningful. Generally, the inclination angle decreases with increased shear rate and this is known behavior in polymers, star polymers, and vesicles [26]–[30]. For fluid vesicles, the decrease in inclination angle can be modeled as a function of the vesicles excess area, which increases with deformation, and therefore shear rate [31].

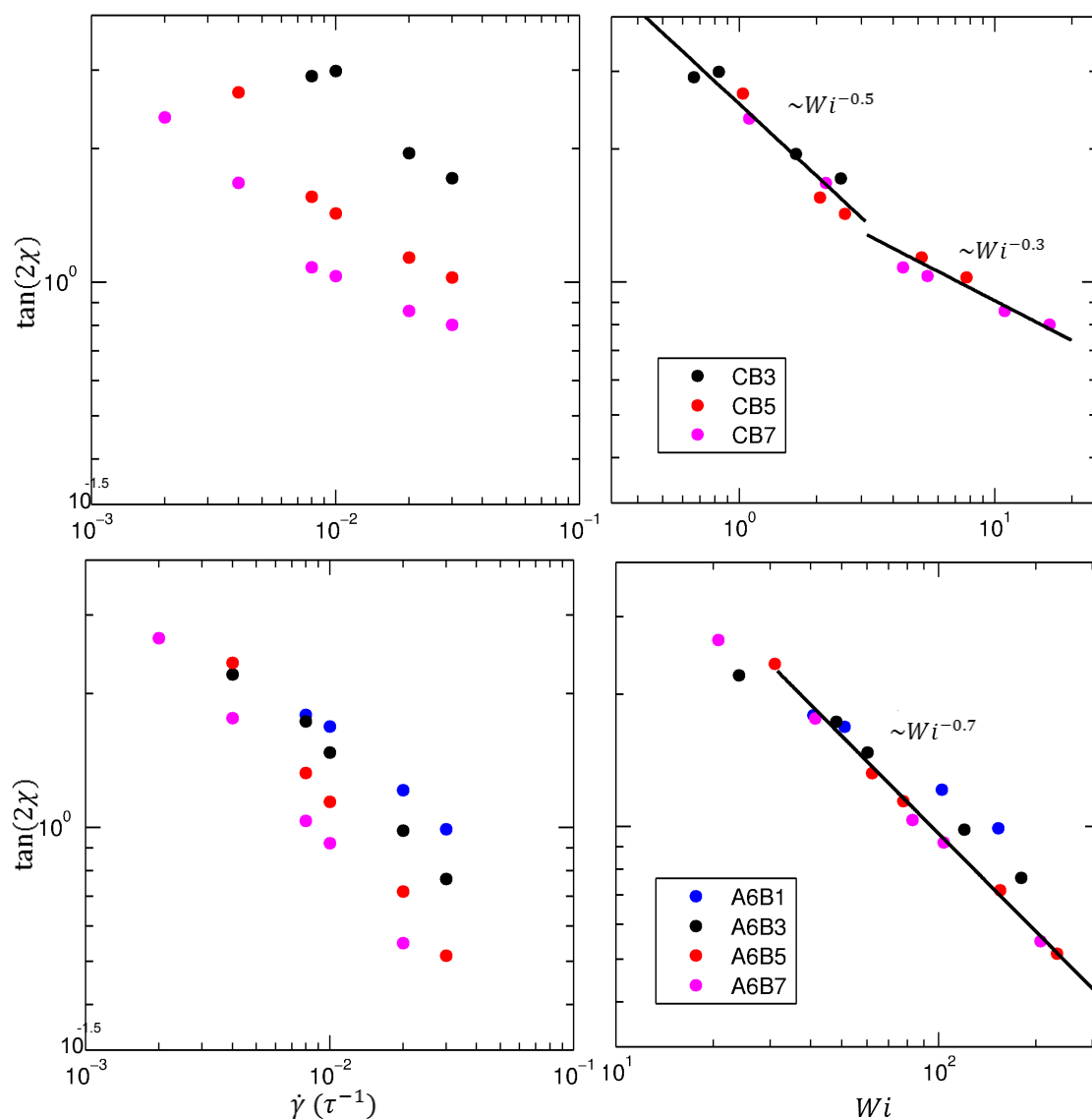


Figure 4-8 – Flow alignment, or orientational resistance, for PGNs (top) and micelles (bottom). Note that the nature of this calculation is not well-suited for nearly-spherical particles, and statistically noisy data have been excluded.

With this insight, it is interesting to note that the PGNs exhibit two distinct phases of inclination – one decaying with $Wi^{-0.5}$ and the other decaying with $Wi^{-0.3}$. The transition occurs at approximately the same location where the asphericity transitions from a growth $\sim Wi^{0.7}$ to a slower growth of $\sim Wi^{0.5}$, which supports inclination angle and excess area, or deformation, being highly correlated. Meanwhile, the micelles exhibit only a single mode dependence following $\sim Wi^{-0.7}$. It is important to point out that the Wi definitions for micelles and PGNs are not equivalent, and therefore only qualitative observations on their dependence on Wi can be made. The decrease in inclination angle fitting a single power law follows from the previous discussion for PGNs. Unlike the PGNs, however, the micelle asphericity increases exponentially as a function of Wi throughout. Correspondingly, we only observe a single slope in the inclination angle dependence on Wi . It is clear in Figure 4-8 that the micelle data do not collapse as well as the PGN data, and that in fact, the micelle inclination angles may not follow a power law dependence on Wi . Resolving this shortcoming requires a more rigorous analysis of the micelle relaxation phenomena.

4.3.3 Rotational Motion

The final, and perhaps most important behavior to the fluid dynamics, is the rotation of the particles. Figure 4-9 shows the normalized rotational frequencies for both particles as a function of shear rate and Wi . Note that both data sets collapse onto

master curves against Wi , but that again, the micelle data do not collapse as well as the PGN data. Here we have used the “rotational” relaxation time of the micelles measured using autocorrelations of the end-to-center vectors and previously discussed, whereas previously we had used end-to-end relaxations to collapse the data. Clearly, this result strongly suggests the existence of a yet unidentified relaxation time that would collapse both deformation and rotational data.

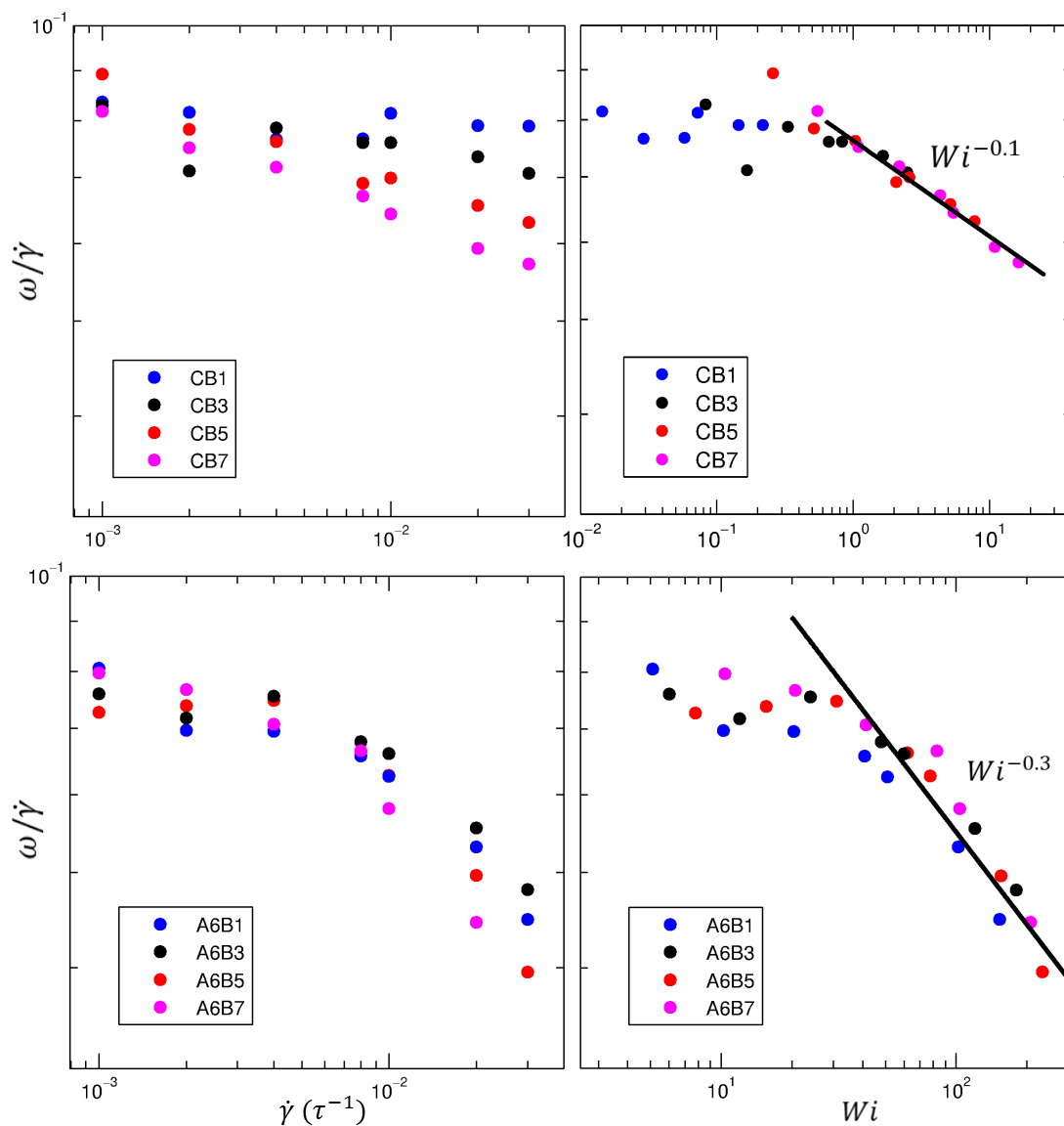


Figure 4-9 – Normalized rotational frequencies for PGNs (top) and micelles (bottom) plotted against shear rate (left) and collapsed into master curves against Wi (right).

From Figure 4-9, we see that for both PGNs and micelles the rotation rates decrease away from their low-shear constant value. In other words, at low shear, the particles rotate at a rate proportional to the applied shear, consistent with rods, linear polymers, star polymers, droplets, vesicles, and capsules [9], [19], [32]. At higher shear rates, this dependence becomes sub-linear, consistent with work seen on star polymers [9]. It is also apparent that the micelles rotate at a slower rate than their PGN counterparts, even at low shear rates. There are likely several reasons for this difference. For one, the grafted particles rotate as a single body, despite their flexible coronas, whereas the micelles tank-tread. This is an important distinction, particularly at high shear rates. As the micelles become deformed into ellipsoids, rotation would imply the ellipsoid flipping about the vorticity axis. Though we see some oscillation at very high shear rates, we generally only observe time-independent, constant inclination angle, behavior from the micelles. Thus, the micelle surface area increases with shear rate, resulting in a larger contour length for the polymers to traverse, and therefore slow “rotation” rates.

The PGNs rotate proportionally to applied shear at low Wi , and follow a power law decay away of $\sim Wi^{-0.1}$ beginning at about $Wi = 1.0$, when relaxation timescales become longer than the time scale of the applied shear. The shortest tethered polymer particle does not deviate from its linear dependence on shear rate, again owing to the fast relaxation time scales of the single bonded particle. This result also suggests that

an untethered nanoparticle would exhibit only a linear dependence on shear rate in the studied regime, which is consistent with the Stokes solutions. At higher Wi , though the relationship becomes sub-linear, it does not deviate as quickly compared to the micelles. Following that discussion, PGNs rotate and do not tank-tread. Thus the sub-linear behavior would be a result of screening of the flow by the presence of the polymers, an increased effective drag, and dissipation through individual polymer fluctuations.

4.4 Conclusions

For the first time, PGN and micelle steady-state dynamics have been analyzed in detail using coarse-grained molecular dynamics. We have shown that PGNs and micelles, though similar in overall shape and size, exhibit different steady-state dynamics owing to the differences in core construction. Compared to star polymers and vesicles, micelles occupy a middle ground. The lack of strong bonds to maintain micelle integrity means that shear forces tend to deform the micelles exponentially, which also results in a steep decline in the inclination angle as a function of Wi . Qualitatively, these results match the behavior seen for vesicles and diverge from star and homopolymer results at high Wi . PGNs, on the other hand, were found to exhibit dynamics similar to the micelles in the low Wi regime, but quickly became more star polymer in nature as Wi increases. When Wi is small, the PGN deforms with $\sim Wi^{0.7}$ and aligns with $\sim Wi^{-0.5}$; when Wi is large, the exponents become smaller in magnitude, 0.5 and -0.3 , respectively. We attributed these regimes to the rearrangement of polymer beads at low Wi , and to the finitely extensible nature of the bonds at high Wi .

Rotational dynamics were shown to be fundamentally different between the two particles. PGNs rotate while micelles tank-tread. Thus, micelles deviate from the linear dependence on shear rate more quickly than their PGN equivalents. In both cases though, we found a sub-linear deviation occurring at high Wi . This result is consistent with the available literature on similar soft particles. Ultimately, the differences between rotational dynamics at high Wi were attributed to the deformation of the micelles, increasing the contour length for tank-treading, as compared to unmodified rigid body rotation for the PGNs.

Though a thorough investigation into relaxation time scales was carried out, we were unable to adequately capture the relaxation timescale important to the *micelle* dynamics. More recent, unpublished work, strongly supports a multi-mode decay in many of the measured relaxation processes. We expect further analysis to reveal both the correct timescale, and its mechanism, such that the dynamics collapse onto single master curves that are comparable, quantitatively, to the PGN results.

Acknowledgements

We would like to thank the National Science Foundation for funding through the National Science Foundation Graduate Research Fellowship Program (NSFGRFP) under Grant No. DGE-1144153. This work was also supported by the computational facilities (Darter and Kraken) provided by the National Institute of Computational Sciences (NICS) and made available through the NSFGRFP.

REFERENCES

- [1] J. Deschamps, V. Kantsler, E. Segre, and V. Steinberg, “Dynamics of a vesicle in general flow.,” *Proc. Natl. Acad. Sci. U. S. A.*, vol. 106, no. 28, pp. 11444–7, Jul. 2009.
- [2] T. Fischer, M. Stohr-Lissen, and H. Schmid-Schonbein, “The red cell as a fluid droplet: tank tread-like motion of the human erythrocyte membrane in shear flow,” *Science (80-.)*, vol. 202, no. 4370, pp. 894–896, Nov. 1978.
- [3] M. Kraus, W. Wintz, U. Seifert, and R. Lipowsky, “Fluid Vesicles in Shear Flow.,” *Phys. Rev. Lett.*, vol. 77, no. 17, pp. 3685–3688, Oct. 1996.
- [4] F. Rioual, T. Biben, and C. Misbah, “Analytical analysis of a vesicle tumbling under a shear flow,” *Phys. Rev. E*, vol. 69, no. 6, p. 061914, Jun. 2004.
- [5] S. Keller and R. Skalak, “Motion of a tank-treading ellipsoidal particle in a shear flow,” *J. Fluid Mech.*, vol. 120, no. -1, p. 27, Apr. 1982.
- [6] H. Zhao and E. S. G. Shaqfeh, “The dynamics of a vesicle in simple shear flow,” *J. Fluid Mech.*, vol. 674, pp. 578–604, Mar. 2011.
- [7] H. Noguchi and G. Gompper, “Fluid vesicles with viscous membranes in shear flow,” *Phys. Rev. Lett.*, pp. 0–3, 2004.
- [8] S. Goyal and F. a Escobedo, “Structure and transport properties of polymer grafted nanoparticles.,” *J. Chem. Phys.*, vol. 135, no. 18, p. 184902, Nov. 2011.
- [9] M. Ripoll, R. Winkler, and G. Gompper, “Star Polymers in Shear Flow,” *Phys. Rev. Lett.*, vol. 96, no. 18, p. 188302, May 2006.
- [10] A. Nikoubashman, G. Kahl, and C. N. Likos, “Flow quantization and nonequilibrium nucleation of soft crystals,” *Soft Matter*, vol. 8, no. 15, p. 4121, 2012.
- [11] S. P. Singh, A. Chatterji, G. Gompper, and R. G. Winkler, “Dynamical and Rheological Properties of Ultrasoft Colloids under Shear Flow,” *Macromolecules*, vol. 46, no. 19, pp. 8026–8036, Oct. 2013.
- [12] J. Castillo-Tejas, J. F. J. Alvarado, S. Carro, F. Pérez-Villaseñor, F. Bautista, and O. Manero, “Rheology of wormlike micelles from non-equilibrium

- molecular dynamics,” *J. Nonnewton. Fluid Mech.*, vol. 166, no. 3–4, pp. 194–207, Feb. 2011.
- [13] B. a. Rolfe, J. Chun, and Y. L. Joo, “Dynamics of micelle–nanoparticle systems undergoing shear: a coarse-grained molecular dynamics approach,” *Soft Matter*, vol. 9, no. 43, p. 10294, 2013.
- [14] D. C. Pozzo and L. M. Walker, “Shear Orientation of Nanoparticle Arrays Templated in a Thermoreversible Block Copolymer Micellar Crystal,” *Macromolecules*, vol. 40, no. 16, pp. 5801–5811, Aug. 2007.
- [15] B. J. Ackerson, “Shear induced order and shear processing of model hard sphere suspensions,” *J. Rheol. (N. Y. N. Y.)*, vol. 34, no. 4, p. 553, May 1990.
- [16] H. Watanabe, M. Yao, T. Sato, and K. Osaki, “Non-Newtonian Flow Behavior of Diblock Copolymer Micelles : Shear-Thinning in a Nonentangling Matrix,” *Society*, vol. 9297, no. 96, pp. 5905–5912, 1997.
- [17] G. McConnell, M. Lin, and A. Gast, “Long range order in polymeric micelles under steady shear,” *Macromolecules*, pp. 6754–6764, 1995.
- [18] C.-C. Hsieh, A. Balducci, and P. S. Doyle, “An Experimental Study of DNA Rotational Relaxation Time in Nanoslits,” *Macromolecules*, vol. 40, pp. 5196–5205, 2007.
- [19] S. Doi, Masao, Edwards, *The theory of polymer dynamics*. Oxford, 1986, p. 222.
- [20] P. E. Rouse, “A Theory of the Linear Viscoelastic Properties of Dilute Solutions of Coiling Polymers,” *J. Chem. Phys.*, vol. 21, no. 7, p. 1272, 1953.
- [21] S. J. Marrink, H. J. Risselada, S. Yefimov, D. P. Tieleman, and A. H. de Vries, “The MARTINI force field: coarse grained model for biomolecular simulations,” *J. Phys. Chem. B*, vol. 111, no. 27, pp. 7812–24, Jul. 2007.
- [22] P. Español, “Dissipative particle dynamics with energy conservation,” *EPL (Europhysics Letters)*, vol. 40, no. 6. p. 631, 1997.
- [23] S. Plimpton, “Fast Parallel Algorithms for Short – Range Molecular Dynamics,” vol. 117, no. June 1994, pp. 1–42, 1995.
- [24] J. S. Hur, E. S. G. Shaqfeh, and R. G. Larson, “Brownian dynamics simulations of single DNA molecules in shear flow,” *Molecules*, no. August, pp. 713–742, 2000.

- [25] G. S. Grest, K. Kremer, S. T. Milner, and T. A. Wittent, "Self-Entangled Many-Arm Star Polymers," pp. 1904–1910, 1989.
- [26] C. Aust, M. Kro, and S. Hess, "Structure and Dynamics of Dilute Polymer Solutions under Shear Flow via Nonequilibrium Molecular Dynamics," pp. 5660–5672, 1999.
- [27] a Link and J. Springer, "Light-Scattering from Dilute Polymer-Solutions in Shear-Flow," *Macromolecules*, vol. 26, pp. 464–471, 1993.
- [28] R. E. Teixeira, H. P. Babcock, E. S. G. Shaqfeh, and S. Chu, "Shear thinning and tumbling dynamics of single polymers in the flow-gradient plane," *Macromolecules*, vol. 38, pp. 581–592, 2005.
- [29] Y. Navot, "Elastic membranes in viscous shear flow," *Phys. Fluids*, vol. 10, no. 1998, pp. 1819–1833, 1998.
- [30] V. Kantsler and V. Steinberg, "Orientation and Dynamics of a Vesicle in Tank-Treading Motion in Shear Flow," *Phys. Rev. Lett.*, vol. 95, no. 25, p. 258101, Dec. 2005.
- [31] C. Misbah, "Vacillating Breathing and Tumbling of Vesicles under Shear Flow," *Phys. Rev. Lett.*, vol. 96, no. 2, p. 028104, Jan. 2006.
- [32] C. Aust, S. Hess, and M. Kröger, "Rotation and deformation of a finitely extendable flexible polymer molecule in a steady shear flow," *Macromolecules*, vol. 35, pp. 8621–8631, 2002.